

© 2013 by Jacob Thomas Stewart. All rights reserved.

HIGH-RESOLUTION INFRARED SPECTROSCOPY OF LARGE MOLECULES AND  
WATER CLUSTERS USING QUANTUM CASCADE LASERS

BY

JACOB THOMAS STEWART

DISSERTATION

Submitted in partial fulfillment of the requirements  
for the degree of Doctor of Philosophy in Chemistry  
in the Graduate College of the  
University of Illinois at Urbana-Champaign, 2013

Urbana, Illinois

Doctoral Committee:

Professor Benjamin McCall, Chair  
Professor Martin Gruebele  
Professor Alexander Scheeline  
Professor So Hirata

# Abstract

High-resolution infrared spectroscopy is a powerful tool for obtaining detailed information about molecules and molecular clusters. This dissertation presents several high-resolution spectroscopic studies of large molecules and water clusters which have been obtained using a quantum cascade laser (QCL) based infrared spectrometer coupled to a supersonic expansion source. The spectrometer operates near  $8.5 \mu\text{m}$  and has been developed for the purpose of obtaining a high-resolution gas phase spectrum of  $\text{C}_{60}$  for use in astronomical observations of this molecule. Details of the development of the spectrometer and initial results measuring methylene bromide are included as appendices in the dissertation. The spectrometer was used to attempt to observe the high-resolution spectrum of  $\text{C}_{60}$ , but the spectrum has not yet been observed. Calculations of the expected signal-to-noise ratio reveal that the spectrum should have been observable, and the lack of an observed spectrum is attributed to inefficient vibrational cooling of  $\text{C}_{60}$  in the supersonic expansion. This finding is in contrast to previous studies which showed good cooling of polycyclic aromatic hydrocarbons (PAHs), including high-resolution spectroscopy of pyrene ( $\text{C}_{16}\text{H}_{10}$ ) near  $1184 \text{ cm}^{-1}$  using the QCL spectrometer. Details of the high-resolution infrared spectrum of pyrene and the good cooling which was observed are included as an appendix in the dissertation.

The QCL spectrometer has also been utilized to study two small deuterated water clusters:  $\text{Ar-D}_2\text{O}$  and  $(\text{D}_2\text{O})_2$ . Several bands of the bending mode of  $\text{Ar-D}_2\text{O}$  were observed in  $\text{Ar/D}_2\text{O}$  supersonic expansions. The observed bands were fit to a pseudo-diatomic model which treats  $\text{D}_2\text{O}$  as a nearly free rotor within the complex, and accurate molecular constants were obtained. The deviations in the fits to this model ranged from  $0.0002$  to  $0.0005 \text{ cm}^{-1}$ , and two previously unobserved bands of the complex were identified. The bending mode of the hydrogen bond donor of deuterated water dimer ( $(\text{D}_2\text{O})_2$ ) has also been observed with rotational resolution, which represents the first high-resolution study of the bending modes of water dimer. Two perpendicular sub-bands were observed and interpreted in the context of the tunneling motions which occur in the water dimer complex. Excitation of the donor bending mode was found to have little effect on the tunneling motion of the acceptor molecule, but caused significant perturbations on the tunneling motion which exchanges the roles of the hydrogen bond donor and acceptor. An accurate value for the gas phase

vibrational frequency of the donor bend was also obtained, which was found to be quite similar to previous theoretical predictions obtained from an *ab initio* potential energy surface.

Details of the construction of an external cavity QCL (EC-QCL) system are also presented. The EC-QCL provides a significant improvement in the frequency tunability of the spectrometer, increasing the tuning range from 1180–1200  $\text{cm}^{-1}$  to 1135–1220  $\text{cm}^{-1}$ . The procedures for putting the system together and aligning it are outlined, and the details of implementing mode-hop free tuning of the laser are also presented. Mode-hop free tuning of the EC-QCL has been achieved over  $\sim 0.6 \text{ cm}^{-1}$ , which is sufficient to allow the EC-QCL to be used for high-resolution spectroscopy once the frequency stability of the laser can be improved.

*For Alysa, who has been so supportive throughout this journey*

# Acknowledgments

I would first like to thank my advisor, Ben McCall, for being a mentor throughout my work on the projects presented in this dissertation. He has allowed me to follow my interests, especially in working on the water cluster work presented here, which turned out to be far more “interesting” than I first anticipated. His guidance throughout my time in Illinois has been extremely helpful. I also appreciate his trust in allowing me to set my own schedule, which has been invaluable as two children have joined the Stewart family during our stay in Illinois.

I am also especially grateful to Brian Brumfield, who I worked with closely during my first three years in the McCall group. His training and help during my first few years of grad school made a big impact on my time here. He provided a great example to me of what it means to be a scientist and is also a great friend. His work on constructing the QCL spectrometer made the work presented in this dissertation possible. Thanks for everything, Brummy.

I also wish to thank the rest of the McCall group I have had the pleasure of working with, especially Brad Gibson, who is now the heir of the QCL system. It has been a pleasure to work with the group as it has evolved throughout the years. I am especially grateful to Brian Siller and Kyle Crabtree for their help in getting me started with computer programming and helping to write the code that has kept our instruments running. They have also been the source of many great conversations around the lunch table, both about science and not. I also wish to especially thank Mike Porambo and Jamie Hodges, my fellow Springborn Fellows, for their help throughout the years.

I have been blessed to be a part of the Springborn Fellowship program, and I am extremely grateful to Dr. Bob Springborn and his wife, Carolyn, for providing the funds for this program. I feel that the Fellowship really allowed me to pursue the research that interested me, and also was a great help to my family financially. I am also grateful for the R. C. Fuson Fellowship I received from the Department of Chemistry, which was a boon to our family finances.

Last, but certainly not least, I am grateful for my wife, Alysa, and my three children: Benjamin, Levi, and Jubilee. Alysa has been wonderful and so supportive of me while I have been pursuing my goal of

earning a PhD. I am especially grateful for her patience on those days and nights where I had to stay late or come back to the lab when the spectrometer was actually working. It's also great to come home to two little boys running down the sidewalk to give you a hug, and I thank Benjamin and Levi for all of the hugs and kisses and wrestling. And Jubilee, thanks for being a wonderful baby while I have been finishing my work on this dissertation. I love all four of you so much.

# Table of Contents

<b>List of Tables</b> . . . . .	<b>ix</b>
<b>List of Figures</b> . . . . .	<b>x</b>
<b>Chapter 1 Introduction</b> . . . . .	<b>1</b>
1.1 Rotationally-resolved Spectroscopy of Large Molecules . . . . .	2
1.2 Spectroscopy of Deuterated Water Clusters . . . . .	4
1.3 External Cavity QCLs . . . . .	5
<b>Chapter 2 Inefficient Vibrational Cooling of C<sub>60</sub> in a Supersonic Expansion</b> . . . . .	<b>6</b>
2.1 Introduction . . . . .	6
2.2 Experimental . . . . .	7
2.3 Estimating Signal-to-Noise . . . . .	8
2.4 Results . . . . .	10
2.4.1 Search for C <sub>60</sub> Spectrum . . . . .	10
2.4.2 High Temperature Measurements of D <sub>2</sub> O . . . . .	13
2.5 Discussion . . . . .	13
2.6 Alternative Experiments . . . . .	20
2.7 Conclusions . . . . .	21
<b>Chapter 3 High-resolution Infrared Spectroscopy of the Bending Mode of Ar-D<sub>2</sub>O</b> . . . . .	<b>22</b>
3.1 Introduction . . . . .	22
3.2 Experimental . . . . .	22
3.3 Results and Discussion . . . . .	23
3.3.1 $\Pi(1_{10}, \nu_2 = 1) \leftarrow \Sigma(1_{01})$ band . . . . .	24
3.3.2 $\Pi(1_{01}, \nu_2 = 1) \leftarrow \Sigma(1_{01})$ band . . . . .	26
3.3.3 Additional $\Pi \leftarrow \Sigma$ bands . . . . .	27
3.4 Conclusion . . . . .	31
<b>Chapter 4 Rotationally-resolved Infrared Spectroscopy of the Donor Bending Mode of Deuterated Water Dimer</b> . . . . .	<b>33</b>
4.1 Introduction . . . . .	33
4.2 Experimental . . . . .	34
4.3 Energy level structure of water dimer . . . . .	35
4.4 Results . . . . .	36
4.5 Discussion . . . . .	46
4.6 Conclusions . . . . .	49

<b>Chapter 5</b>	<b>Development of an External Cavity Quantum Cascade Laser Spectrometer</b>	<b>50</b>
5.1	Introduction	50
5.2	Basic Design of the Laser	51
5.3	Aligning the System	56
5.4	Laser Performance	60
5.5	Mode-hop Free Tuning	61
5.6	Future Work	63
<b>Appendix A</b>	<b>Data sheets for the QCL chip used in the external cavity QCL system</b>	<b>66</b>
<b>Appendix B</b>	<b>A quantum cascade laser cw cavity ringdown spectrometer coupled to a supersonic expansion source</b>	<b>71</b>
<b>Appendix C</b>	<b>High-resolution spectroscopy of the <math>\nu_8</math> band of methylene bromide using a quantum cascade laser</b>	<b>81</b>
<b>Appendix D</b>	<b>Extending the limits of rotationally resolved absorption spectroscopy: Pyrene</b>	<b>88</b>
<b>References</b>		<b>113</b>

# List of Tables

2.1	Summary of attempted absorption spectroscopy of C <sub>60</sub> . . . . .	12
2.2	List of observed D <sub>2</sub> O transitions . . . . .	14
2.3	Estimated number of two body hard sphere collisions experienced by large molecules seeded in an argon supersonic expansion . . . . .	16
2.4	Hard sphere radii used to compute the mean free path of molecules in the supersonic expansion	17
2.5	Vibrational partition function, average vibrational energy (above zero-point energy) in cm <sup>-1</sup> , frequency of the lowest energy vibrational mode, and energy to collision ratio for the molecules listed in Table 2.3 . . . . .	19
3.1	Comparison of molecular constants for the $\Pi(1_{10}, \nu_2 = 1) \leftarrow \Sigma(1_{01})$ band of Ar-D <sub>2</sub> O . . . . .	25
3.2	Observed transitions for the $\Pi(1_{10}, \nu_2 = 1) \leftarrow \Sigma(1_{01})$ band of Ar-D <sub>2</sub> O . . . . .	25
3.3	Molecular constants for the $\Pi(1_{01}, \nu_2 = 1) \leftarrow \Sigma(1_{01})$ band and two newly observed $\Pi \leftarrow \Sigma$ bands of Ar-D <sub>2</sub> O . . . . .	28
3.4	Observed transitions for the $\Pi(1_{01}, \nu_2 = 1) \leftarrow \Sigma(1_{01})$ band of Ar-D <sub>2</sub> O . . . . .	28
3.5	Observed transitions for the two newly observed $\Pi \leftarrow \Sigma$ bands of Ar-D <sub>2</sub> O . . . . .	31
4.1	Approximate center frequency positions of the $K_a = 1 \leftarrow 0$ and $K_a = 2 \leftarrow 1$ sub-bands of the donor bend of (D <sub>2</sub> O) <sub>2</sub> . . . . .	44
4.2	Comparison of the frequency of the donor bending mode of (D <sub>2</sub> O) <sub>2</sub> calculated in the present study to previous experimental and theoretical work . . . . .	48

# List of Figures

2.1	$C_{60}$ vibrational partition function as a function of temperature . . . . .	8
2.2	Plot of calculated signal-to-noise ratio for spectroscopy of $C_{60}$ as a function of frequency . . .	11
2.3	Representative absorption spectrum of the Ar/ $C_{60}$ expansion from 1184 – 1186 $\text{cm}^{-1}$ . . . . .	12
2.4	Boltzmann plot of $D_2O$ rotational levels observed in a supersonic jet at 875 K . . . . .	14
3.1	$Q$ -branch region of the $\Pi(1_{10}, \nu_2 = 1) \leftarrow \Sigma(1_{01})$ band of Ar- $D_2O$ . . . . .	24
3.2	$Q$ -branch of the $\Pi(1_{01}, \nu_2 = 1) \leftarrow \Sigma(1_{01})$ band of Ar- $D_2O$ . . . . .	27
3.3	$Q$ -branch region of two previously unobserved $\Pi \leftarrow \Sigma$ transitions of Ar- $D_2O$ . . . . .	29
4.1	Representation of the two intramolecular bending modes of $(D_2O)_2$ , corresponding to bending of the hydrogen bond acceptor and the hydrogen bond donor . . . . .	35
4.2	Energy levels of the tunneling sublevels of the $K_a = 0, J = 0$ rotational level of the ground state of $(D_2O)_2$ . . . . .	37
4.3	Plot of $\ln(\text{relative intensity})$ versus $\ln(\chi_{D_2O})$ for several $D_2O/H_2O$ mixtures to determine the cluster size responsible for absorption features recorded near 1195.55 $\text{cm}^{-1}$ . . . . .	38
4.4	Observed spectrum of the $K_a = 1 \leftarrow 0$ sub-band of the bending mode of hydrogen bond donor measured in an Ar supersonic expansion . . . . .	40
4.5	Observed spectrum of the $K_a = 2 \leftarrow 1$ sub-band of the bending mode of hydrogen bond donor measured in an Ar supersonic expansion . . . . .	41
4.6	Observed spectrum of the $K_a = 2 \leftarrow 1$ sub-band of the bending mode of hydrogen bond donor measured in a He supersonic expansion . . . . .	41
4.7	Zoomed-in views of the groups of R-branch lines of the $K_a = 1 \leftarrow 0$ band measured in an Ar expansion . . . . .	42
4.8	Zoomed-in views of the groups of R-branch lines $K_a = 2 \leftarrow 1$ band measured in an Ar expansion . . . . .	43
4.9	Zoomed-in views of the groups of R-branch lines $K_a = 2 \leftarrow 1$ band measured in a He expansion . . . . .	44
4.10	$Q$ -branches of the $K_a = 1 \leftarrow 0$ band for both the $A_1^+/E_1^+/B_1^+$ tunneling levels and the $A_2^-/E_2^-/B_2^-$ tunneling levels as observed in an Ar expansion . . . . .	45
4.11	$Q$ -branches of the $K_a = 2 \leftarrow 1$ band for both the $A_1^+/E_1^+/B_1^+$ tunneling levels and the $A_2^-/E_2^-/B_2^-$ tunneling levels as observed in an Ar expansion . . . . .	45
4.12	Energy level diagram for the observed $(D_2O)_2$ bands . . . . .	47
5.1	Schematic diagram of the external cavity QCL system . . . . .	52
5.2	Illustration of proper bias voltage for QCL chip used in the EC-QCL . . . . .	53
5.3	Absolute efficiency of the diffraction grating used in the EC-QCL setup versus wavelength . . . . .	54
5.4	Photograph of the stack of stages underneath the diffraction grating and output mirror . . . . .	55
5.5	Photograph of the entire EC-QCL setup . . . . .	56
5.6	Setup for running the EC-QCL in pulsed mode . . . . .	58
5.7	Measured optical power of the EC-QCL plotted as a function of the laser frequency . . . . .	60
5.8	Frequency of the EC-QCL as measured by a wavemeter when only the current applied to the laser is varied . . . . .	62
5.9	Frequency of the EC-QCL as measured by a wavemeter when only the diffraction grating angle is varied . . . . .	63

5.10 Mode-hop free tuning of the EC-QCL over  $>0.6 \text{ cm}^{-1}$  . . . . . 64

# Chapter 1

## Introduction

High-resolution spectroscopy is a powerful technique which is widely used to obtain detailed information about fundamental properties of molecules, such as their structure, bonding, and interactions with other molecules. Infrared spectroscopy, in particular, allows us to measure the vibrational modes of molecules, and with sufficient resolution, the rotational levels of both the ground and vibrationally excited states can also be directly measured. Experimental spectra provide important information to help develop and refine theoretical frameworks which have been created to describe the detailed energy level structures of molecules. Obtaining low resolution spectra of abundant molecules is relatively simple and is easily accomplished with Fourier transform infrared (FTIR) instruments found in chemical laboratories around the globe. Obtaining high-resolution, rotationally-resolved spectra throughout the infrared spectrum is significantly more challenging, though, and generally requires the use of high-intensity light sources, such as lasers or synchrotron radiation sources.

While there are pulsed laser sources that are available throughout the mid-infrared, continuous wave (cw) laser sources are required for performing rotationally-resolved vibrational spectroscopy because they inherently possess a much narrower linewidth than pulsed sources. For infrared spectroscopy down to  $\sim 5 \mu\text{m}$ , widely tunable cw lasers are available using difference frequency generation in nonlinear optical materials, such as periodically poled lithium niobate (PPLN). These crystals can also be used to create optical parametric oscillators (OPOs), which are now commercially available and produce infrared light at powers greater than 1 W. For spectroscopy beyond  $5 \mu\text{m}$ , there are few cw laser sources available. In recent years, quantum cascade lasers (QCLs) have emerged as the leading solution for performing high-resolution spectroscopy in the mid-IR. Though individual QCLs are generally only narrowly tunable, they can be engineered to emit light throughout the mid-IR, making them useful for measuring a wide variety of molecular targets throughout the mid-IR from  $4\text{--}10 \mu\text{m}$  and beyond. The work presented in this dissertation details the development and use of a QCL-based infrared spectrometer which operates near  $8.5 \mu\text{m}$ .

The QCL spectrometer has been developed with the goal of recording a rotationally-resolved gas phase spectrum of buckminsterfullerene ( $\text{C}_{60}$ ), but has also proved useful for performing high-resolution spec-

troscopy of a variety of molecules with vibrational bands in the  $8.5 \mu\text{m}$  region of the infrared spectrum. In particular, the spectrometer has been used to observe another large molecule, pyrene ( $\text{C}_{16}\text{H}_{10}$ ), which has been used as a stepping stone on the way to the ultimate goal of observing  $\text{C}_{60}$ . While this molecule is of intermediate size in comparison to  $\text{C}_{60}$ , it is the largest molecule which has been observed to date with rotational resolution by absorption spectroscopy. The spectrometer has also been used to observe rotationally resolved spectra of deuterated water clusters, as the bending mode of  $\text{D}_2\text{O}$  lies in the  $8.5 \mu\text{m}$  region of the spectrum, near the expected position of the  $\text{C}_{60}$  absorption band. Rotationally-resolved spectra of the Ar- $\text{D}_2\text{O}$  van der Waals cluster have been obtained and analyzed, and the bending mode of the deuterated water dimer has been observed for the first time with rotational resolution.

The spectrometer which was used to perform all of the work in this dissertation (with the exception of the work in Chapter 5) is based on liquid nitrogen-cooled Fabry Perot QCLs which were provided to us by the group of Claire Gmachl at Princeton. The spectrometer is described in detail in the papers which are included in this dissertation as Appendices B and C, and further details can be found in the dissertation of Brian Brumfield, a recent graduate of the McCall group.[1]

## 1.1 Rotationally-resolved Spectroscopy of Large Molecules

Though the vast majority of high-resolution infrared spectroscopy focuses on small molecules ( $\lesssim 10$  atoms), there is a need to extend the techniques of rotationally-resolved IR spectroscopy to larger molecules. One driver of this is the field of astrochemistry, which seeks to understand the chemical environment present in astronomical objects. Because it is impossible to sample the chemical environment of distant objects directly, astronomers rely on spectroscopic observations to determine the composition and conditions of these objects. The workhorse of observational astronomy is pure rotational spectroscopy, but there are many interesting molecules which lack a permanent dipole moment and cannot be observed by this technique. Some of these molecules include linear carbon chains, symmetric fullerenes, and polycyclic aromatic hydrocarbons (PAHs). To observe these molecules, it is necessary to obtain high quality infrared or electronic spectra to compare to astronomical observations. Additionally, high-resolution spectra of large molecules provide benchmarks for theoretical calculations of these molecules, which can help refine theoretical approaches to calculating the properties of these molecules.

Obtaining a high-resolution spectrum of  $\text{C}_{60}$  is of particular interest because it would be the largest and most symmetric molecule to be observed with rotational resolution. Because of the high degree of symmetry in  $\text{C}_{60}$ , many rotational levels are forbidden due to restrictions of boson exchange symmetry. While these

forbidden levels have been predicted, a rotationally-resolved spectrum has not yet been measured to confirm the predictions.  $C_{60}$  is also of great interest from an astrochemical perspective.  $C_{60}$  has recently been detected in space by infrared emission spectroscopy in a wide variety of astronomical environments. Although the presence of  $C_{60}$  in astronomical environments has now been confirmed, it is not yet understood how or where  $C_{60}$  is formed. By obtaining a cold gas phase spectrum, it is hoped that additional observations of  $C_{60}$  by absorption spectroscopy can be made. Astronomical absorption spectra will allow observation of  $C_{60}$  in cold environments where  $C_{60}$  emission would not be observable. Absorption spectra will also give additional information about the temperature and density of environments where  $C_{60}$  is observed, which will aid in elucidating where and how  $C_{60}$  forms in space.

Obtaining high-resolution infrared spectra of large molecules presents a challenge for a variety of reasons. First, it is necessary to produce a gas phase sample in order to obtain rotationally-resolved spectra. The absorption features in a solid or liquid sample are simply too broad to allow individual rotational levels to be resolved. Small molecules are generally easy to produce in the gas phase, while larger molecules must be vaporized using either high temperatures or specialized techniques, such as laser ablation. Even using these techniques, there is often only a relatively small quantity of gas phase sample available to measure. A second challenge for high-resolution spectroscopy of large molecules is that large molecules have large moments of inertia, which means that they have small rotational constants. This makes it more difficult to resolve individual rotational transitions as they are closely spaced and the spectrum can be quite dense. (As an example of this spectral density, see Figure 3 in Appendix D, which shows a close-up view of the high-resolution spectrum of pyrene.) At high temperatures, the partition functions for large molecules are also quite large, leading to a dilution of the absorption signal into many different rotational states. An additional problem is the increased number of vibrational modes in large molecules. Because it is necessary to heat the samples to high temperatures to produce molecules in the gas phase, a large number of vibrational modes are thermally excited, making absorption spectroscopy of fundamental bands arising from the ground vibrational state much more challenging.

A key to overcoming these challenges is to take hot molecules which have been produced by heating a solid or liquid sample and to cool them to reduce the partition function and complexity of the spectrum. One of the most-utilized ways this is accomplished is through the technique of seeding the large molecules in a high pressure of a carrier gas (typically a noble gas, such as Ar) and sending the high pressure gas mixture through a small orifice into a low pressure chamber to produce a supersonic expansion. As the gas expands, it cools rapidly, and collisions of the carrier gas with the large molecule of interest cool the internal degrees of freedom. The cooled molecules have a significantly simpler spectrum as the higher energy rotational and

vibrational levels are depopulated. In Appendix D a supersonic expansion was successfully used to cool pyrene, a molecule with 26 atoms, to a rotational temperature of 23 K and a vibrational temperature of 23–111 K. Chapter 2 presents work done towards obtaining a cold, high-resolution spectrum of  $C_{60}$  using our QCL spectrometer. Unlike pyrene, we have found that  $C_{60}$  does not cool vibrationally by supersonic expansion, and a different approach to vaporizing  $C_{60}$  will be necessary to produce a cold, gas phase sample for spectroscopic study.

## 1.2 Spectroscopy of Deuterated Water Clusters

Water is a vitally important molecule in chemistry, and essential to life as we know it. The bulk properties of water are well characterized, but a detailed picture of the microscopic structure of liquid water is still a work in progress.[2] The hydrogen bonding interactions among water molecules lead to its unique properties, and also make it difficult to create an accurate theoretical description of liquid water. To better understand the intermolecular interactions that lead to this complexity, much work has been devoted to studying small, gas phase water clusters. Studying isolated water clusters gives detailed information on the interactions among a few water molecules, and by studying increasingly large clusters, a more accurate model of liquid water can be developed. The interaction of water with other species is also of vital importance in many areas of chemistry. To this end, small clusters of water combined with other atoms and molecules have also been extensively studied.

In particular, this dissertation presents rotationally-resolved spectroscopy of the bending modes of two important small water clusters: Ar- $D_2O$  and  $(D_2O)_2$ . Ar-water clusters have been extensively studied by high-resolution spectroscopy as a model of polar-nonpolar interactions. The work presented in Chapter 3, in conjunction with previous results published by Li et al.[3] have provided a detailed picture of the vibrational bands associated with the bending mode of Ar- $D_2O$ , which will aid in continued theoretical modeling of this system.

Experimental studies of gas phase water dimer play an especially important role in the development of accurate models of liquid water because of the importance of two-body interactions in creating these models. Chapter 4 details observations of the high-resolution spectrum of  $(D_2O)_2$  in the region of the bending mode of the hydrogen bond donor. Though there have been previous studies of the bending modes of  $(H_2O)_2$  at low resolution,[4] this work represents the first rotationally-resolved spectrum of a bending mode of water dimer. This work has helped to elucidate the effect of excitation of the bending mode on the tunneling which occurs in water dimer, and provides an accurate value of the gas phase frequency of the donor bending

vibration, which will aid in further theoretical efforts to model water dimer and larger water clusters.

### 1.3 External Cavity QCLs

As this dissertation shows, the QCL spectrometer in the McCall group has proven to be quite useful in performing high-resolution spectroscopy of a wide variety of molecular species. This work has gone forward despite the fact that the frequency tuning of the Fabry Perot QCLs we have been using is limited to, at most, 1180–1200  $\text{cm}^{-1}$ . Most QCLs are inherently only narrowly tunable, and are often used to measure a specific molecule. In recent years, QCLs with broad gain media have been developed to create more broadly tunable QCLs throughout the mid-IR. These broadband QCLs have been placed in external cavity configurations to create lasers capable of high power and significantly broader tunability than conventional QCLs. Chapter 5 outlines work which has been performed in collaboration with Gerard Wysocki at Princeton to construct an external cavity QCL (EC-QCL) system for use in our cavity ringdown spectrometer. The EC-QCL has been built and is capable of frequency tuning from 1135–1220  $\text{cm}^{-1}$ , which greatly enhances the capabilities of the QCL spectrometer. This new laser will allow us to perform high-resolution spectroscopy of many interesting species, including two molecules of particular fundamental interest:  $\text{CH}_5^+$  and  $\text{H}_5^+$ .

## Chapter 2

# Inefficient Vibrational Cooling of $C_{60}$ in a Supersonic Expansion

### 2.1 Introduction

Ever since its discovery in 1985,[5] buckminsterfullerene ( $C_{60}$ ) has been the subject of an enormous body of research (the publication of its discovery has been cited more than 8100 times at the time of writing according to Web of Science). One particular area of interest is the astrochemistry of  $C_{60}$ .  $C_{60}$  was long believed to be present in the interstellar medium (ISM), and has recently been detected via emission spectroscopy in the mid-infrared (mid-IR).[6, 7, 8, 9, 10, 11] Though  $C_{60}$  has been detected in the ISM, the mechanism by which it is formed is still under debate.[12] Obtaining an astronomical absorption spectrum of  $C_{60}$  would yield additional information about the abundance and temperature of  $C_{60}$  in the ISM, which could provide useful information in determining the formation mechanism. Unfortunately, astronomical searches for absorption from cold gas phase  $C_{60}$  are hampered by the lack of a high-resolution gas-phase laboratory spectrum of any of the four infrared active vibrational bands of  $C_{60}$ .

A rotationally-resolved spectrum of  $C_{60}$  would also be of great fundamental interest. The acquisition of such a spectrum would be a significant milestone in the field of molecular spectroscopy, as  $C_{60}$  would be the largest and most symmetric molecule to be observed with rotational resolution. In addition, due to boson exchange symmetry restrictions on the overall symmetry of the molecular wavefunction there are many rotational levels in the ground and vibrationally excited state that are rigorously forbidden to exist.[13, 14] Such missing levels will manifest as “gaps” in the normal progression of rovibrational lines.

Despite great interest in a high-resolution spectrum of  $C_{60}$ , a rotationally-resolved, gas-phase absorption spectrum of  $C_{60}$  has not yet been observed. There are several obstacles which must be overcome to record such a spectrum. First, it is difficult to generate a gas phase sample of  $C_{60}$ .  $C_{60}$  has negligible vapor pressure at room temperature and must be heated to temperatures in excess of 875 K to reach a vapor pressure on the order of 10 – 100 mTorr.[15] Second,  $C_{60}$  has 174 vibrational modes, which leads to a large vibrational partition function at even modest temperatures (see Figure 2.1). Cooling the vibrational degrees of freedom

---

This chapter is a preprint of a manuscript to be submitted to *Advances in Physical Chemistry*, authored by J. T. Stewart, B. E. Brumfield, B. M. Gibson, and B. J. McCall.

will be critical for observing a fundamental vibrational band. Finally, it is necessary to have a sensitive, high-resolution spectrometer in the mid-IR to observe the relatively small amount of gas-phase sample.

We have developed an experiment which attempts to address these obstacles. We have built a high-temperature oven source which has been used to generate  $C_{60}$  vapor. To attempt to relax the vibrational degrees of freedom, the hot  $C_{60}$  vapor has been cooled using a supersonic expansion. The supersonic jet is then probed using continuous wave cavity ringdown spectroscopy (cw-CRDS).[16] We have attempted to observe the  $8.5 \mu\text{m}$  band due to the availability of quantum cascade laser (QCL) sources at this wavelength, and also because this band coincides with an atmospheric window, permitting ground-based astronomical observations. The cavity ringdown spectrometer has already been tested by carrying out high-resolution spectroscopy of methylene bromide[17] and pyrene.[18] Despite multiple spectral searches under a variety of expansion source conditions, no absorption signals from  $C_{60}$  have yet been detected.

Previous work has shown effective vibrational cooling of large molecules (such as polycyclic aromatic hydrocarbons (PAHs)) in supersonic expansions.[18, 19, 20] In contrast to this previous work, our lack of signal indicates that the vibrational degrees of freedom are not effectively cooled in  $C_{60}$ . We will discuss the details of our experiment and also briefly discuss measurements of  $D_2O$  made in the heated oven, which show good rotational cooling, but no vibrational cooling. We will also compare our current experiment to the previous work showing good vibrational cooling of other large molecules. Finally, we will present possible alternative experiments which may allow observation of a high-resolution absorption spectrum of  $C_{60}$ .

## 2.2 Experimental

Our high-resolution mid-IR spectrometer has been described in detail previously,[16, 17] so here we present only a brief overview of the instrument. Mid-IR light near  $8.5 \mu\text{m}$  is generated using a QCL supplied by collaborators in the Gmachl group at Princeton. The frequency of the emitted light can be tuned from  $\sim 1180\text{-}1200 \text{ cm}^{-1}$  by changing the temperature of the laser and the current applied to the QCL. Light from the QCL is sent through an optical isolator to an optical cavity where we perform cw-CRDS to record the infrared absorption spectrum of our sample. To calibrate our spectra we utilize an absorption cell filled with  $SO_2$  to provide absolute frequency calibration and a mid-IR wavemeter for relative frequency calibration.

We have constructed a high-temperature oven which we used to produce gas-phase  $C_{60}$ . (This oven is described in detail in our previous work on pyrene[18].) The oven is made from stainless steel with attached strip heaters to provide heating and is capable of operating under vacuum at temperatures up to 975 K for many hours. To produce gas-phase  $C_{60}$  for spectroscopy, we loaded solid  $C_{60}$  (MER Corporation,

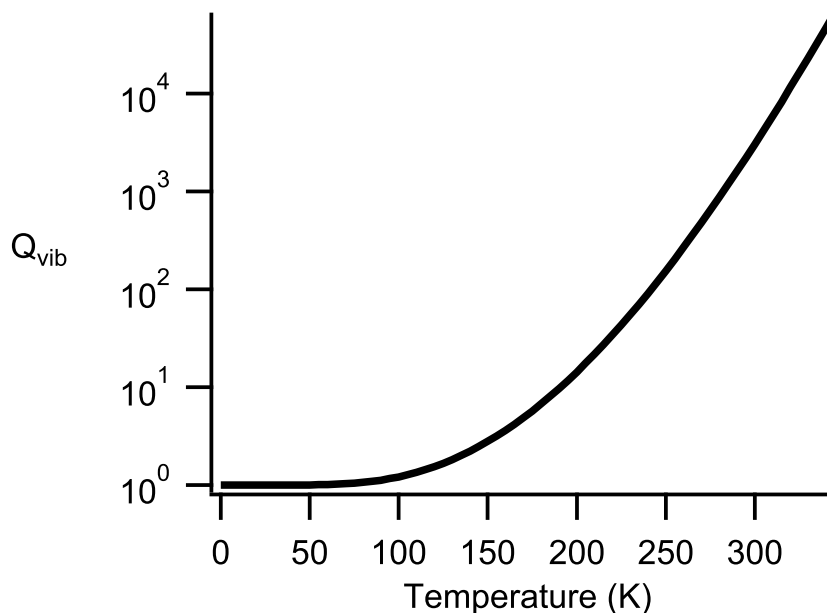


Figure 2.1: Plot of  $C_{60}$  vibrational partition function (on a logarithmic scale) versus temperature. The vibrational frequencies used in the calculation were obtained from Ref. [21].

99+% purity) into the oven, which was then placed in a vacuum chamber and surrounded by an aluminum heat shield. The oven was heated by applying current to the strip heaters using variable transformers, which gave us coarse control over the temperature of the oven. The oven temperature was monitored using a thermocouple inserted into the interior of the oven. Once we had achieved the desired temperature ( $\sim 950$  K) we flowed Ar through the oven and generated a continuous supersonic expansion of the Ar/ $C_{60}$  mixture through a  $12.7 \text{ mm} \times 150 \text{ }\mu\text{m}$  slit; the expansion was then probed with our spectrometer. Effective vaporization of  $C_{60}$  in the oven was verified by measuring the mass of  $C_{60}$  in the oven following a set of scans, and also by deposition of  $C_{60}$  on the walls of our vacuum chamber. As described in the next section, we anticipate that the absorption band should lie between  $1184\text{-}1186 \text{ cm}^{-1}$ , so our efforts have been directed at this frequency region.

### 2.3 Estimating Signal-to-Noise

Knowledge of where to scan in frequency space to detect the first signal from the  $8.5 \text{ }\mu\text{m}$  vibrational band of  $C_{60}$  is critical. Restricting the search window allowed us to focus on varying experimental parameters instead of trying to cover a large spectral region. The only gas phase measurements come from observations of infrared emission at  $\sim 1000$  K.[22, 23] The estimated band center position was  $1169.1 \text{ cm}^{-1}$ , [22] but this estimate is likely red-shifted due to the contribution from hot bands, whose emission frequencies are shifted

due to vibrational anharmonicity. Low-temperature (15 K) measurements of  $C_{60}$  films assign the center position to  $1183.7 \text{ cm}^{-1}$ , [24] while Ar matrix spectroscopy yields  $1184.8 \text{ cm}^{-1}$ . [25] Measurements in para- $H_2$  (p- $H_2$ ), considered the least perturbing matrix host, place the center position of the peak associated with the  $8.5 \mu\text{m}$  band at  $1184.7 \text{ cm}^{-1}$ . [14] Because the frequency shift between Ar and p- $H_2$  matrix hosts for a spectral feature is generally comparable to the frequency shift between gas-phase and p- $H_2$ , we feel confident that the peak of the  $8.5 \mu\text{m}$  absorption band should be near the p- $H_2$  matrix value of  $1184.7 \text{ cm}^{-1}$ .

We have simulated the  $8.5 \mu\text{m}$   $C_{60}$  vibrational band at high resolution, following the approach of Sogoshi et al. [14] As noted by Sogoshi et al., the appearance of the spectrum will be dependent on the change of the rotational constant from the ground to the excited vibrational state as well as the Coriolis coupling constant  $\zeta$ . If the change in rotational constant is small, there will be a prominent  $Q$ -branch. If the change is large (on the order of 1%), there could be a prominent  $R$ -branch head. Because we do not know if either of these cases will happen in the actual experimental spectrum, we base our S/N estimates on observing a single rovibrational transition. To estimate our expected signal, we use a theoretical value for the band strength of the  $8.5 \mu\text{m}$  band [26] of  $25 \text{ km/mol}$ . Our estimates assume a vibrational temperature of 0 K. We will discuss the importance of vibrational excitation in Sec. 2.5.

Estimating the expected S/N for  $C_{60}$  absorption using our experimental apparatus parallels calculations that we carried out to estimate vibrational cooling of pyrene in a previous publication. [18] We begin with the following formula for estimating the S/N for a single rovibrational transition:

$$S/N = \frac{n_z f S' L_{jet}}{\Delta\tilde{\nu}(\sigma_{NEA})} \quad (2.1)$$

In this equation,  $n_z$  is the number density of  $^{12}C_{60}$  in units of  $\text{cm}^{-3}$  at a distance  $z$  from the slit,  $f$  is the ratio of the line intensity for a single transition (factoring in Boltzmann statistics) divided by the sum of all the line intensities,  $S'$  is the calculated band strength in  $\text{cm/molecule}$ ,  $L_{jet}$  is the length of the expansion in  $\text{cm}$ ,  $\Delta\tilde{\nu}$  is the linewidth of the transition in  $\text{cm}^{-1}$ , and  $\sigma_{NEA}$  represents the noise equivalent fractional absorption of the spectrometer. By evaluating each of these parameters for our instrument and this band of  $C_{60}$ , we can calculate an expected S/N for our experiment.

To estimate the number density, we use the rate of mass loss from the oven per unit time, combined with the velocity of molecules in the expansion. We account for the fact that not all of the molecules in the expansion will overlap with the  $TEM_{00}$  mode of the cavity and be probed by our spectrometer and that only 51.5% of the sample is  $^{12}C_{60}$ . In our previous work with pyrene, we have measured that only  $\sim 20\%$  of the molecules in the expansion overlap with the  $TEM_{00}$  mode of the ringdown cavity. [18] Because there is

little expansion along the axis of the slit, we assume that  $L_{jet}$  equals the length of the slit (12.7 mm) and can find the number density of molecules probed by our spectrometer:

$$n_{probed} = \frac{0.20 \times 0.515 \times \dot{N}_{C_{60}}}{2\omega_0 \times L_{slit} \times v_{max}} \quad (2.2)$$

where  $\dot{N}_{C_{60}}$  is the rate of molecules lost from the oven per second,  $\omega_0$  is the beam waist of the TEM<sub>00</sub> mode,  $L_{slit}$  is the length of the slit, and  $v_{max}$  is the flow velocity of molecules in the expansion (for further details on the derivation of this expression, we refer readers to the Supporting Information for Ref. [18]). We estimate  $\dot{N}_{C_{60}}$  by measuring the amount of C<sub>60</sub> before and after heating the sample and recording the length of time for which the expansion was on.  $\omega_0$  can be calculated from the radius of curvature of our ringdown mirrors, the length of the cavity, and the wavelength of light in the cavity.[27] For our setup,  $\omega_0$  is equal to 1.1 mm.  $v_{max}$  for the expansion can be found from the temperature and mass of carrier gas atoms in the expansion.[28]

We can now use Equation 2.1 to calculate our expected S/N for the slit expansion, using a 0.0004 cm<sup>-1</sup> (12 MHz) linewidth, which we have observed in slit expansions of methylene bromide and pyrene.[17, 18] Figure 2.2 displays the estimated S/N for the entire vibrational band for the measured mass loss at 955 K (2 g/hr) with the slit 6 mm from the cavity axis. The largest estimated S/N for a single rovibrational transition is ~130 (for the  $P(60)$ ,  $Q(60)$ , and  $R(60)$  lines).

## 2.4 Results

### 2.4.1 Search for C<sub>60</sub> Spectrum

Our attempts to observe C<sub>60</sub> are summarized in Table 2.1. We also attempted 6 spectroscopic searches for C<sub>60</sub> using a smaller oven with both a slit and pinhole expansion, which are discussed in detail in Ref. [1], but the work presented here represents our best attempts with a high calculated S/N and complete frequency coverage of where the band is expected to be. We decided to use a slit expansion because of the narrower linewidth of transitions and the greater vibrational cooling due to the larger number of collisions that occur in a slit expansion. Our attempts were performed at three different backing pressures and all three attempts covered the entire frequency region between 1184-1186 cm<sup>-1</sup> where we expect to observe the C<sub>60</sub> vibrational band. All of our attempts had expected values of S/N > 70 but despite this, we saw no evidence of absorption due to C<sub>60</sub> in any of these searches. An example of our spectra is presented in Figure 2.3, which comes from attempt 3 in Table 2.1.

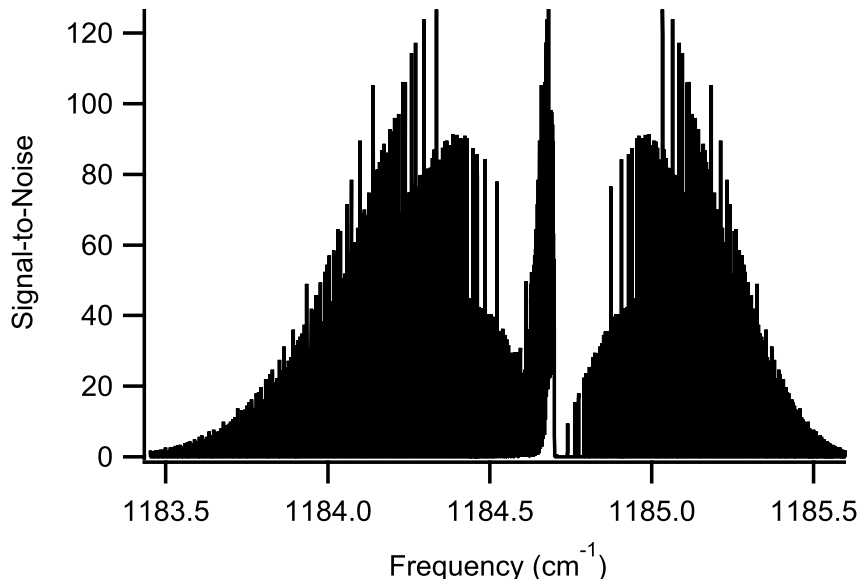


Figure 2.2: Plot of calculated signal-to-noise versus frequency. The signal-to-noise was calculated at  $T_{rot} = 20$  K,  $T_{vib} = 0$  K,  $B'' = 0.0028$  cm $^{-1}$ ,  $B' = 0.002795$  cm $^{-1}$ ,  $\zeta = -0.0319$ , oven temperature of 955 K, and a mass loss of 2.0 g/hr, corresponding to a probed number density of  $^{12}\text{C}_{60}$  in the expansion of  $1.7 \times 10^{12}$  cm $^{-3}$ . The assumed noise level was 1.0 ppm and the linewidth for the transitions was set to 0.0004 cm $^{-1}$ . The largest value of S/N for a single rovibrational transition is  $\sim 130$ . These parameters are similar to our experimental parameters for attempt 1 listed in Table 2.1. The value for  $\zeta$  comes from Ref. [29].

As can be seen in Table 2.1, the mass loss rate for our attempts decreased from attempts 1 and 2 to attempt 3, even though all three attempts were performed at approximately the same oven temperature. In a previous study on the thermal decomposition of  $\text{C}_{60}$ , Sundar et al. observed that  $\text{C}_{60}$  held at 975 K for an extended period of time (24 h) decomposed to amorphous carbon.[30] Other publications have also observed a similar reduction in vapor pressure over time when measuring the vapor pressure of  $\text{C}_{60}$  at elevated temperatures.[15, 31, 32] Our sample appears to be decomposing over time as we maintain it at high temperatures in the oven while scanning our spectrometer. The same sample was used for attempt 3 after it had been used for attempts 1 and 2, and the reduced mass loss rate for attempt 3 is indicative of this decomposition. We have also observed that after attempt 3, our sample is no longer soluble in toluene and has become conductive, even though pure  $\text{C}_{60}$  is an insulator. Further characterization by CHN analysis revealed that the recovered sample was  $\sim 89\%$  carbon by weight, with the elemental composition of the remaining mass as yet unknown. This implies that the actual mass of  $\text{C}_{60}$  lost over the course of attempts 1, 2 and 3 was higher than reported, but without elemental analysis between attempts we cannot say when this  $\text{C}_{60}$  mass loss occurred. Because of the decomposition of our sample, the reported S/N ratios in Table 2.1 represent average values for the expected S/N over the course of a scan, as the mass loss rate was decreasing as we were scanning our spectrometer.

Table 2.1: Summary of attempted absorption spectroscopy of  $C_{60}$ . The measured mass loss rate for each attempt was used to calculate S/N. The mass loss rates were 2.0 g/hr for attempts 1 and 2, and 0.7 g/hr for attempt 3. For all attempts, the supersonic expansion was probed 6 mm downstream from the exit of the slit.

Attempt	$T_0$ (K)	$P_0$ (torr)	NEA (ppm) <sup>a</sup>	Estimated S/N <sup>b</sup>
1	955	150	1.0	130
2	955	500	0.9	140
3	965	1900	0.6	74

<sup>a</sup> NEA = noise equivalent absorption

<sup>b</sup> These values represent the largest S/N value for a single rovibrational transition at  $T_{rot} = 20$  K and  $T_{vib} = 0$  K following the analysis presented in Sec. 2.3

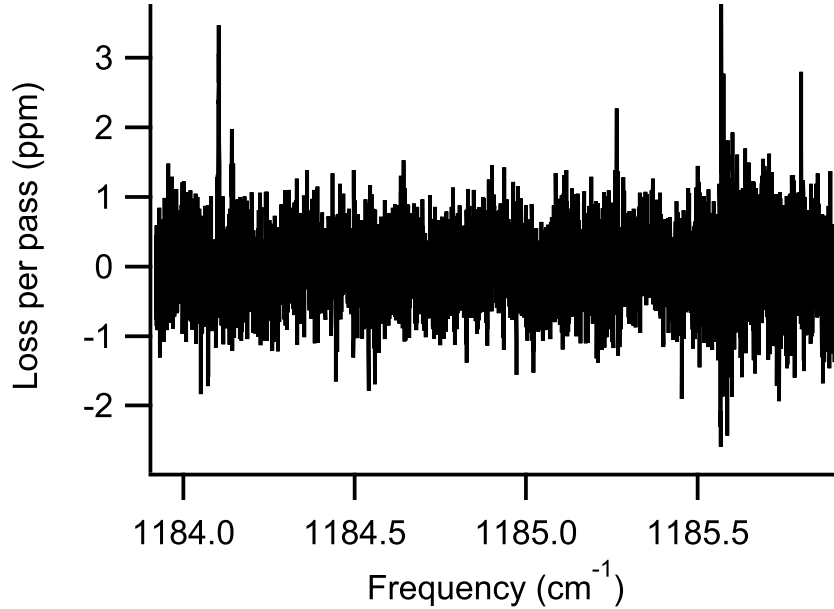


Figure 2.3: Representative absorption spectrum of the Ar/ $C_{60}$  expansion from 1184 – 1186  $cm^{-1}$ . This plot is from attempt 3 listed in Table 2.1. Baseline drifts have been corrected by use of polynomial fitting and subtraction. Periodic fringing was removed by Fourier transforming the spectrum, eliminating the most intense frequency components, and then inverse Fourier transforming the result to retrieve the spectrum. Similar data processing was used for all attempts where periodic fringing was observed. The spikes near 1185.6  $cm^{-1}$  are due to noise and were not reproducible. The line at 1184.1  $cm^{-1}$  is due to absorption by water vapor in the vacuum chamber. The standard deviation of the spectrum is 0.6 ppm.

### 2.4.2 High Temperature Measurements of D<sub>2</sub>O

Because of the high temperatures involved in producing gas-phase C<sub>60</sub>, we were concerned that the alignment of our optical cavity with our oven might be affected by thermal expansion or other heating effects. To eliminate this possibility, we observed absorption spectra of D<sub>2</sub>O in expansions from our oven at similar temperatures as our C<sub>60</sub> searches. There are many lines of the bending mode as well as a hot band within the spectral coverage of our spectrometer, which also allowed us to monitor the rotational and vibrational temperature of D<sub>2</sub>O molecules in the high temperature supersonic expansion.

We introduced a small amount of D<sub>2</sub>O into an Ar slit expansion and observed low-lying states which were populated in the expansion. We observed the  $1_{11} \leftarrow 0_{00}$  transition of the  $(010) \leftarrow (000)$  band of D<sub>2</sub>O at 1199.79 cm<sup>-1</sup> with the oven at 875 K to determine if alignment effects could be responsible for us not observing C<sub>60</sub>. We were easily able to observe the line in the expansion, and displacing the oven vertically only caused a slight change in the intensity of the line, consistent with the molecular distribution we measured with pyrene. This indicates that the extreme temperatures of our oven are not affecting the alignment of our ringdown cavity to prevent us from observing C<sub>60</sub>.

Measuring several transitions of D<sub>2</sub>O in the expansion from the hot oven also allowed us to calculate both the rotational and vibrational temperatures for D<sub>2</sub>O. Table 2.2 presents a list of the transitions that we measured in the  $(010) \leftarrow (000)$  and  $(020) \leftarrow (010)$  vibrational bands of D<sub>2</sub>O. Each line was measured 5 times and the average intensity for each line was used for all temperature calculations. Figure 2.4 shows a Boltzmann plot for both the fundamental and hot band transitions, showing that the rotational temperature of the D<sub>2</sub>O molecules is ~20 K in both the ground and excited vibrational states. From this we see that even though the expansion originated in an oven at 875 K, the rotational degrees of freedom are cooled efficiently. On the other hand, the strength of the hot band lines is consistent with a vibrational temperature >1000 K. The hot vibrational temperature for D<sub>2</sub>O is not surprising, considering that the lowest energy vibration in the molecule lies at ~1178 cm<sup>-1</sup>. Even at an oven temperature of 875 K, this is almost twice the value of  $k_B T$  (608 cm<sup>-1</sup> at 875 K), and vibrational modes with energies significantly higher than  $k_B T$  do not effectively relax to the ground vibrational state in a supersonic expansion.[33]

## 2.5 Discussion

From the discussion in section 2.3, we can see that if the C<sub>60</sub> molecules are cooled vibrationally in the supersonic expansion, we would anticipate observing an absorption signal even if there is not a strong *R*-branch head or *Q*-branch. Therefore, the most likely explanation for our lack of observed signal is that we

Table 2.2: List of observed D<sub>2</sub>O transitions. Rotational levels are denoted in the usual way ( $J_{K_a, K_c}$ ). The listed frequencies are from Refs. [34] and [35].

Vibrational Band	Transition	Frequency (cm <sup>-1</sup> )
(010) ← (000)	1 <sub>11</sub> ← 0 <sub>00</sub>	1199.793
	2 <sub>02</sub> ← 1 <sub>11</sub>	1194.038
	2 <sub>11</sub> ← 2 <sub>02</sub>	1193.255
	3 <sub>12</sub> ← 3 <sub>03</sub>	1198.536
(020) ← (010)	1 <sub>11</sub> ← 0 <sub>00</sub>	1181.311
	3 <sub>13</sub> ← 2 <sub>02</sub>	1199.154
	2 <sub>20</sub> ← 2 <sub>11</sub>	1192.497
	2 <sub>21</sub> ← 2 <sub>12</sub>	1199.690
	4 <sub>04</sub> ← 3 <sub>13</sub>	1198.379

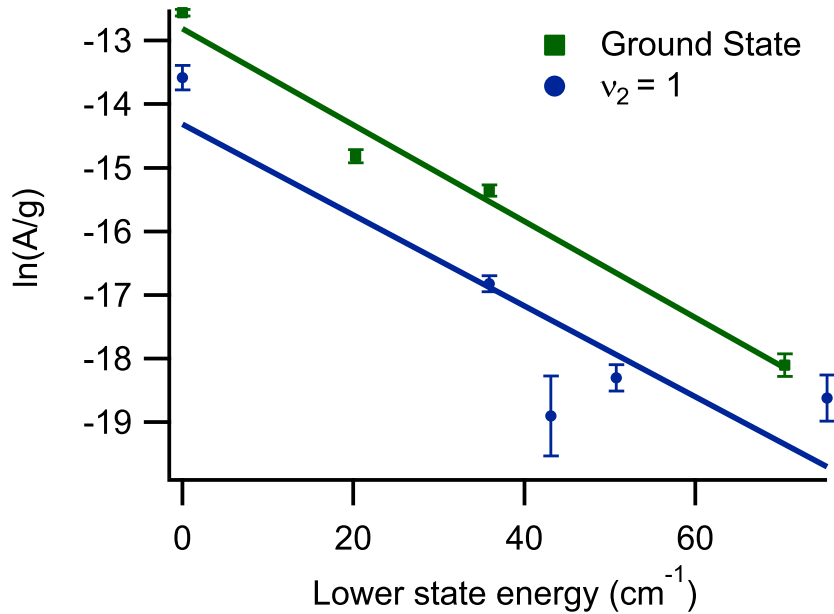


Figure 2.4: Boltzmann plot of D<sub>2</sub>O rotational levels observed in the supersonic jet at 875 K. The error bars indicate 3 $\sigma$  deviations from the average for each data point. The calculated rotational temperatures from the linear fits are 19 $\pm$ 2 K for the ground vibrational state (green squares) and 20 $\pm$ 6 K for the  $\nu_2=1$  vibrational state (blue circles). The uncertainties in the temperatures are 1 $\sigma$  values.

are not achieving sufficient vibrational cooling of C<sub>60</sub>. For us to observe absorption from the C<sub>60</sub> molecules, they must be in the ground vibrational state. The fraction of molecules in the ground vibrational state (assuming a Boltzmann distribution) is given by the expression:

$$f_0 = \frac{e^{-E_0/(k_B T_{vib})}}{Q_{vib}} \quad (2.3)$$

where  $E_0$  is the energy of the ground vibrational state,  $T_{vib}$  is the vibrational temperature, and  $Q_{vib}$  is the vibrational partition function. If we express the vibrational energies relative to  $E_0 = 0$ , Eq. 2.3 simply becomes the inverse of the partition function. Because C<sub>60</sub> has 174 vibrational degrees of freedom, its vibrational partition function increases rapidly with increasing temperature (see Figure 2.1), meaning very few molecules occupy the ground vibrational state at high temperatures. Even at a vibrational temperature as low as 190 K, only 1 in 10 C<sub>60</sub> molecules will be in the ground vibrational state, leading to an order of magnitude decrease for an absorption signal. If we assume that the lack of vibrational cooling is the primary cause preventing us from observing C<sub>60</sub>, we can calculate a lower limit for  $T_{vib}$  in the expansion using our expected S/N and Equation 2.3. Our expected signal is proportional to  $f_0$ , so if our expected S/N is 140 (as in attempt 2 in Table 2.1),  $f_0$  must be decreased by at least a factor of 140 for us to not observe the signal. This means that  $Q_{vib}$  must be at least 140, which would correspond to  $T_{vib} \simeq 250$  K. It should be noted that this lower limit of 250 K assumes a Boltzmann distribution for the vibrational levels, which is likely not the case in a supersonic expansion.

Previous studies have shown that large molecules (specifically PAHs) can be effectively cooled in supersonic expansions.[19] Our own recent measurements of pyrene using the experimental setup described in this paper indicated that pyrene was cooled to  $T_{vib} = 23 - 111$  K.[18] It is useful to compare these previous studies with our current attempted spectroscopy to ascertain why we were unable to observe C<sub>60</sub> absorption in our expansion.

Vibrational cooling of large molecules seeded in a supersonic expansion of a monatomic carrier gas proceeds by transferring vibrational energy from the large molecule to translational energy in the expansion by collisions with the carrier gas (V-T transfer). Because of this, the number of collisions that a molecule experiences in the supersonic expansion will have a significant effect on the amount of vibrational cooling that is possible in the expansion. We have estimated the number of two-body hard sphere collisions which occur in our attempted C<sub>60</sub> spectroscopy and previous work on PAHs by our group[18] and Amirav et al.[19] The estimated number of collisions for our work and Amirav et al.'s work is found in Table 2.3. The details of our calculations are outlined in the following paragraphs.

Table 2.3: Estimated number of two body hard sphere collisions experienced by large molecules seeded in an argon supersonic expansion. The first three entries in the table are from the attempted C<sub>60</sub> spectroscopy reported in this work. The pyrene entry is from our previous work observing pyrene in the same experimental setup which we used to attempt C<sub>60</sub> spectroscopy.[18] The remaining entries are from laser induced fluorescence spectroscopy of the listed PAHs performed by Amirav et al.[19] The listed pressures for the PAHs were sufficient to produce vibrationally cold molecules ( $T_{vib} \lesssim 100$  K). The C<sub>60</sub> and pyrene expansions used a 12.7 mm  $\times$  150  $\mu$ m slit. For Amirav et al.’s work, all expansions used a 150  $\mu$ m diameter pinhole. Further details on how the number of collisions was calculated can be found in the article text.

Molecule	$T_0$ (K)	$P_0$ (torr)	Nozzle type	Number of collisions
C <sub>60</sub> (att. 1)	955	150	slit	320
C <sub>60</sub> (att. 2)	955	500	slit	1100
C <sub>60</sub> (att. 3)	965	1900	slit	4000
pyrene	430	150	slit	560
anthracene	410	270	pinhole	600
tetracene	485	175	pinhole	360
pentacene	550	250	pinhole	500
ovalene	630	300	pinhole	620

The first step in estimating the number of collisions in a supersonic expansion is to describe the temperature, density, and velocity of molecules in the expansion. These properties are given by the following equations for the centerline of the expansion, which are reproduced from Ref. [36]:

$$T(z) = T_0 \left(1 + \frac{\gamma - 1}{2} M^2\right)^{-1} \quad (2.4)$$

$$n(z) = n_0 \left(1 + \frac{\gamma - 1}{2} M^2\right)^{-\frac{1}{\gamma - 1}} \quad (2.5)$$

$$v(z) = M \sqrt{\frac{\gamma k_B T_0}{m}} \left(1 + \frac{\gamma - 1}{2} M^2\right)^{-\frac{1}{2}} \quad (2.6)$$

In these equations,  $z$  represents the distance from the nozzle along the centerline of the expansion,  $T_0$  and  $n_0$  are the temperature and number density of the gas prior to the expansion,  $\gamma$  is the heat capacity ratio (which is 5/3 for the argon expansions we consider here),  $M$  is the Mach number of the expansion, and  $m$  is the mass of the gas. Because the large molecule is only a minor constituent of the gas being expanded, we assume that the properties of the expansion can be approximated as that of a pure argon expansion. To use these equations, we also need to know the value of  $M$  as a function of  $z$ ; equations to do so for both slit and pinhole expansion sources are provided in Ref. [36].

The next step in calculating the number of collisions is to calculate the mean free path of the large molecules in the expansion. To do so, we use a hard sphere model, which gives the usual equation:

$$\lambda(z) = \frac{1}{\sqrt{2}\pi(r_{large} + r_{Ar})^2 n(z)} \quad (2.7)$$

Table 2.4: Hard sphere radii used to compute the mean free path of molecules in the supersonic expansion.

Species	Radius (Å)
Ar	1.88
C <sub>60</sub>	5.0
pyrene	4.0
anthracene	3.8
tetracene	4.2
pentacene	4.6
ovalene	5.1

where  $\lambda(z)$  is the mean free path as a function of distance from the expansion nozzle and  $r_{large}$  and  $r_{Ar}$  are the hard sphere radii for the large molecule and argon atoms, respectively. Because C<sub>60</sub> is roughly a sphere, we can simply use the van der Waals radius of C<sub>60</sub> for  $r_{large}$  in this equation, but the PAHs studied by us and Amirav et al. are far from spherical. To get a rough approximation of a hard sphere radius for these species, we used values for the minimum and maximum projected cross sections of the molecules as given in the chemicalize.org database from ChemAxon.[37] To obtain a hard sphere radius, we averaged the minimum and maximum projected cross sections for the PAHs, and then calculated an effective radius based on the average cross section of the molecule. While this is certainly not exact, it should give a rough estimate of the relative size of the PAHs for computing the mean free path, and seems to give reasonable results. The hard sphere radii which we used to compute the mean free path are listed in Table 2.4.

We can then calculate the average frequency of two-body collisions of the large molecule with Ar atoms in the expansion by dividing the average speed of the molecules by the mean free path. We assume that the translational temperature of the large molecules is thermalized with the translational temperature of the Ar atoms and calculate the average speed according to:

$$s(z) = \sqrt{\frac{8k_B T(z)}{\pi \mu}} \quad (2.8)$$

where  $\mu$  is the reduced mass of the Ar and large molecule. Using the above equations, we can calculate the collision frequency at any point  $z$  along the centerline of the expansion. We calculated the collision frequency in steps of 1.5  $\mu\text{m}$  from  $z = 0$  to 6 mm along the expansion for all of the molecules and conditions listed in Table 2.3. We then calculated the number of collisions at each point by calculating the velocity of the expansion to determine how long the molecules were within each 1.5  $\mu\text{m}$  section, and then multiplying that time by the collision frequency. We then added together the number of collisions calculated for each of these 1.5  $\mu\text{m}$  sections from  $z = 0$  to 6 mm to give the total number collisions listed in Table 2.3. We use a maximum of 6 mm because that is where the expansion was probed in our work and in Amirav et al.'s work.

From Table 2.3, we can see that the PAHs were vibrationally cooled after undergoing an average of 360–620 collisions with Ar. In our attempted  $C_{60}$  spectroscopy, the  $C_{60}$  molecules underwent an average of 320, 1100, and 4000 collisions with Ar for attempts 1, 2, and 3 in Table 2.1, respectively. For attempts 1 and 2, the number of collisions is similar to the number of collisions for the PAH molecules, while the much higher backing pressure for attempt 3 leads to about an order of magnitude more collisions. While the  $C_{60}$  molecules underwent a similar number of collisions as the PAHs, or significantly more for attempt 3, we have seen that this was insufficient to produce vibrationally cold  $C_{60}$ , which would have been observable with our spectrometer. To try to understand why this might be the case, we can compare the vibrational properties of these molecules.

Theoretical harmonic vibrational frequencies for all of the PAHs listed in Table 2.3 can be found in the PAH IR Spectral Database[38], which come from the original data of Langhoff.[39] We have used these vibrational frequencies to calculate the vibrational partition functions of the PAHs and  $C_{60}$  at high temperature before being cooled by supersonic expansion. Using the vibrational partition function, we can also calculate the amount of vibrational energy in an average molecule at high temperature. These values are presented in Table 2.5 for all of the molecules we have been considering. The first thing to notice is the incredibly large partition functions for these molecules at elevated temperatures, especially for  $C_{60}$  and ovalene. According to Eq. 2.3, this means that on average only 1 in  $10^{28}$  molecules of  $C_{60}$  is in the ground vibrational state before the expansion. Table 2.5 also shows that these molecules have a large amount of vibrational energy (over  $50000\text{ cm}^{-1}$  for  $C_{60}$ ) that must be transferred into the supersonic expansion to cool them vibrationally. For the PAHs, we have seen that it is possible to transfer this energy in the hundreds of collisions that occur in the expansion. We can divide the vibrational energies in Table 2.5 by the collision numbers in Table 2.3 to calculate an energy to collision ratio to get an idea of how much energy would need to be removed in an average collision to cool the molecule. This ratio is listed in the last column of Table 2.5. For the vibrationally cold PAH molecules, an average collision carried away 5–30  $\text{cm}^{-1}$  of energy. For our attempted  $C_{60}$  spectroscopy, the energy to collision ratio is significantly higher than this for attempt 1, slightly higher for attempt 2, and right in the range of the PAHs for attempt 3.

Looking at these values, it is somewhat surprising that  $C_{60}$  was not efficiently cooled using a supersonic expansion for attempts 2 and 3. Considering the previous work with PAHs, it appears that there should be enough collisions to carry away the vibrational energy for these attempts. One possible reason why  $C_{60}$  was not efficiently cooled is that the lowest energy vibrational mode for  $C_{60}$  is at  $267\text{ cm}^{-1}$ , which is significantly higher than the lowest modes for the PAHs (see Table 2.5). To completely cool the molecule to the ground vibrational state, energy must be transferred from the lowest vibrational mode into translational energy.

Table 2.5: Vibrational partition function, average vibrational energy (above zero-point energy) in  $\text{cm}^{-1}$ , frequency of the lowest energy vibrational mode, and energy to collision ratio for the molecules listed in Table 2.3 at the temperatures listed in that table. The calculated values for our  $\text{D}_2\text{O}$  measurements from section 2.4.2 are also included for comparison.

Molecule	$Q_{vib}$	$E_{vib}$ ( $\text{cm}^{-1}$ )	$\nu_{min}$ ( $\text{cm}^{-1}$ )	$\frac{E_{vib}}{\text{collisions}}$
$\text{C}_{60}$ (att. 1)	$1.3 \times 10^{28}$	56000	267	174
$\text{C}_{60}$ (att. 2)	$1.3 \times 10^{28}$	56000	267	50
$\text{C}_{60}$ (att. 3)	$3.0 \times 10^{28}$	57000	267	14
pyrene	$4.0 \times 10^3$	4000	99	7
anthracene	$1.5 \times 10^3$	3200	91	5
tetracene	$1.0 \times 10^6$	6400	56	18
pentacene	$2.5 \times 10^9$	10000	38	21
ovalene	$8.6 \times 10^{13}$	18000	61	29
$\text{D}_2\text{O}$	1.20	260	1178	0.8

The efficiency of V-T transfer decreases as the energy gap increases, making it more difficult for modes with higher energy to be completely cooled. As an extreme example of this, we can consider the  $\text{D}_2\text{O}$  spectroscopy presented in Sec. 2.4.2. We have calculated the vibrational properties for  $\text{D}_2\text{O}$  following the same procedure as for  $\text{C}_{60}$  and the PAHs, using vibrational frequencies from Ref. [40]. The results are listed in Table 2.5, and show that the amount of vibrational energy for a small molecule at high temperature is much lower than the large molecules we have been considering. At a temperature of 875 K and a backing pressure of  $\sim 300$  torr, the average number of hard sphere collisions for a  $\text{D}_2\text{O}$  molecule in the expansion is 310 (using a hard sphere radius of 1.6 Å), which gives an energy to collision ratio of 0.8. Even though this ratio is significantly lower than for all of the PAHs, we observed substantial population in the (010) state, indicating no cooling of this vibrational mode. This lack of cooling is a direct consequence of the fact that the lowest energy mode lies so high in energy.

Another possibility is that the extremely large size of  $\text{C}_{60}$  is causing a significant velocity slip effect to occur because of the large difference in mass between the  $\text{C}_{60}$  molecules and the Ar carrier gas.[19] While this does not seem to be a problem for the previous work on ovalene,  $\text{C}_{60}$  is about 2 times heavier than ovalene. This problem would be easily remedied by using a heavier carrier gas such as Kr or Xe, which would more closely match the mass of  $\text{C}_{60}$ . We did not try a heavier gas because of the increased cost of these gases compared to Ar, especially when used continuously, as in our experiment. For future attempts to observe  $\text{C}_{60}$ , it may be worth the extra expense to try the heavier rare gases to reduce the velocity slip effect.

Finally, it is worth noting that other molecules have been observed to have anomalously low cooling efficiency in supersonic expansions. In particular, Sulkes observed that benzene displays a lack of collision-induced vibrational relaxation in He and Ar expansions, despite the fact that substituted benzene derivatives

showed excellent cooling under similar conditions.[41] Sulkes attributed this to a lack of efficient cooling via orbiting resonances; it is conceivable that a similar effect is occurring with  $C_{60}$ .

## 2.6 Alternative Experiments

It would be preferable to produce  $C_{60}$  vapor at a much lower temperature than is possible in our oven. Doing so would significantly decrease the vibrational partition function and vibrational energy of the molecules prior to the supersonic expansion. For example, if  $C_{60}$  vapor could be produced at a temperature similar to our pyrene work (430 K) then the vibrational partition function would be only be  $5 \times 10^7$  and an average molecule would only have  $11000 \text{ cm}^{-1}$  of vibrational energy, which would be quite similar to the PAHs that were observed by Amirav et al. This should make it much easier to cool the  $C_{60}$  molecules to the ground vibrational state.

We have identified two possible methods for producing  $C_{60}$  vapor at lower temperatures; the first is the expansion of a supercritical fluid containing dissolved  $C_{60}$ . It has been demonstrated that  $C_{60}$  can be dissolved in supercritical toluene, or to a lesser extent in supercritical carbon dioxide containing toluene as a co-solvent.[42, 43] Assuming a 1:1 volume ratio of  $CO_2$  to toluene, the critical temperature is  $\sim 450 \text{ K}$ . Decreasing the toluene content will lower the critical temperature, though this would be at the expense of solubility. It will be necessary to optimize the toluene content for our particular needs. We would likely employ an argon sheath-flow continuous expansion source, as in Ref. [44].

Another alternative is a laser desorption source. Although a laser desorption/supersonic expansion source has been successfully employed for resonant two-photon ionization measurements of  $C_{60}$ ,[45] the vibrational temperature of the vapor produced was not directly observed. Likewise, while it has been shown that laser desorption can volatilize large molecules with pre-expansion vibrational temperatures below what one would expect for thermal vaporization,[46, 47] the temperatures achievable are molecule- and surface-dependent and as yet unknown for  $C_{60}$ . As such, the viability of a laser desorption source is difficult to assess without further experiments.

Although we expect either of these sources to be superior to our current oven in terms of vibrational temperature, we also expect them to produce significantly lower number densities of  $C_{60}$ . Based on reports of supercritical fluid extractions of  $C_{60}$ ,[42, 43] we anticipate that the number density produced by a supercritical fluid expansion would be two orders of magnitude lower than that of our current oven. Assuming  $C_{60}$  can cool efficiently, we will need to implement high repetition rate cavity ringdown spectroscopy[48] to account for the decrease in sample. Depending on the repetition rate achieved, doing so would improve

signal-to-noise by a factor of 10 – 20. If  $C_{60}$  does not cool completely or the number density is lower than anticipated, noise-immune cavity-enhanced optical heterodyne molecular spectroscopy (NICE-OHMS) detection could be implemented instead, improving our signal to noise ratio by as much as three orders of magnitude.[49] This route would also significantly increase the technical complexity of our spectrometer.

## 2.7 Conclusions

Obtaining a high-resolution gas phase spectrum of  $C_{60}$  represents a significant challenge for molecular spectroscopy. We have attempted to obtain such a spectrum using a highly sensitive cw-CRDS spectrometer, but were unable to detect any absorption signal from  $C_{60}$ . We have shown that an absorption signal should be expected with our current experimental setup if we are able to vibrationally cool  $C_{60}$ . Our lack of signal is most likely due to the fact that we must heat our sample to  $>950$  K to obtain sufficient vapor pressure for spectroscopy, which leads to an incredibly large vibrational partition function because of the large size of  $C_{60}$ . We have compared these results with previous work that has shown efficient vibrational cooling of large polycyclic aromatic hydrocarbons. To overcome this problem it will be necessary to produce gas phase  $C_{60}$  at much lower temperatures so that the vibrational degrees of freedom can be cooled. It may be possible to do this by using an expansion of  $C_{60}$  dissolved in supercritical fluid or by use of laser desorption methods.

## Chapter 3

# High-resolution Infrared Spectroscopy of the Bending Mode of Ar-D<sub>2</sub>O

### 3.1 Introduction

The interaction of water with itself and other molecules plays a key role in many diverse chemical environments, such as biochemical systems and solution phase chemistry. Because of the importance of these interactions, much work has been devoted to gaining a detailed understanding of them through simple model systems such as rare gas-water clusters. In particular, Ar-H<sub>2</sub>O and Ar-D<sub>2</sub>O have been extensively studied through high-resolution microwave,[50, 51] far-infrared,[52, 53, 54, 55, 56] and infrared[57, 58, 59, 60, 3] spectroscopy. This work has shown that the water molecule acts as a nearly free rotor within the Ar-water complex. The data from these spectroscopic studies were used by Cohen and Saykally to generate an empirical intermolecular potential energy surface for the Ar-water complex.[61] More recently, Makarewicz has generated an *ab initio* potential energy surface for various rare gas-water complexes, including Ar-H<sub>2</sub>O.[62]

In this article, we present rovibrational spectra of Ar-D<sub>2</sub>O in the region of the  $\nu_2$  bending mode of D<sub>2</sub>O, which expands on the previous work of Li et al.,[3] who recently reported three rovibrational bands of Ar-D<sub>2</sub>O in this region. In the present work, we provide additional data for one of these previously observed bands and also report three new bands which have not previously been observed.

### 3.2 Experimental

Our quantum cascade laser (QCL) spectrometer has been described in detail previously,[16, 17] but we briefly summarize the instrument here. We generate mid-IR light using a liquid nitrogen cooled Fabry-Perot QCL provided by the Gmachl group at Princeton. By varying the temperature and current applied to the QCL, the frequency can be tuned from  $\sim 1180 - 1200 \text{ cm}^{-1}$ , allowing us to observe the strongest bands of Ar-D<sub>2</sub>O. The light is sent to an optical cavity, where we perform continuous wave cavity ringdown spectroscopy (cw-CRDS) to obtain an absorption spectrum of the clusters. We calibrate the frequency of our laser using a

---

This chapter has been adapted from J. T. Stewart and B. J. McCall, *J. Mol. Spectrosc.* **282**, 34 (2012), Copyright 2012, Elsevier, Inc.

mid-IR wavemeter (Bristol) and SO<sub>2</sub> absorption lines contained in the HITRAN database.[63] We estimate that our absolute frequency accuracy is  $\sim 0.0005 \text{ cm}^{-1}$  (15 MHz).

Ar-D<sub>2</sub>O clusters are generated by bubbling Ar through room temperature D<sub>2</sub>O (Cambridge Isotope Laboratories) and then expanding the gas mixture through a  $150 \mu\text{m} \times 1.2 \text{ cm}$  slit to generate a continuous supersonic expansion. The flow rate of Ar through the system was controlled by a mass flow controller (MKS Instruments). The backing pressure behind the nozzle was measured using a pressure gauge on the input line into the vacuum chamber and typically ranged from 300–400 torr, though some data were acquired using backing pressures up to  $\sim 700$  torr. The vacuum chamber was pumped by a Roots blower and rotary vane pump (Oerlikon-Leybold). While the gas was flowing, the background pressure in the chamber was measured to range from 100–175 mTorr.

### 3.3 Results and Discussion

In the frequency region from 1180–1200  $\text{cm}^{-1}$  we have observed six rovibrational bands of Ar-D<sub>2</sub>O, three of which have been previously reported and analyzed by Li et al.[3] Here we present additional data for the  $\Pi(1_{10}, \nu_2 = 1) \leftarrow \Sigma(1_{01})$  band observed by Li et al.[3] near 1193  $\text{cm}^{-1}$  and for three additional bands which have not previously been reported.

All bands were fit using PGOPHER[64] by treating Ar-D<sub>2</sub>O as a pseudo-diatomic system, similar to Li et al.[3] and Zwart and Meerts.[56] The energy levels for all observed bands are expressed as

$$E(J) = \nu + BJ(J + 1) - D(J(J + 1))^2 + \dots \tag{3.1}$$

where  $\nu$  is the band origin,  $B$  is an effective rotational constant, and  $D$  is the effective quartic distortion constant. Fitting of all bands was complicated by the presence of Coriolis coupling between states with the same symmetry ( $e$  or  $f$ ) and internal rotor state.[59] As an example, the  $\Pi(1_{10}, \nu_2 = 1)$  state is actually comprised of two degenerate states with different symmetry, which we can label  $\Pi^e(1_{10}, \nu_2 = 1)$  and  $\Pi^f(1_{10}, \nu_2 = 1)$ . The  $\Pi^f(1_{10}, \nu_2 = 1)$  state participates in Coriolis coupling with the  $\Sigma^f(1_{10}, \nu_2 = 1)$  state, which lifts the degeneracy. Due to selection rules based on the symmetry of the states,[65]  $Q$ -branch transitions only occur between states with different symmetry ( $f \leftarrow e$  or  $e \leftarrow f$ ) and  $P$ - and  $R$ -branch transitions only occur between states of the same symmetry ( $e \leftarrow e$  or  $f \leftarrow f$ ). Because we do not have data on the  $\Sigma^f(1_{10}, \nu_2 = 1)$  state, we can only incorporate the effects of the Coriolis coupling into an effective rotational constant and fit the  $Q$ -branch separately from the  $P$ - and  $R$ -branches, which was also the approach taken by Li et al.[3] We follow this approach and report effective rotational constants for each symmetry state contained in a  $\Pi$

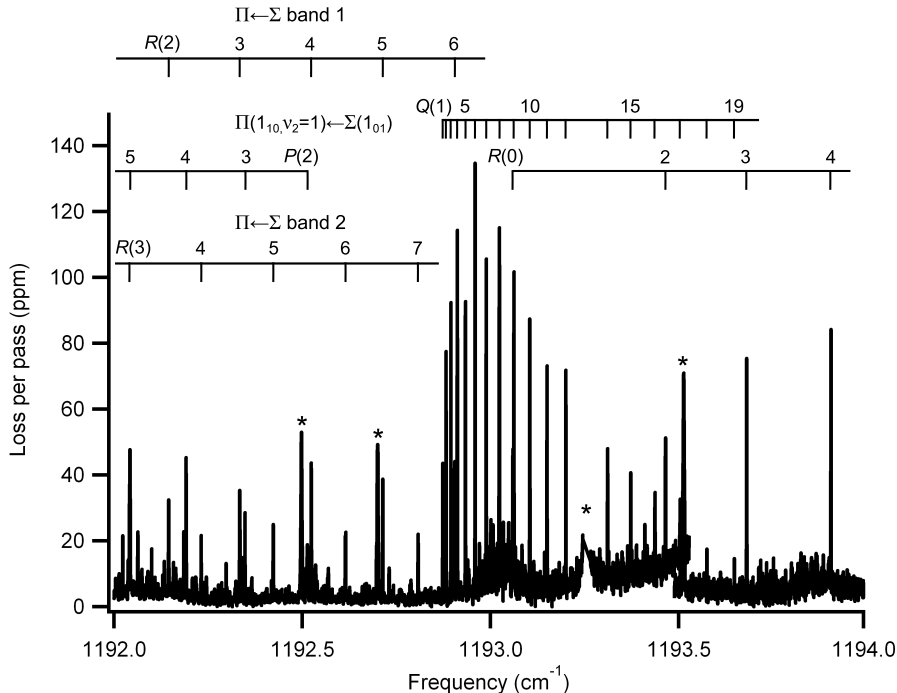


Figure 3.1:  $Q$ -branch region of the  $\Pi(1_{10}, \nu_2 = 1) \leftarrow \Sigma(1_{01})$  band, along with the beginning of the  $P$ - and  $R$ -branches. Additional lines are present from previously unobserved  $\Pi \leftarrow \Sigma$  bands. Lines marked with an asterisk(\*) are due to  $D_2O$  and  $HOD$  monomer. The very strong  $D_2O$  line near  $1193.25 \text{ cm}^{-1}$  has been removed for clarity. Other lines are due to  $(D_2O)_n$  clusters. The spectrum was collected at a backing pressure of  $\sim 300$  torr.

internal rotor state.

### 3.3.1 $\Pi(1_{10}, \nu_2 = 1) \leftarrow \Sigma(1_{01})$ band

As observed by Li et al.,[3] the strongest rovibrational band of *para* Ar- $D_2O$  is the  $\Pi(1_{10}, \nu_2 = 1) \leftarrow \Sigma(1_{01})$  band found near  $1193 \text{ cm}^{-1}$ . We have also observed this band and have been able to measure additional transitions beyond what Li et al. were able to obtain with their instrument. Figure 3.1 shows the  $Q$ -branch region of this band, along with the first few transitions of the  $P$ - and  $R$ -branches.  $R$ -branch transitions from additional  $\Pi \leftarrow \Sigma$  bands can also be seen which were not observed by Li et al.

We have fit the band using the approach outlined above, while fixing the constants for the  $\Sigma(1_{01})$  state to the values presented in Ref. [56]. The results of the fit are listed in Table 3.1 along with the previous results from Li et al. As can be seen in Table 3.1 our results differ from those obtained by Li et al. for the  $f$  state, which corresponds to the observed  $Q$ -branch transitions. The constants obtained by Li et al. fit well to the low  $J$   $Q$ -branch transitions, which were observed by Li et al., but at higher  $J$  values ( $\geq 14$ ), the fit diverges significantly. Because we were able to observe lines up to  $Q(19)$ , we were able to more accurately

Table 3.1: Comparison of molecular constants (in  $\text{cm}^{-1}$ ) for the  $\Pi(1_{10}, \nu_2 = 1) \leftarrow \Sigma(1_{01})$  band reported by Li et al.[3] and the present work. Values in parentheses represent one standard deviation from the least squares fit to the data.

Parameter	Li et al.[3]	Present work
$B''$		0.09103344(33) <sup>a</sup>
$D''(\times 10^6)$		1.7666(80) <sup>a</sup>
$\nu$	1192.86911(21)	1192.86863(25)
$B'(e)$	0.095237(20)	0.0952486(40)
$D'(e)(\times 10^6)$	2.01(30)	2.152(14)
$B'(f)$	0.0931767(63)	0.0932128(39)
$D'(f)(\times 10^6)$	1.857(33)	2.101(11)
$\sigma$	0.0004	0.0005

determine the constants for the  $f$  state, which fit both the low and high  $J$  transitions. A list of the observed transitions is presented in Table 3.2.

Table 3.2: Observed transitions for the  $\Pi(1_{10}, \nu_2 = 1) \leftarrow \Sigma(1_{01})$  band (in  $\text{cm}^{-1}$ ). Values in parentheses are residuals (observed - calculated) from the least squares fit.

Transition	Frequency
$P(12)$	1191.2468(11)
$P(11)$	1191.3351(8)
$P(10)$	1191.4317(4)
$P(9)$	1191.5364(-2)
$P(8)$	1191.6497(-8)
$P(7)$	1191.7727(-2)
$P(6)$	1191.9036(-2)
$P(5)$	1192.0424(-10)
$P(4)$	1192.1915(1)
$P(3)$	1192.3479(0)
$P(2)$	1192.5133(4)
$Q(1)$	1192.8734(4)
$Q(2)$	1192.8822(5)
$Q(3)$	1192.8950(3)
$Q(4)$	1192.9121(0)
$Q(5)$	1192.9335(-2)
$Q(6)$	1192.9592(-4)
$Q(7)$	1192.9888(-8)
$Q(8)$	1193.0231(-7)
$Q(9)$	1193.0625(4)
$Q(10)$	1193.1047(3)
$Q(11)$	1193.1504(0)

Table 3.2: (continued)

Transition	Frequency
$Q(12)$	1193.2004(-1)
$Q(14)$	1193.3113(-2)
$Q(15)$	1193.3728(4)
$Q(16)$	1193.4371(4)
$Q(17)$	1193.5042(0)
$Q(18)$	1193.5751(3)
$Q(19)$	1193.6481(-4)
$R(0)$	1193.0596(5)
$R(2)$	1193.4652(0)
$R(3)$	1193.6809(3)
$R(4)$	1193.9049(7)
$R(5)$	1194.1355(-4)
$R(6)$	1194.3753(-2)
$R(7)$	1194.6227(-4)
$R(8)$	1194.8789(6)
$R(9)$	1195.1413(0)
$R(10)$	1195.4100(-16)
$R(11)$	1195.6893(-1)
$R(12)$	1195.9746(2)
$R(13)$	1196.2664(0)
$R(14)$	1196.5652(0)
$R(15)$	1196.8710(3)
$R(16)$	1197.1826(-3)

### 3.3.2 $\Pi(1_{01}, \nu_2 = 1) \leftarrow \Sigma(1_{01})$ band

We observed a much weaker band near  $1189.4 \text{ cm}^{-1}$  with a distinct  $Q$ -branch, as can be seen in Figure 3.2. To determine the identity of this band, we can look at previous results in the far-IR. Zwart and Meerts observed two bands in their far-IR work, which they assigned as  $\Pi(1_{10}) \leftarrow \Sigma(1_{01})$  and  $\Pi(1_{01}) \leftarrow \Sigma(1_{01})$ . [56] Previous work with Ar- $\text{H}_2\text{O}$  showed that the bending vibration is only slightly affected by the presence of the Ar atom in the complex, [59] so we can estimate the locations of these bands in the infrared by simply adding the energy of the bending vibration to observed band origins observed in the far-IR. Doing this gives an estimated band origin of  $1192.6 \text{ cm}^{-1}$  for the  $\Pi(1_{10}, \nu_2 = 1) \leftarrow \Sigma(1_{01})$  band (which is close to the actual band origin of  $1192.87 \text{ cm}^{-1}$  we report in Table 3.1) and  $1189.5 \text{ cm}^{-1}$  for the  $\Pi(1_{01}, \nu_2 = 1) \leftarrow \Sigma(1_{01})$  band. This prediction lies only  $0.1 \text{ cm}^{-1}$  from the band presented in Figure 3.2, leading us to assign this band as  $\Pi(1_{01}, \nu_2 = 1) \leftarrow \Sigma(1_{01})$ .

The presence of a strong  $Q$ -branch is consistent with this assignment, but we have not observed any  $P$ - or  $R$ -branch transitions associated with this band. A possible  $R(0)$  line appears in Figure 3.2 near  $1189.59 \text{ cm}^{-1}$ , but was also present in expansions using He as the carrier gas, indicating that the line is due to

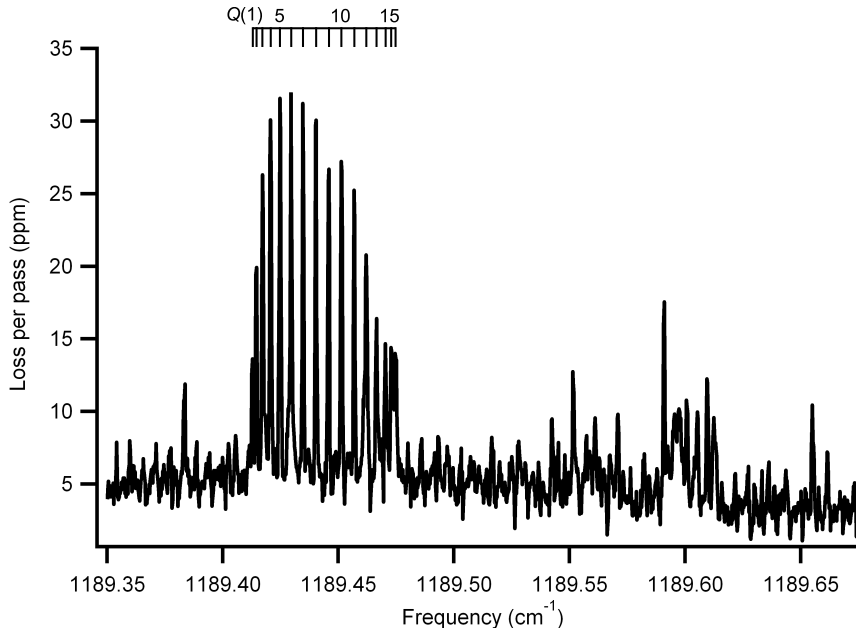


Figure 3.2:  $Q$ -branch of the  $\Pi(1_{01}, \nu_2 = 1) \leftarrow \Sigma(1_{01})$  band. The other lines present also appear in helium expansions and are not  $R$ -branch transitions, but are from  $(D_2O)_n$  clusters. This spectrum was observed with  $\sim 700$  torr Ar backing pressure to improve signal-to-noise.

$(D_2O)_n$  clusters. The absence of  $P$ - and  $R$ -branch lines indicates that no transitions occur from the  $\Sigma(1_{01})$  state to the  $\Pi^e(1_{01}, \nu_2 = 1)$  state, which is in contrast to Zwart and Meerts,[56] who observed  $P$ -,  $Q$ -, and  $R$ -branch transitions of this band in the far-infrared. The  $1_{01}, \nu_2 = 1 \leftarrow 1_{01}$  transition in  $D_2O$  monomer is forbidden, and only occurs in Ar- $D_2O$  because of mixing between the  $\Pi(1_{01})$  and  $\Pi(1_{10})$  states because of anisotropy in the potential energy surface of the complex.[56] It is unclear why only the  $\Pi^f(1_{01}, \nu_2 = 1)$  would mix with the  $\Pi(1_{10}, \nu_2 = 1)$  state, though the lack of  $P$ - and  $R$ -branch lines implies that this is the case. It is possible that the  $\Pi^e(1_{01}, \nu_2 = 1)$  state does not mix because of Coriolis interaction with the  $\Sigma^e(1_{01}, \nu_2 = 1)$  state.

We have fit the  $Q$ -branch transitions using the approach outlined above to obtain upper state constants, while keeping the constants for the  $\Sigma(1_{01})$  state fixed to the values from Ref. [56]. The results are presented in Table 3.3 and a list of the observed transitions is presented in Table 3.4.

### 3.3.3 Additional $\Pi \leftarrow \Sigma$ bands

In addition to these bands we have observed two bands with clear  $P$ -,  $Q$ -, and  $R$ -branch structure near 1191.3 and 1191.6  $\text{cm}^{-1}$ , as shown in Figure 3.3. Both bands have an  $R(0)$  transition and lack a  $P(1)$  transition, identifying them as  $\Pi \leftarrow \Sigma$  bands. These bands only appear at the relatively low backing pressures we

Table 3.3: Molecular constants (in  $\text{cm}^{-1}$ ) for the  $\Pi(1_{01}, \nu_2 = 1) \leftarrow \Sigma(1_{01})$  band and two newly observed  $\Pi \leftarrow \Sigma$  bands. Values in parentheses represent one standard deviation from the least squares fit to the data. The labeling of the band 1 and band 2 constants as  $e$  or  $f$  assumes that the lower  $\Sigma$  state is an  $e$  state.

Parameter	$\Pi(1_{01}, \nu_2 = 1) \leftarrow \Sigma(1_{01})$	$\Pi \leftarrow \Sigma$ band 1	$\Pi \leftarrow \Sigma$ band 2
$B''$	0.09103344(33) <sup>a</sup>	0.0925124(86)	0.092491(16)
$D''(\times 10^6)$	1.7666(80) <sup>a</sup>	-	-
$\nu$	1189.41215(11)	1191.584206(94)	1191.29042(18)
$B'(e)$	-	0.093026(13)	0.093050(15)
$D'(e)(\times 10^6)$	-	0.98(18) <sup>b</sup>	0.53(11) <sup>b</sup>
$B'(f)$	0.0914774(22)	0.0936565(87)	0.093601(17)
$D'(f)(\times 10^6)$	2.5568(85)	0.2924(32) <sup>b</sup>	0.273(24) <sup>b</sup>
$\sigma$	0.0002	0.0002	0.0003

a)From Ref. [56]. b)Reported values are actually  $\Delta D$  because  $D''$  was not included in the fit for these bands.

Table 3.4: Observed transitions for the  $\Pi(1_{01}, \nu_2 = 1) \leftarrow \Sigma(1_{01})$  band (in  $\text{cm}^{-1}$ ). Values in parentheses are residuals (observed - calculated) from the least squares fit.

Transition	Frequency
$Q(1)$	1189.4129(-2)
$Q(2)$	1189.4145(-3)
$Q(3)$	1189.4173(-1)
$Q(4)$	1189.4207(0)
$Q(5)$	1189.4249(1)
$Q(6)$	1189.4296(2)
$Q(7)$	1189.4348(2)
$Q(8)$	1189.4403(3)
$Q(9)$	1189.4459(2)
$Q(10)$	1189.4514(0)
$Q(11)$	1189.4569(-1)
$Q(12)$	1189.4621(-1)
$Q(13)$	1189.4665(-3)
$Q(14)$	1189.4704(-1)
$Q(15)$	1189.4730(-1)
$Q(16)$	1189.4748(3)

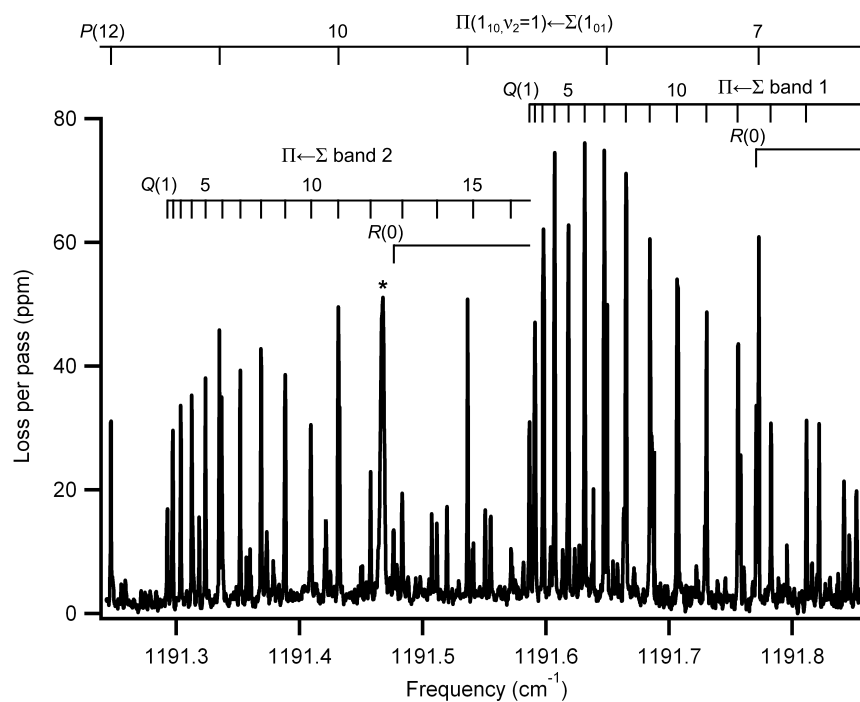


Figure 3.3:  $Q$ -branch region of two previously unobserved  $\Pi \leftarrow \Sigma$  transitions of Ar-D<sub>2</sub>O between 1191 and 1192 cm<sup>-1</sup>. The presence of  $R(0)$  lines for both bands provide evidence that both are  $\Pi \leftarrow \Sigma$  transitions.  $P$ -branch lines from the nearby  $\Pi(1_{10}, \nu_2 = 1) \leftarrow \Sigma(1_{01})$  can also be seen. The line marked with an asterisk(\*) is due to HOD. Additional lines present in the spectrum are due to the presence of (D<sub>2</sub>O)<sub>*n*</sub> clusters in the expansion. The spectrum was collected at a backing pressure of  $\sim 300$  torr.

used when collecting our spectra. As we increased the backing pressure of the supersonic expansion, the lines became progressively weaker until they disappeared altogether. As the backing pressure increases, the temperature of molecules in the expansion decreases, which suggests that these bands originate in excited internal rotor states in the ground vibrational state. As the temperature in the expansion decreases, these excited states will no longer be populated, leading to the decrease in signal. Because of this, it is not surprising that these bands were not observed by Li et al., because they used a backing pressure of  $\sim 4$  bar in their expansion, which likely cooled all of the Ar-D<sub>2</sub>O to the ground internal rotor states.

We have fit the two bands (which we refer to as band 1 for the stronger band at  $1191.6\text{ cm}^{-1}$  and band 2 for the weaker band at  $1191.3\text{ cm}^{-1}$ ) using the approach outlined above and the results of the fit are presented in Table 3.3. The observed transitions are listed in Table 3.5. We excluded  $D''$  from the fit for both bands because the uncertainty was larger than the constant when it was included. It is interesting to note that  $B''$  for the two bands are nearly identical, which could be an indication that these two bands originate in the same lower state.

These two bands do not correspond to any transitions observed by far-IR spectroscopy of Ar-D<sub>2</sub>O, and without further data it is difficult to definitively assign these bands. The observed bands could be due to transitions from low-lying internal rotor states of D<sub>2</sub>O. There are two transitions of D<sub>2</sub>O monomer that lie near this frequency range from low-lying rotational levels:  $2_{02}, \nu_2 = 1 \leftarrow 1_{11}$  at  $1194.40\text{ cm}^{-1}$  and  $2_{11}, \nu_2 = 1 \leftarrow 2_{02}$  at  $1193.26\text{ cm}^{-1}$ .<sup>[34]</sup> It is also possible that these bands both originate in the  $n = 1, \Sigma(0_{00})$  intermolecular stretching state of Ar-D<sub>2</sub>O.

To make a tentative assignment of these bands, we first consider the energies of the possible lower states compared to the ground  $\Sigma(0_{00})$  state of Ar-D<sub>2</sub>O. The  $\Sigma(1_{11})$  state has been measured by far-IR spectroscopy to lie  $20.7\text{ cm}^{-1}$  above the ground state,<sup>[55]</sup> while the  $\Sigma(2_{02})$  state is predicted to be  $\sim 32\text{ cm}^{-1}$  above the ground state according to the potential energy surface of Cohen and Saykally.<sup>[61]</sup> Cohen and Saykally also predicted that the intermolecular stretching state of Ar-D<sub>2</sub>O lies  $\sim 36\text{ cm}^{-1}$  above the ground  $\Sigma(0_{00})$  state. In a cold supersonic expansion, the lower-lying  $1_{11}$  and  $2_{02}$  states will be more populated than the intermolecular stretching state, making it more likely that we would observe transitions from these lower-lying states. In addition, the only transition from the intermolecular stretching state that might lie near this frequency region would be a red-shifted hot band transition of the  $\Pi(1_{11}, \nu_2 = 1) \leftarrow \Sigma(0_{00})$  band observed near  $1199\text{ cm}^{-1}$  (i.e.,  $\Pi(1_{11}, n = 1, \nu_2 = 1) \leftarrow \Sigma(0_{00}, n = 1)$ ).<sup>[3]</sup> If we had observed this band, we would also expect to observe the  $\Sigma \leftarrow \Sigma$  band instead of the two  $\Pi \leftarrow \Sigma$  bands we have seen. Based on these arguments, we tentatively assign band 1 as  $\Pi(2_{02}, \nu_2 = 1) \leftarrow \Sigma(1_{11})$  and band 2 as  $\Pi(2_{11}, \nu_2 = 1) \leftarrow \Sigma(2_{02})$ . The relative intensities of the bands support this assignment, as band 2 is weaker than band 1 and the  $2_{02}$

level lies higher in energy than the  $1_{11}$  level.

Table 3.5: Observed transitions for the two newly observed  $\Pi \leftarrow \Sigma$  bands (in  $\text{cm}^{-1}$ ). Values in parentheses are residuals (observed - calculated) from the least squares fit.

Transition	Band 1	Band 2
$P(6)$	1190.4887(1)	
$P(5)$	1190.6687(-3)	1190.3766(1)
$P(4)$	1190.8501(0)	1190.5576(5)
$P(3)$	1191.0325(4)	1190.7381(-7)
$P(2)$		1190.9210(-6)
$Q(1)$	1191.5867(2)	1191.2926(0)
$Q(2)$	1191.5911(0)	1191.2970(0)
$Q(3)$	1191.5980(1)	1191.3036(-1)
$Q(4)$	1191.6070(0)	1191.3125(0)
$Q(5)$	1191.6183(0)	1191.3236(2)
$Q(6)$	1191.6314(-3)	1191.3367(2)
$Q(7)$	1191.6473(0)	1191.3518(1)
$Q(8)$	1191.6650(0)	1191.3687(-2)
$Q(9)$	1191.6844(-4)	1191.3883(2)
$Q(10)$	1191.7065(0)	1191.4091(-1)
$Q(11)$	1191.7304(3)	1191.4316(-6)
$Q(12)$	1191.7560(4)	1191.4576(6)
$Q(13)$	1191.7827(0)	1191.4833(-2)
$Q(14)$	1191.8115(0)	1191.5115(0)
$Q(15)$	1191.8419(0)	
$Q(16)$	1191.8738(0)	
$Q(17)$	1191.9069(0)	
$Q(19)$	1191.9764(-3)	
$Q(20)$	1192.0134(2)	
$R(0)$	1191.7707(4)	1191.4763(-3)
$R(1)$	1191.9574(1)	1191.6632(-6)
$R(2)$	1192.1453(0)	1191.8520(0)
$R(3)$	1192.3341(-1)	1192.0413(-1)
$R(4)$	1192.5240(1)	1192.2315(-1)
$R(5)$	1192.7140(-1)	1192.4231(2)
$R(6)$	1192.9051(1)	1192.6150(0)
$R(7)$		1192.8079(1)
$R(8)$		1193.0012(-1)

### 3.4 Conclusion

We have observed three previously unobserved bands of Ar-D<sub>2</sub>O in the  $\nu_2$  bend region of D<sub>2</sub>O and provided additional data for the previously observed  $\Pi(1_{10}, \nu_2 = 1) \leftarrow \Sigma(1_{01})$  band. We have fit all four bands using a pseudo-diatomic model for Ar-D<sub>2</sub>O and obtained accurate excited-state molecular constants, as

well as ground state constants for two of the new bands. We assign the band at  $1189.4 \text{ cm}^{-1}$  as the  $\Pi(1_{01}, \nu_2 = 1) \leftarrow \Sigma(1_{01})$  band and tentatively identify two newly observed bands as  $\Pi(2_{02}, \nu_2 = 1) \leftarrow \Sigma(1_{11})$  and  $\Pi(2_{11}, \nu_2 = 1) \leftarrow \Sigma(2_{02})$ , which have not previously been observed by microwave, far-infrared, or infrared spectroscopy.

## Chapter 4

# Rotationally-resolved Infrared Spectroscopy of the Donor Bending Mode of Deuterated Water Dimer

### 4.1 Introduction

Water is a ubiquitous molecule with unique properties that make it essential for life as we know it. Many of these unique properties arise because of the complex hydrogen bonding interactions that occur among water molecules. Because of the central importance of water in many fields, especially chemistry and biology, a large amount of research effort has been expended to create an accurate model of water, particularly in the liquid phase.[2, 66, 67] In order to create an accurate model of water, it is essential to understand the detailed intermolecular interactions that occur between water molecules. To study these interactions in detail, there have been extensive experimental and theoretical studies of small, gas phase water clusters. The water dimer has been of particular interest because of the importance of two-body interactions in creating accurate models of liquid water.[68, 69]

Water dimer has been extensively studied by high-resolution spectroscopy throughout the microwave[70, 71, 72, 73, 74, 75, 76, 77], sub-millimeter[78, 79, 77], far-IR[80, 81, 82, 83, 84], and mid-IR[85, 86] regions of the spectrum, for both  $(\text{H}_2\text{O})_2$  and  $(\text{D}_2\text{O})_2$ . This work has elucidated the structure of the water dimer and the details of its complex energy level structure. This complexity arises from the fact that three major tunneling motions are present in the dimer, which causes each rotational energy level to be split into six different sublevels. The high-resolution spectroscopic work has yielded energy levels and tunneling splittings of the ground state and many of the excited intermolecular vibrational states of both  $(\text{H}_2\text{O})_2$  and  $(\text{D}_2\text{O})_2$ . These data have been used to develop empirical potentials for the water dimer,[69, 87, 88, 66] and more recently *ab initio* potentials have been calculated and compared with the experimental data.[89, 90, 91, 92, 93]

While the low-lying states of  $(\text{H}_2\text{O})_2$  and  $(\text{D}_2\text{O})_2$  have been comprehensively studied, much less work has been done on the intramolecular vibrational modes in the mid-IR, presumably because of the difficulty in obtaining light sources in this region that are suitable for high-resolution spectroscopy. High-resolution spectra of the intramolecular modes provide additional data to support theoretical work on the water dimer,

---

This chapter is a draft of a manuscript in preparation for submission to the Journal of Physical Chemistry A, authored by J. T. Stewart and B. J. McCall.

including vibrational frequency shifts and tunneling barriers in the excited vibrational states. Recent potentials have been developed which attempt to include the effect of intramolecular vibrations,[93] but only some of the intramolecular vibrations have been experimentally measured at high resolution. Huang and Miller[85] measured rotationally-resolved spectra of the O-H stretching bands of  $(\text{H}_2\text{O})_2$ , and the equivalent O-D stretching bands of  $(\text{D}_2\text{O})_2$  were later measured by Paul et al.[86] Low-resolution spectra of the bending modes of  $(\text{H}_2\text{O})_2$  have also been obtained,[4] but up to this point in time, no rotationally-resolved spectra of the bending modes of water dimer have been recorded.

In addition to the gas phase measurements of Paul et al., low-resolution spectra have been obtained for the bending modes of  $(\text{H}_2\text{O})_2$  and  $(\text{D}_2\text{O})_2$  in various matrices, including Ar,[94, 95] Kr,[96]  $\text{N}_2$ ,[97] Ne,[98] and *para*- $\text{H}_2$ .[99] All of these studies show that there are two distinct frequencies in the region of the bending mode of the water dimer, which correspond to the hydrogen bond donor and acceptor subunits of the complex. All of the work on these modes agrees that the bending mode of the hydrogen bond acceptor ((A) in Figure 4.1) lies lower in frequency than the bending mode of the hydrogen bond donor ((B) in Figure 4.1) by  $\sim 10 \text{ cm}^{-1}$ .

The recent development of quantum cascade lasers (QCLs) has enabled a variety of high-resolution spectroscopic studies throughout the mid-IR. In the present work, we have utilized a QCL operating near  $8.5 \mu\text{m}$  to record rotationally-resolved spectra of the bending modes of the hydrogen bond donor of  $(\text{D}_2\text{O})_2$ . We have observed two perpendicular bands of this vibrational mode, which we have used to calculate the band center of the donor bend. We have also estimated the acceptor switching tunneling splittings for the  $K_a = 1$  and 2 levels in the excited state of the donor bend.

## 4.2 Experimental

High-resolution spectra of the  $(\text{D}_2\text{O})_2$  bending modes were acquired using our QCL based infrared spectrometer, which has been described in detail previously.[16, 17] We will give a brief description of the instrument here, highlighting details pertinent to the present study. Infrared light is generated using a QCL which can be tuned from  $\sim 1180\text{--}1200 \text{ cm}^{-1}$  by varying the temperature and current of the laser. Light from the laser is sent to a high-finesse cavity where we perform cw cavity ringdown spectroscopy (cw-CRDS) to obtain a sensitive absorption spectrum of  $\text{D}_2\text{O}$  clusters which are generated in a continuous supersonic expansion. The frequency of our laser is calibrated using a combination of a mid-IR wavemeter (Bristol) and a  $\text{SO}_2$  absorption cell, using lines contained in the HITRAN database.[63] By calibrating our laser frequency with these sources, we estimate that our absolute frequency accuracy is  $\sim 0.0005 \text{ cm}^{-1}$  (15 MHz).

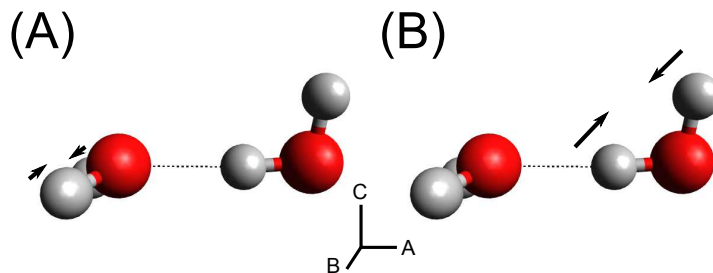


Figure 4.1: Representation of the two intramolecular bending modes of  $(\text{D}_2\text{O})_2$ , corresponding to bending of (A) the hydrogen bond acceptor and (B) the hydrogen bond donor. The principal axes are also indicated in the figure.

To generate  $(\text{D}_2\text{O})_2$ , we bubble either argon or helium gas through a room temperature  $\text{D}_2\text{O}$  (Cambridge Isotope Laboratories, 99.9 % D) reservoir. The gas mixture is then sent through a  $150 \mu\text{m} \times 1.2 \text{ cm}$  slit into a vacuum chamber which is pumped by a Roots blower and rotary vane pump (Oerlikon-Leybold). For most data presented in this paper, we used a mass flow controller (MKS Instruments) after the  $\text{D}_2\text{O}$  reservoir to provide a consistent gas flow to the slit, though some spectra were obtained without the mass flow controller. Expansions were run at backing pressures of  $\sim 300\text{--}400$  Torr for argon expansions and  $\sim 850\text{--}950$  Torr for helium expansions, as measured by a pressure gauge attached to the input line into the vacuum chamber.

For the helium expansions, a consistent decrease in the baseline was observed over the course of scanning the laser. The decrease roughly corresponded with the amount of  $\text{D}_2\text{O}$  remaining in the bubbler. A similar baseline drift was sometimes seen when measuring the argon expansions, though it was generally a smaller effect. The linewidth (FWHM) of individual transitions in argon expansions is  $\sim 15\text{--}20$  MHz; in helium expansions the lines are slightly broader, with a linewidth of  $\sim 35\text{--}40$  MHz. In both the argon and helium spectra, strong  $\text{D}_2\text{O}$  and HOD monomer lines are present throughout the acquired data, and have been removed for clarity. In the argon expansions, strong bands of  $\text{Ar-D}_2\text{O}$  were observed in addition to the  $\text{D}_2\text{O}$ -only cluster lines presented in this work. Our analysis of the  $\text{Ar-D}_2\text{O}$  bands has been published previously[100], and a prior analysis of the strongest bands in this region is also available.[3] The lines from these bands have also been removed from the presented data for clarity.

### 4.3 Energy level structure of water dimer

The spectrum of the intramolecular bending modes of  $(\text{D}_2\text{O})_2$  is complicated by the fact that water dimer has two distinct intramolecular bending modes, corresponding to bending of the hydrogen bond acceptor and donor subunits of the complex. These vibrations, as well as the principal axes of the complex, are shown in Figure 4.1. As stated above, previous experimental and theoretical studies of  $(\text{D}_2\text{O})_2$  have found that the

donor bend ((B) in Figure 4.1) lies  $\sim 10 \text{ cm}^{-1}$  higher in energy than the acceptor bend ((A) in Figure 4.1).

The observed spectrum is further complicated by the complex tunneling motions which occur in water dimer. There are three major tunneling motions which occur in the complex. The lowest barrier tunneling motion is an interchange of the hydrogen atoms of the acceptor subunit, which is called “acceptor switching” and causes splitting of individual rotational energy levels into two sublevels. The second tunneling motion is an interchange of the acceptor and donor subunits (referred to as “interchange tunneling”) and splits each of the two sublevels from the acceptor switching into four levels, with two of the states being degenerate. The final tunneling motion is an interchange of the hydrogen atoms of the donor subunit (referred to as “bifurcation tunneling”), which causes a small shift of the degenerate E levels relative to the A and B levels. The overall energy level structure for an individual rotational level is shown in Figure 4.2 for the  $K_a = 0$ ,  $J = 0$  level of the ground vibrational state of  $(\text{D}_2\text{O})_2$ . For levels with  $K_a \geq 1$ , each rotation-tunneling level is further split into two by asymmetry splitting.

A group theoretical description of water dimer was presented by Dyke[101] and gives the statistical weights and selection rules for the rotation-tunneling levels. The tunneling levels can be identified with their symmetry labels in the permutation inversion group for water dimer, which is isomorphic with the  $D_{4h}$  point group, as shown in Figure 4.2. The spin statistical weights for the rotational-tunneling levels of  $(\text{D}_2\text{O})_2$  are  $A_1^\pm$  (21),  $B_1^\pm$  (15),  $A_2^\pm$  (3),  $B_2^\pm$  (6), and  $E^\pm$  (18). The selection rules for transitions between these levels are  $A_1^+ \leftrightarrow A_1^-$ ,  $B_1^+ \leftrightarrow B_1^-$ ,  $A_2^+ \leftrightarrow A_2^-$ ,  $B_2^+ \leftrightarrow B_2^-$ , and  $E^+ \leftrightarrow E^-$ .

## 4.4 Results

The supersonic expansion that we use to produce  $(\text{D}_2\text{O})_2$  also produces a variety of other species, such as larger water clusters and clusters containing  $\text{D}_2\text{O}$  in combination with the carrier gas. To determine which absorption features arise from water-only clusters (i.e.,  $(\text{D}_2\text{O})_n$ ), we used both Ar and He as the carrier gas for the expansion. The absorption features we report here were present in expansions with both carrier gases, confirming that they are due to  $(\text{D}_2\text{O})_n$  clusters. After finding the lines from water-only clusters, we have followed the approach of Cruzan et al.[102] to determine the number of  $\text{D}_2\text{O}$  units in the cluster. This is done by recording absorption spectra of the expansion using several different mixtures of  $\text{D}_2\text{O}$  and  $\text{H}_2\text{O}$ . We assume that the H and D atoms in the liquid mixture rapidly equilibrate to produce a statistical mixture of  $\text{D}_2\text{O}$ ,  $\text{H}_2\text{O}$ , and HOD. If we neglect any kinetic isotope effects for this rearrangement, we can generate

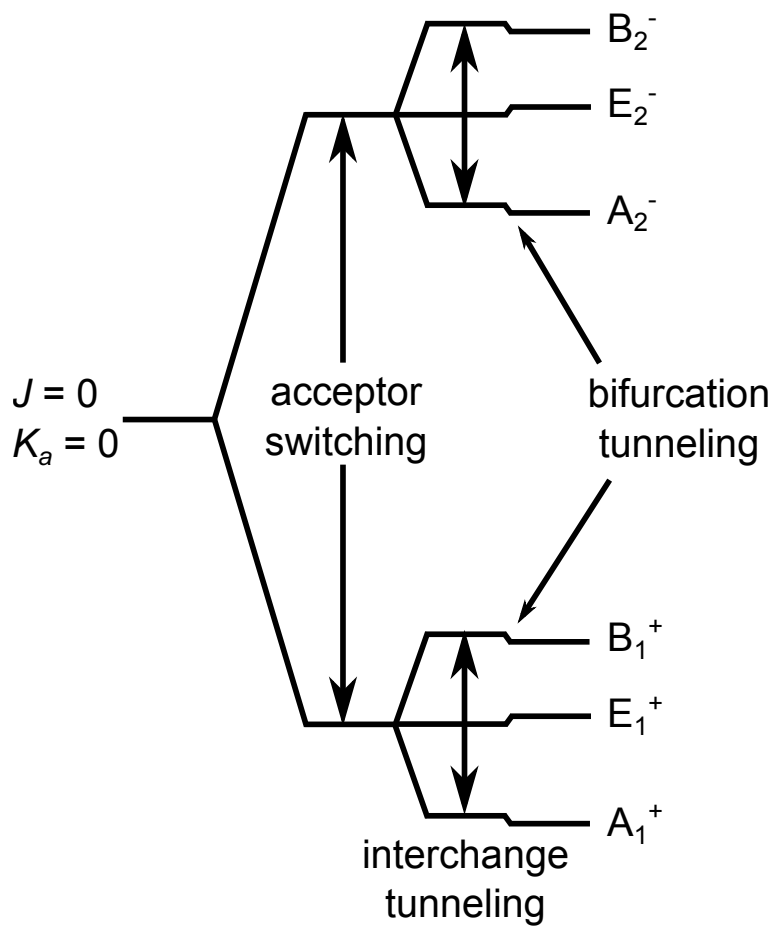


Figure 4.2: Energy levels of the tunneling sublevels of the  $K_a = 0$ ,  $J = 0$  rotational level of the ground state of  $(D_2O)_2$ . The effects of the three tunneling motions present in water dimer (acceptor switching, interchange tunneling, and bifurcation tunneling) are indicated in the figure. The symmetry labels of the resulting rotation-tunneling states are also included.

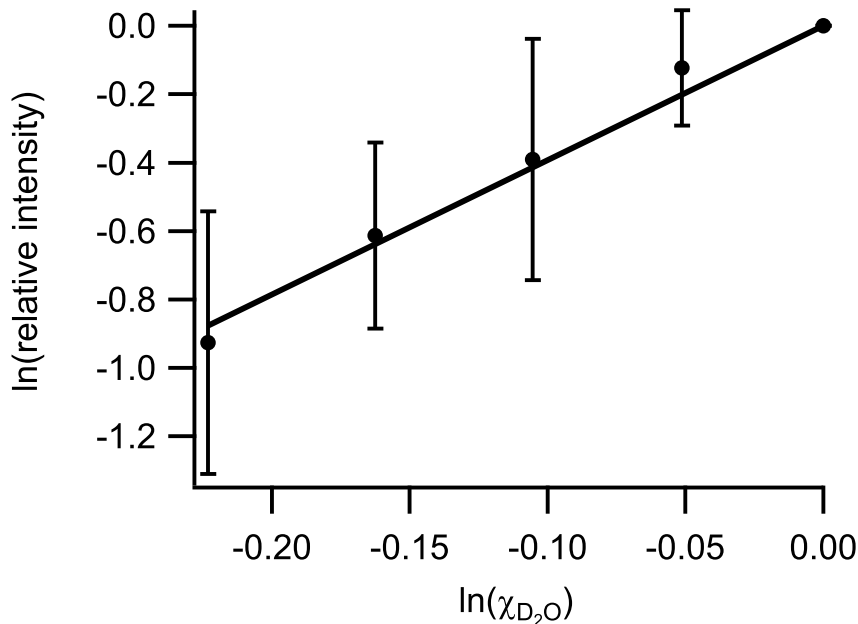


Figure 4.3: Plot of  $\ln(\text{relative intensity})$  versus  $\ln(\chi_{D_2O})$  for several  $D_2O/H_2O$  mixtures to determine the cluster size responsible for absorption features recorded near  $1195.55 \text{ cm}^{-1}$ . Multiple measurements of the absorption intensity were made for pure  $D_2O$  and mixtures of 95%, 90%, 85%, and 80%  $D_2O$  diluted with  $H_2O$ . The intercept of the linear fit was fixed to 0, and the resulting slope is  $3.93 \pm 0.33$ , indicating a cluster size of 2. The error bars and uncertainty indicate a 95% confidence level.

the following relationship to determine the cluster size:

$$\ln\left(\frac{I}{I_0}\right) = 2n \ln(\chi_{D_2O}) \quad (4.1)$$

In this equation,  $I$  is the intensity of an absorption feature for an expansion using a  $D_2O/H_2O$  mixture,  $I_0$  is the intensity of the feature for an expansion of pure  $D_2O$ ,  $n$  is the cluster size (i.e.,  $n = 2$  for water dimer), and  $\chi_{D_2O}$  is the mole fraction of  $D_2O$  in the mixture. By recording absorption spectra with a range of values for  $\chi_{D_2O}$ , we can plot  $\ln(I/I_0)$  versus  $\ln(\chi_{D_2O})$  to find the slope of the line, which gives the cluster size. Figure 4.3 shows such a plot for absorption features we recorded near  $1195.55 \text{ cm}^{-1}$ , which belong to the Q-branch of the  $K_a = 2 \leftarrow 1$  sub-band of the donor bending mode. The slope of the line in Figure 4.3 is  $3.93 \pm 0.33$ , which agrees with the expected value of 4 for  $(D_2O)_2$ .

We have observed two main bands of  $(D_2O)_2$  near  $1187$  and  $1195 \text{ cm}^{-1}$ , which we assign as the  $K_a = 1 \leftarrow 0$  and  $K_a = 2 \leftarrow 1$  sub-bands of the bending mode of the hydrogen bond donor. We assign these bands to the donor bend because, as noted above, previous experimental and theoretical work has shown that the donor bend lies  $\sim 10 \text{ cm}^{-1}$  higher in frequency than the acceptor bend. We have obtained spectra of Ar

expansions up to  $\sim 1204 \text{ cm}^{-1}$  and have not seen any strong absorption features beyond  $1200 \text{ cm}^{-1}$ . There are some weak absorption features near  $1203 \text{ cm}^{-1}$ , but these are most likely from the  $K_a = 3 \leftarrow 2$  sub-band. In contrast, spectra of both Ar and He expansions recorded down to  $\sim 1182 \text{ cm}^{-1}$  show strong absorption features throughout the frequency region to the red of these two main bands in both carrier gases. While we have not yet been able to definitively assign these absorption features, they may be due to the acceptor bend, meaning the higher frequency features we present here must arise from the donor bend.

Based on the energy level structure of  $(\text{D}_2\text{O})_2$  outlined in Section 4.3, we expect that there will be six separate tunneling sub-bands for each of the  $K_a = 1 \leftarrow 0$  and  $K_a = 2 \leftarrow 1$  sub-bands of  $(\text{D}_2\text{O})_2$ . These six bands will be split into two groups of three by the acceptor switching tunneling motion of the complex, resulting in two main groups of tunneling levels. These two groups are the tunneling levels with  $A_1^+$ ,  $E_1^+$ , and  $B_1^+$  symmetry (the lower three levels in Figure 4.2) and the levels with  $A_2^-$ ,  $E_2^-$ , and  $B_2^-$  symmetry (the upper three levels in Figure 4.2). The acceptor switching tunneling splitting has not been directly measured, but it has been estimated to range from  $\sim 1.2$  to  $1.8 \text{ cm}^{-1}$  from microwave[76] and infrared[86] studies of  $(\text{D}_2\text{O})_2$ . The magnitude of this splitting will lead to a clear separation of the two groups of tunneling levels in the spectrum. The three levels in each group will then be separated by the interchange tunneling splitting, which has been directly measured to be  $1172 \text{ MHz}$  ( $0.039 \text{ cm}^{-1}$ ) for the splitting between the  $A_1^+$  and  $B_1^+$  levels, and  $1083 \text{ MHz}$  ( $0.036 \text{ cm}^{-1}$ ) for the splitting between the  $A_2^-$  and  $B_2^-$  levels in the ground state for  $K_a = 0$ . [75] Because the interchange tunneling splitting is only  $\sim 0.04 \text{ cm}^{-1}$ , the three sub-bands corresponding to the tunneling levels are closely spaced, leading to substantial overlap of the Q-branches of the tunneling sub-bands. For the  $K_a = 2 \leftarrow 1$  sub-band, the spectrum is further complicated by asymmetry splitting in the  $K_a = 1$  level in the ground state. [78]

Our observed spectra for the  $K_a = 1 \leftarrow 0$  band in an Ar expansion are presented in Figure 4.4. Our frequency coverage of this region with a He expansion is limited to the Q-branch region and the R(0) lines because there was a gap in the frequency coverage of our QCL when the He spectra were recorded. Spectra of both Ar and He expansions are available further to the red from what is shown in Figure 4.4. As can be seen in the figure, there is a dense cluster of absorption lines near  $1187.4 \text{ cm}^{-1}$ , which arises from the series of overlapping Q-branches from multiple tunneling states. Because these Q-branches are much stronger than anything else nearby in the spectrum, we attribute them to the  $A_1^+/E_1^+/B_1^+$  tunneling levels, because these levels carry a larger statistical weight than the  $A_2^-/E_2^-/B_2^-$  tunneling levels. Clusters of R-branch transitions are also observed and labeled in the figure, which are spaced at  $\sim 0.36 \text{ cm}^{-1}$ . The  $0.36 \text{ cm}^{-1}$  spacing is approximately equal to 2 times the known  $B$  rotational constant for  $(\text{D}_2\text{O})_2$  ( $B = 0.1812 \text{ cm}^{-1}$  in the ground state), supporting the assignment of these absorption lines to  $(\text{D}_2\text{O})_2$ . R(0) transitions are

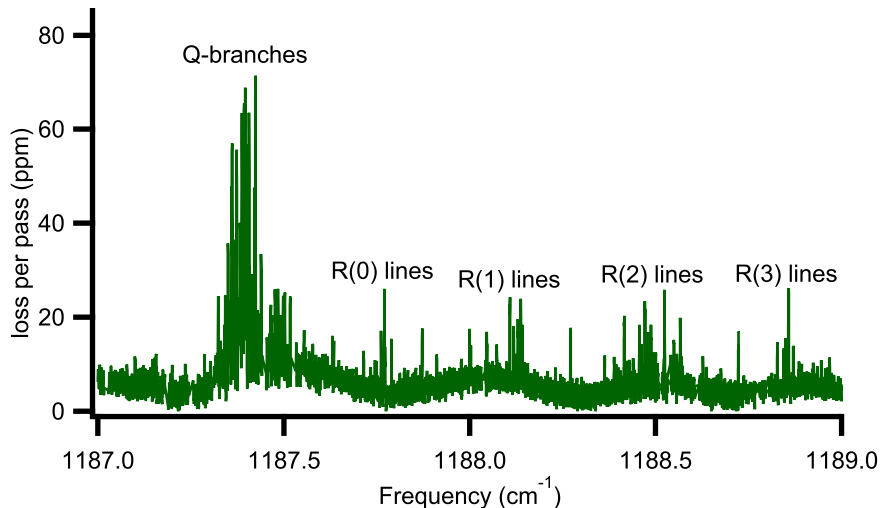


Figure 4.4: Observed spectrum of the  $K_a = 1 \leftarrow 0$  sub-band of the bending mode of hydrogen bond donor measured in an Ar supersonic expansion. The densely packed region of Q-branches and the R-branch lines are labeled in the figure. Because not all spectra were acquired with the same background level due to changes in alignment of the ringdown cavity over time, the spectra were brought to the same level by subtracting the minimum point in a scan from the entire scan. The apparent gap in the Q-branches is due to a strong absorption from  $D_2O$  monomer which has been removed from the spectrum for clarity.

observed, which aids in identifying the sub-band as  $K_a = 1 \leftarrow 0$ . Only a few possible P-branch transitions were observed, presumably because they were too weak to be observed due to the reduction in P-branch intensities for  $\Delta K_a = +1$  bands.[103] A similar effect was observed in measurements of the hydrogen bond acceptor antisymmetric stretch of  $(D_2O)_2$ . [86]

The  $K_a = 2 \leftarrow 1$  band of  $(D_2O)_2$  which we have observed lies near  $1195.5 \text{ cm}^{-1}$  and is shown in Figures 4.5 and 4.6 for Ar and He expansions, respectively. As can be seen in the figure, there is again a densely packed region caused by overlapping Q-branches of multiple tunneling components, with groups of R-branch lines spaced at  $\sim 0.36 \text{ cm}^{-1}$ . Because of the strength of the band, we attribute this band to the  $A_1^+/E_1^+/B_1^+$  tunneling levels. For this band, no R(0) transitions are observed, indicating that this band is  $K_a = 2 \leftarrow 1$ . Again, the P-branch transitions are expected to be weaker in this  $\Delta K_a = +1$  band, and are not observed in either Ar or He expansions.

The identification of these two bands as  $K_a = 1 \leftarrow 0$  and  $K_a = 2 \leftarrow 1$  bands is further confirmed by their frequency separation. For a near-prolate top such as  $(D_2O)_2$ , the Q-branches of adjacent sub-bands will be separated by  $\sim 2(A' - B')$ . [103] Though  $A'$  and  $B'$  are unknown for this band, we can assume that they will be close to their ground state values. Using the ground state values [104] of  $4.17 \text{ cm}^{-1}$  for  $A$  and  $0.181 \text{ cm}^{-1}$  for  $B$ , the expected separation between the Q-branches should be  $\sim 8 \text{ cm}^{-1}$ . If we take the center of the Q-branch regions as a rough approximation of the band center for the sub-bands we have observed, we

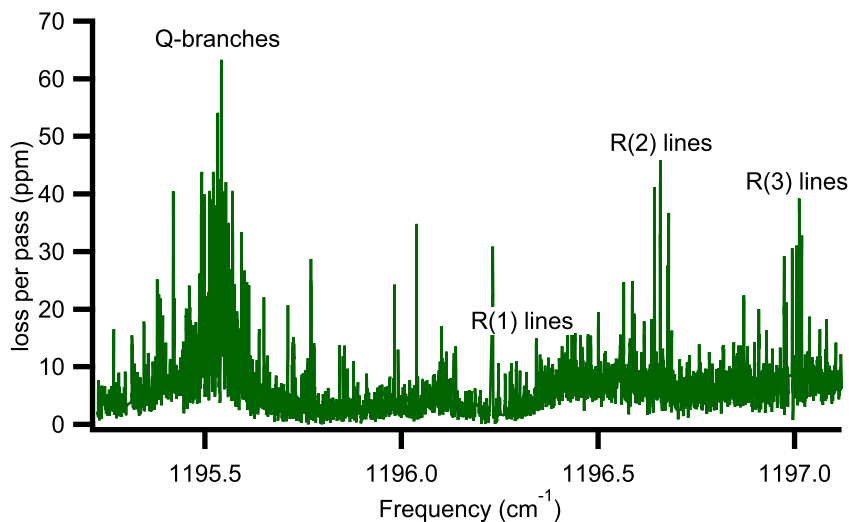


Figure 4.5: Observed spectrum of the  $K_a = 2 \leftarrow 1$  sub-band of the bending mode of hydrogen bond donor measured in an Ar supersonic expansion. The densely packed region of Q-branches and the R-branch lines are labeled in the figure. Because not all spectra were acquired with the same background level due to changes in alignment of the ringdown cavity over time, the spectra were brought to the same level by subtracting the minimum point in a scan from the entire scan.

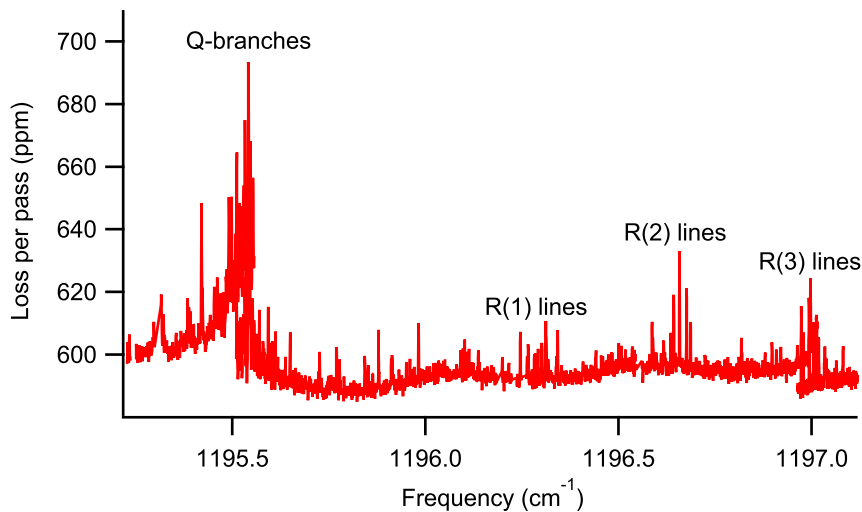


Figure 4.6: Observed spectrum of the  $K_a = 2 \leftarrow 1$  sub-band of the bending mode of hydrogen bond donor measured in a He supersonic expansion. The densely packed region of Q-branches and the R-branch lines are labeled in the figure.

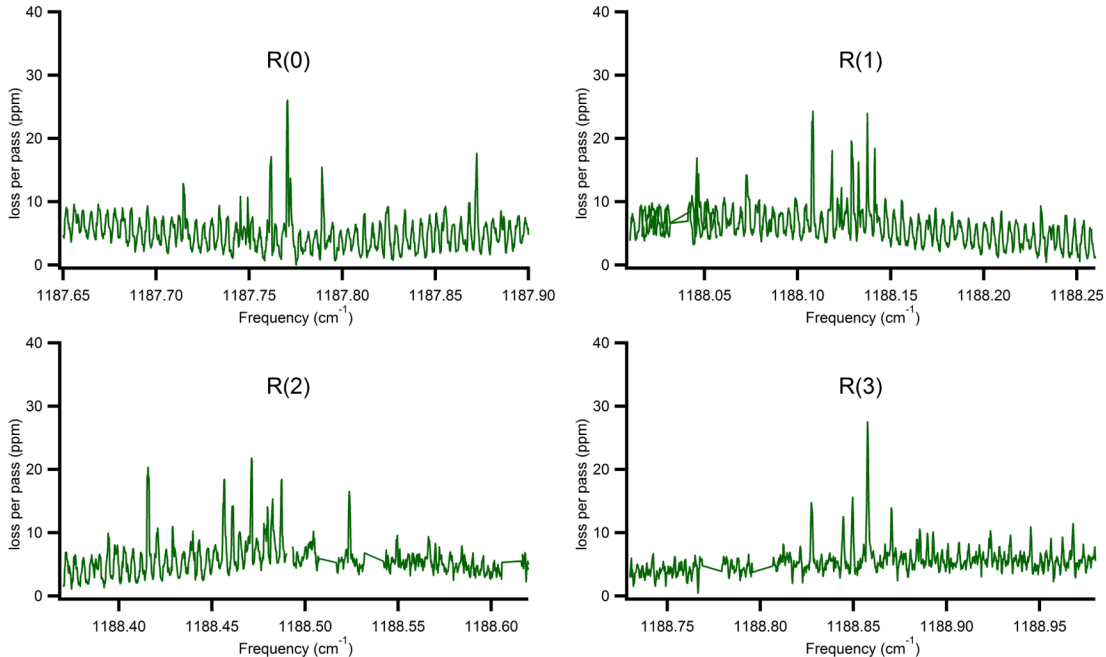


Figure 4.7: Zoomed-in views of the groups of R-branch lines of the  $K_a = 1 \leftarrow 0$  band measured in an Ar expansion. Each panel is offset  $0.36 \text{ cm}^{-1}$  from the previous panel, and all panels are  $0.25 \text{ cm}^{-1}$  wide. The gaps that are present are due to removal of monomer transitions.

estimate a separation of  $\sim 8.1 \text{ cm}^{-1}$ , which agrees well with the expected separation based on the ground state constants.

We have attempted to assign the spectra using a near-prolate top energy level expression, as has been done previously for water dimer, but were unable to obtain an unambiguous assignment. The many overlapping peaks in the Q-branch regions have made it difficult to use Q-branch transitions in making assignments, so our attempts have focused on the R-branch transitions (and the P-branch transitions we observed for the  $K_a = 1 \leftarrow 0$  band). Though the groups of peaks appear at a regular  $0.36 \text{ cm}^{-1}$  interval, there does not appear to be the expected triplet pattern for the  $A_1^+/E_1^+/B_1^+$  tunneling levels. This is illustrated in Figure 4.7, which shows close-up views of the R-branch lines we have observed for the  $K_a = 1 \leftarrow 0$  band. Only the R(0) lines show a possible triplet pattern which is seen in both Ar and He expansions. For the transitions with  $J'' > 1$ , more than three lines are observed, which is unexpected for the  $K_a = 1 \leftarrow 0$  band, as there should not be any asymmetry doubling, as in the  $K_a = 2 \leftarrow 1$  band. Unfortunately, we were not able to obtain data using a He expansion in this frequency region, so it is possible some of the extra lines could be attributed to some form of Ar-D<sub>2</sub>O cluster.

For the  $K_a = 2 \leftarrow 1$  band, we have data for both Ar and He expansions, which are shown in Figures 4.8 and 4.9, respectively. For this sub-band, we again expect a triplet pattern for the three tunneling levels, but

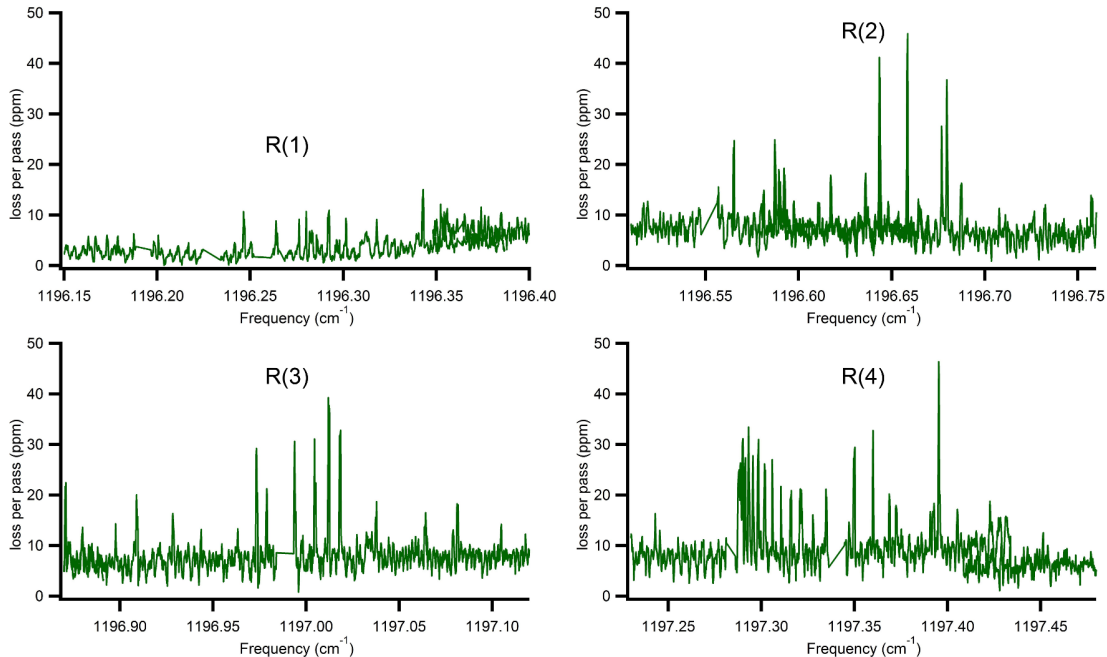


Figure 4.8: Zoomed-in views of the groups of R-branch lines  $K_a = 2 \leftarrow 1$  band measured in an Ar expansion. Each panel is offset  $0.36 \text{ cm}^{-1}$  from the previous panel, and all panels are  $0.25 \text{ cm}^{-1}$  wide. The gaps that are present are due to removal of monomer and Ar-D<sub>2</sub>O transitions. The group of lines near  $1197.28 \text{ cm}^{-1}$  are likely due to an unassigned band of Ar-D<sub>2</sub>O.

each of the components of the triplet will be composed of two lines separated by asymmetry splitting, which should be the same for all tunneling levels.[78] The groups of lines in Figures 4.8 and 4.9 do not show this pattern, which again has made it difficult to obtain a detailed assignment and fit of the tunneling levels. It is unclear what is causing the irregular patterns in the R-branch lines for both the  $K_a = 1 \leftarrow 0$  and  $K_a = 2 \leftarrow 1$  bands we have observed, though it must arise from the excitation of the bending vibration in the donor subunit. The interchange tunneling which leads to the expected triplet pattern in the bands involves the exchange of the donor and acceptor subunits, and must be affected by excitation of the donor subunit. A previous study[85] of the (H<sub>2</sub>O)<sub>2</sub> stretching modes observed a large decrease in the frequency of the interchange tunneling when the acceptor antisymmetric stretch was excited, which was attributed to a breakdown in the Born-Oppenheimer approximation separating the high-frequency and low-frequency vibrations.[105] A similar effect may be occurring with the bending mode, though it does not explain the extra lines we have observed in the  $K_a = 1 \leftarrow 0$  band.

In addition to the strong bands reported above, we have also seen features which we assign as bands arising from the  $A_2^-$ ,  $E_2^-$ , and  $B_2^-$  tunneling levels for both the  $K_a = 1 \leftarrow 0$  and  $K_a = 2 \leftarrow 1$  bands. Because the statistical weights of these levels are much lower than the  $A_1^+/E_1^+/B_1^+$  levels (with the exception of the  $E_2^-$  level) the absorption bands are much weaker. We have only been able to observe the Q-branches of these

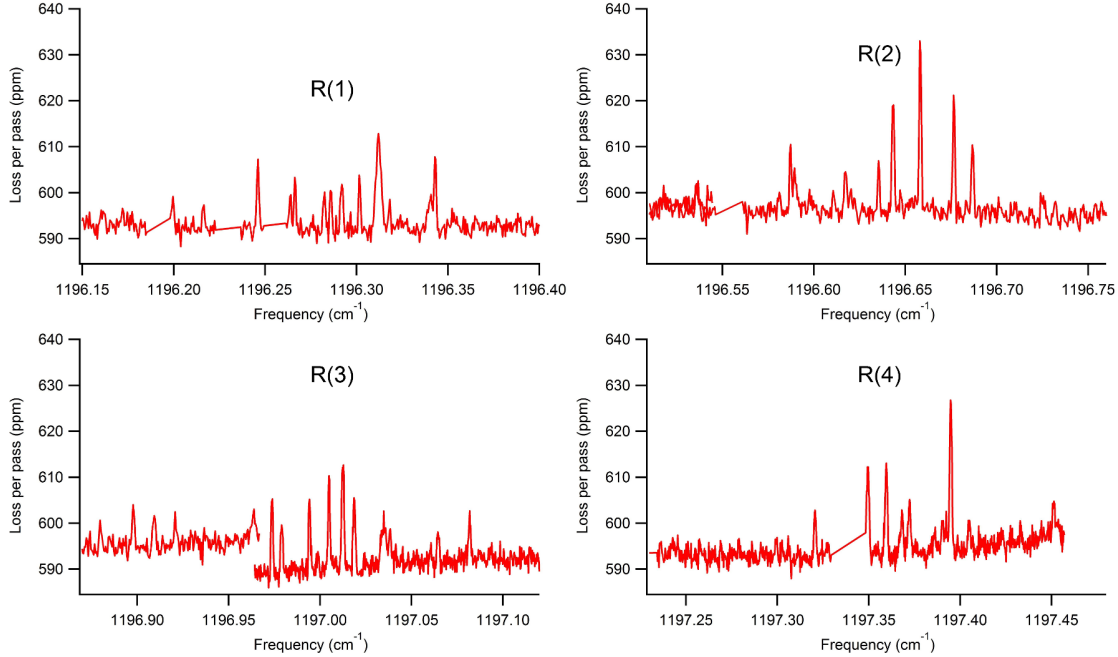


Figure 4.9: Zoomed-in views of the groups of R-branch lines  $K_a = 2 \leftarrow 1$  band measured in a He expansion. Each panel is offset  $0.36 \text{ cm}^{-1}$  from the previous panel, and all panels are  $0.25 \text{ cm}^{-1}$  wide. The gaps that are present are due to removal of monomer transitions.

Table 4.1: Approximate center frequency positions of the  $K_a = 1 \leftarrow 0$  and  $K_a = 2 \leftarrow 1$  sub-bands of the donor bend of  $(\text{D}_2\text{O})_2$ . The frequency positions listed are approximate values based on the center of the cluster of Q-branches observed for each band.

Band	Frequency ( $\text{cm}^{-1}$ )
$K_a = 1 \leftarrow 0$ ( $A_1^+/E_1^+/B_1^+$ levels)	1187.39
$K_a = 1 \leftarrow 0$ ( $A_2^-/E_2^-/B_2^-$ levels)	1184.97
$K_a = 2 \leftarrow 1$ ( $A_1^+/E_1^+/B_1^+$ levels)	1195.54
$K_a = 2 \leftarrow 1$ ( $A_2^-/E_2^-/B_2^-$ levels)	1194.68

levels, which are shown in Figures 4.10 and 4.11 for the  $K_a = 1 \leftarrow 0$  and  $K_a = 2 \leftarrow 1$  bands, respectively, alongside the stronger Q-branches of the  $A_1^+/E_1^+/B_1^+$  levels. Though the figures show only the spectra from Ar expansions, the features are also observed in He expansions. Because the bands are much weaker, we have not been able to identify R-branch transitions associated with the observed Q-branches. For the  $K_a = 1 \leftarrow 0$  band, the separation between these Q-branches is  $\sim 2.4 \text{ cm}^{-1}$ , and for the  $K_a = 2 \leftarrow 1$  band, the separation is  $\sim 0.9 \text{ cm}^{-1}$ . A summary of the frequency positions of the bands we have reported is presented in Table 4.1.

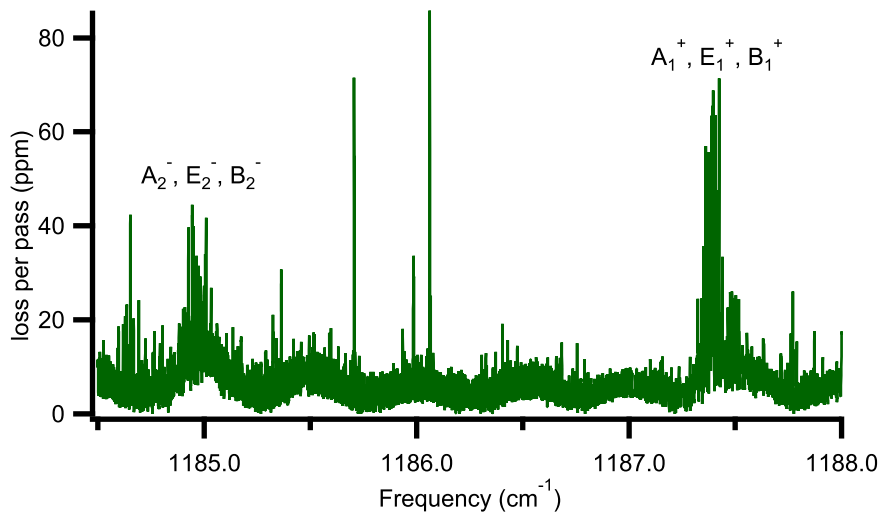


Figure 4.10: Q-branches of the  $K_a = 1 \leftarrow 0$  band for both the  $A_1^+/E_1^+/B_1^+$  tunneling levels and the  $A_2^-/E_2^-/B_2^-$  tunneling levels as observed in an Ar expansion. The two sets of levels are separated by  $\sim 2.4 \text{ cm}^{-1}$ .

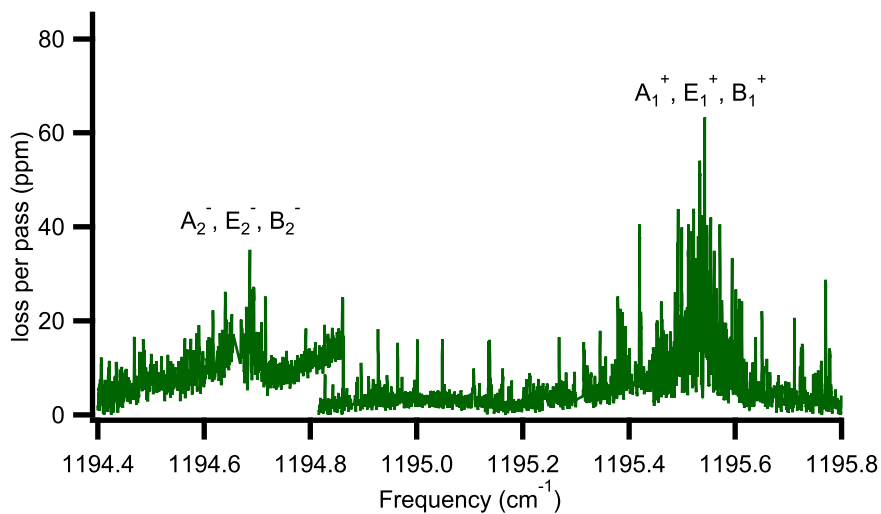


Figure 4.11: Q-branches of the  $K_a = 2 \leftarrow 1$  band for both the  $A_1^+/E_1^+/B_1^+$  tunneling levels and the  $A_2^-/E_2^-/B_2^-$  tunneling levels as observed in an Ar expansion. The two sets of levels are separated by  $\sim 1.3 \text{ cm}^{-1}$ .

## 4.5 Discussion

From the spectra and assignments presented above, we can calculate the gas-phase frequency of the donor bend and compare it to previous experiments and theoretical predictions. As noted above, the spacing between Q-branches of adjacent sub-bands of a near-prolate top are separated by  $\sim 2(A' - B')$ , which is  $\sim 8 \text{ cm}^{-1}$  for  $(\text{D}_2\text{O})_2$ . The band center for the vibrational band lies midway between the  $K_a = 1 \leftarrow 0$  and  $K_a = 0 \leftarrow 1$  sub-bands, so the band center is  $\sim 4 \text{ cm}^{-1}$  to the red of the  $K_a = 1 \leftarrow 0$  band. To attempt to estimate the band center without the influence of the acceptor switching tunneling, we can average the positions of the  $A_1^+/E_1^+/B_1^+$  and  $A_2^-/E_2^-/B_2^-$  tunneling components of the  $K_a = 1 \leftarrow 0$  band before calculating the band center. Doing so gives an estimated band center of  $1182.2 \text{ cm}^{-1}$ . This value is compared to previous experiments and calculations in Table 4.2. As shown in the table, the MULTIMODE calculations of Wang et al.[90] on an *ab initio* potential energy surface[89] produce a value in very good agreement with the gas phase spectra recorded here. Previous studies in various matrices consistently measured values which are higher in frequency than the gas phase value reported here. This is the opposite effect of what is seen with the  $(\text{D}_2\text{O})_2$  stretching modes, where the matrix values are consistently lower in frequency than the gas phase values measured by cavity ringdown spectroscopy.[90] The magnitude of the matrix shift is also greater by about a factor of 2 for the stretches as compared to the bending modes considered here. The difference between the gas phase and matrix data is likely due to a combination of perturbations from the matrix on  $(\text{D}_2\text{O})_2$  and the lack of rotational resolution making it difficult to assign the true band center. The DFT calculations performed by Ceponkus et al.[99] in connection with their *para*- $\text{H}_2$  matrix work produced a value significantly lower in frequency than the gas phase value we report.

The separation between the  $A_1^+/E_1^+/B_1^+$  and  $A_2^-/E_2^-/B_2^-$  tunneling levels provides information regarding the acceptor switching tunneling splitting in the excited state of the donor bend. Because the donor bend is symmetric under the  $C_s$  point group of  $(\text{D}_2\text{O})_2$ , the ordering of the  $A_1^+/E_1^+/B_1^+$  and  $A_2^-/E_2^-/B_2^-$  tunneling levels is expected to stay the same in the vibrationally excited state[101], instead of being reversed, as in the case of the acceptor antisymmetric stretch.[85, 86] The energy levels are depicted in Figure 4.12, with arrows indicating the bands observed in the current study. As can be seen in the figure, the  $2.4 \text{ cm}^{-1}$  separation between the  $A_1^+/E_1^+/B_1^+$  and  $A_2^-/E_2^-/B_2^-$  tunneling levels in the  $K_a = 1 \leftarrow 0$  band provides the sum of the acceptor switching tunneling splittings for the ground state  $K_a = 0$  level and the excited state  $K_a = 1$  level. If we assume a value of  $53 \text{ GHz}$  ( $\sim 1.8 \text{ cm}^{-1}$ ) for this splitting in the ground state  $K_a = 0$  level, as estimated by Paul et al.[86], we calculate the excited state splitting for the  $K_a = 1$  level to be  $\sim 0.6 \text{ cm}^{-1}$ , or  $19 \text{ GHz}$ . This is quite similar to the value of  $17 \text{ GHz}$  estimated by Paul et al. for the splitting in the ground state for  $K_a = 1$ . For the  $K_a = 2 \leftarrow 1$  band, the  $0.9 \text{ cm}^{-1}$  separation between the  $A_1^+/E_1^+/B_1^+$  and  $A_2^-/E_2^-/B_2^-$

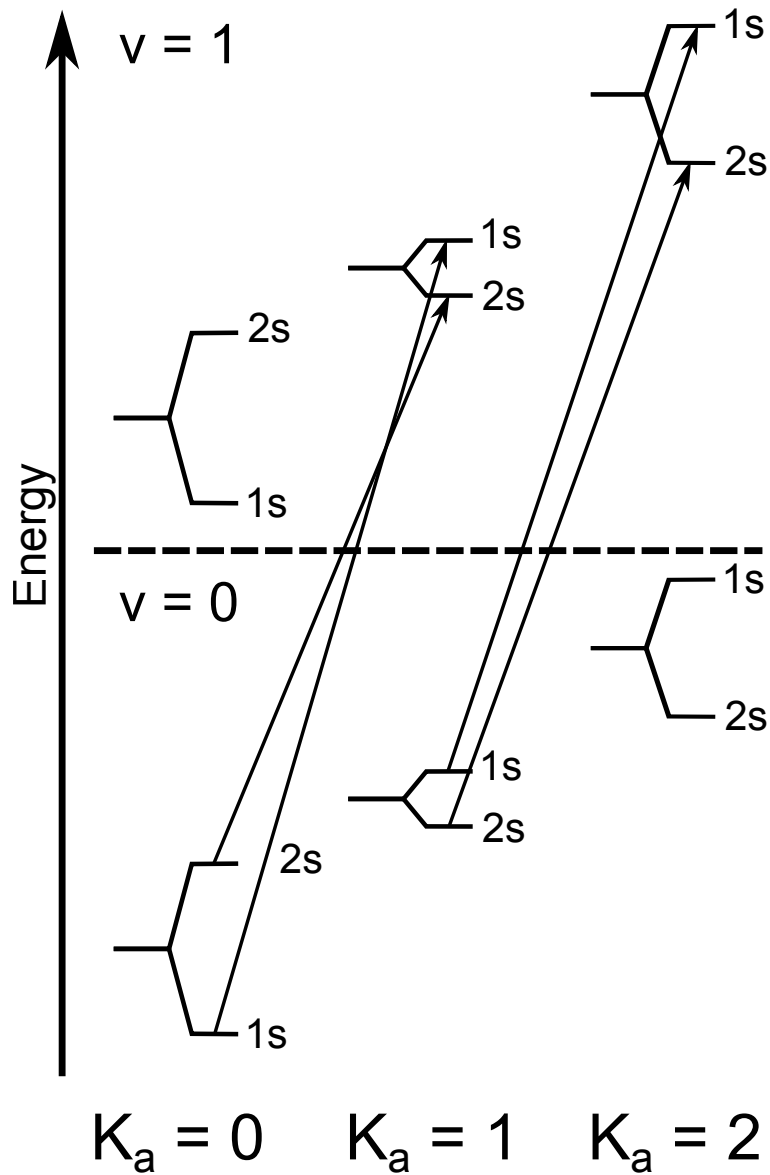


Figure 4.12: Energy level diagram for the observed  $(D_2O)_2$  bands. The 1s in the figure refer to the  $A_1^+/E_1^+/B_1^+$  tunneling levels and the 2s refer to the  $A_2^-/E_2^-/B_2^-$  tunneling levels. The bands observed in this work are indicated by arrows.

Table 4.2: Comparison of the frequency of the donor bending mode of  $(\text{D}_2\text{O})_2$  calculated in the present study to previous experimental and theoretical work.

Method	Frequency ( $\text{cm}^{-1}$ )
Gas phase <sup>a</sup>	1182.2
Ne matrix <sup>b</sup>	1192.2
Ar matrix <sup>c</sup>	1189.1
Kr matrix <sup>d</sup>	1187.0
$\text{N}_2$ matrix <sup>e</sup>	1192.7
<i>para</i> - $\text{H}_2$ matrix <sup>f</sup>	1190
DFT <sup>f</sup>	1176
MULTIMODE <sup>g</sup>	1183

<sup>a</sup> Present work

<sup>b</sup> Ref. [98]

<sup>c</sup> Ref. [94]

<sup>d</sup> Ref. [96]

<sup>e</sup> Ref. [97]

<sup>f</sup> Ref. [99]

<sup>g</sup> Ref. [90]

tunneling levels provides the difference of the acceptor switching tunneling splittings for the ground state  $K_a = 1$  level and the excited state  $K_a = 2$  level. If we again use the estimate of Paul et al. of 17 GHz for the splitting in the ground state  $K_a = 1$  level, the splitting for the excited state  $K_a = 2$  level is calculated to be  $1.5 \text{ cm}^{-1}$ , or 44 GHz. This is again similar to the value of 42 GHz estimated by Paul et al. for the ground state  $K_a = 2$  level. These results indicate that the excitation of the donor bend does not have a significant effect on acceptor switching tunneling. This is unsurprising, considering that the bending motion of the hydrogen bond donor would be unlikely to affect the tunneling motion of the hydrogen bond acceptor. In contrast, excitation of the donor bend appears to have a significant effect on the interchange tunneling motion, as noted previously.

It would be quite interesting to observe additional sub-bands of the donor bend, as well as to observe the acceptor bend, but these bands lie outside the current frequency range of our spectrometer. Based on our observations, the average of the  $A_1^+/E_1^+/B_1^+$  and  $A_2^-/E_2^-/B_2^-$  levels of the  $K_a = 0 \leftarrow 1$  band should lie at  $\sim 1178.2 \text{ cm}^{-1}$ . The MULTIMODE calculations of Wang et al.[90] predict that the acceptor band center lies at  $1175 \text{ cm}^{-1}$ . The QCL used for this work can only go as low as  $\sim 1182 \text{ cm}^{-1}$ , but we have recently constructed an external cavity QCL (EC-QCL) system in collaboration with Gerard Wysocki at Princeton that can tune from  $\sim 1135\text{--}1220 \text{ cm}^{-1}$ . This new laser should make it possible to observe the additional sub-bands of the donor bend and the acceptor bend once it is completely integrated into our spectrometer. It would be especially interesting to observe the effect of excitation of the acceptor bend on the acceptor

switching tunneling splittings.

## 4.6 Conclusions

We have reported the first rotationally-resolved spectra of the bending mode of the hydrogen bond donor of water dimer. Two  $\Delta K_a = +1$  bands were observed, and additional bands are almost certainly present, but outside the frequency coverage of our spectrometer. Both components of the acceptor switching tunneling doublet were observed for each band, which allowed us to estimate the acceptor switching tunneling splittings in the donor bend excited state based on previous estimates of the ground state splittings. We found that excitation of the donor bend has little effect on the acceptor switching tunneling. We have also determined the band center of the donor bend to be  $1182.2 \text{ cm}^{-1}$ , which is in good agreement with previous theoretical predictions. Excitation of the donor bend does have a significant effect on the interchange tunneling, which made it difficult for us to obtain a detailed assignment of the individual tunneling components arising from this tunneling. The acceptor bend and additional bands of the donor bend should be easily observable using a light source with broader frequency tuning, which will allow additional insight into this fascinating molecular system.

## Chapter 5

# Development of an External Cavity Quantum Cascade Laser Spectrometer

### 5.1 Introduction

As can be seen from the work presented in the previous chapters, QCLs are a valuable resource for performing high-resolution infrared spectroscopy. QCLs are able to provide narrow-linewidth infrared light with sufficient power to perform highly sensitive spectroscopic techniques. The major drawback of using QCLs, though, is that individual QCLs generally provide only a small frequency range over which they can be tuned. For example, the Fabry-Perot lasers used in the work presented in Chapters 2–4 have a maximum tuning range of  $\sim 20 \text{ cm}^{-1}$  ( $\sim 1180\text{--}1200 \text{ cm}^{-1}$ ), though individual lasers typically had a smaller tuning range and/or gaps in the frequency coverage. To increase the utility of QCLs for spectroscopy, much effort has been devoted to increasing the frequency tuning of individual lasers. For an excellent review of recent developments in QCL technology, including development of broadband QCL sources, see Ref. [106].

The first development which has made this possible are new designs for QCL active regions which significantly increase the gain bandwidth of the laser. One approach to increasing the bandwidth has been to embed two or more active region designs into a single chip, allowing the device to produce light at multiple wavelengths simultaneously.[107, 108] Another approach has been to use a so-called “bound-to-continuum” design of the active region.[109, 110, 111] In this design, the lower state of the transition which gives rise to lasing is actually a series of closely-spaced energy levels. Instead of lasing only occurring between two distinct energy levels, the electron can access many different lower levels, with each separate level giving rise to a photon with a different energy. This creates a QCL chip with a much broader gain bandwidth than typical QCLs. In practice, both of these strategies can be combined to generate QCLs with broadband gain media.

For high-resolution spectroscopy, it is still necessary to select a narrow frequency range from the broad gain profile to make the laser useful. For broad-gain QCLs, the solution to this problem is to place the laser in an external cavity setup to provide frequency selection.[112, 113, 114, 115] The work presented in this chapter outlines the construction of an external cavity QCL system for use in the McCall group for high-

resolution spectroscopy. This work has been done in collaboration with Gerard Wysocki and his group at Princeton University. The QCL chip used for this work was provided by the Wysocki group. The data sheet provided with the QCL chip, including LIV curves and previous performance of the laser in the Wysocki group, is provided as Appendix A.

## 5.2 Basic Design of the Laser

The essential goal of an external cavity system is to provide frequency selection for the output from a broadband QCL chip. The work presented here follows the ideas and design presented in Refs. [114] and [116]. The basic design of the external cavity is presented in Figure 5.1. The QCL is housed in a laser mount, which is placed under vacuum to prevent condensation on the laser chip, which could potentially damage the QCL. Inside the mount, the QCL is in thermal contact with a large copper block, which is connected to a thermoelectric cooler (TEC), which maintains the QCL at a constant temperature. The laser mount is also cooled via chilled water, which carries away excess heat from the mount. The light from the laser is highly divergent, and must be focused by a collimating lens to generate a usable beam. After being focused by the collimating lens, the light from the laser strikes a diffraction grating, which is mounted on a rotation stage. The diffraction grating forms one side of the external cavity, and the rear facet of the laser, which is HR-coated, forms the other. The first-order diffraction from the grating is sent back towards the laser to form the external cavity, while the zero-order reflection from the grating provides the output beam which is used for spectroscopy. This zero-order beam is sent to an output mirror, which reflects the light into the rest of the spectrometer. The output mirror is mounted on the same rotation stage as the grating, which is essential for ensuring the beam pointing does not change during operation of the laser.

For the EC-QCL system developed in the McCall group, we have housed the laser in a QCL mount purchased from ILX Lightwave (part number LDM-4872). The mount has an integrated TEC, temperature sensor, vacuum ports, and fittings for chilled water, allowing the laser temperature to be kept constant to  $\pm 0.001$  °C during operation. The TEC is controlled by a temperature controller which was also purchased from ILX Lightwave (part number LDT-5980), and can be operated with currents from -3 to +10 A. The mount is evacuated using a turbomolecular pump backed by a diaphragm pump, which is used to prevent any oil from backstreaming into the laser mount. The system is continuously pumped, because it was found that there were sufficient leaks in the mount to lead to condensation if the mount was simply closed off. Chilled water is supplied to the system by a dedicated water chiller (Anova A-15), which is generally maintained at 11°C. The ILX Lightwave mount also has built-in electrical connections for supplying current to the laser

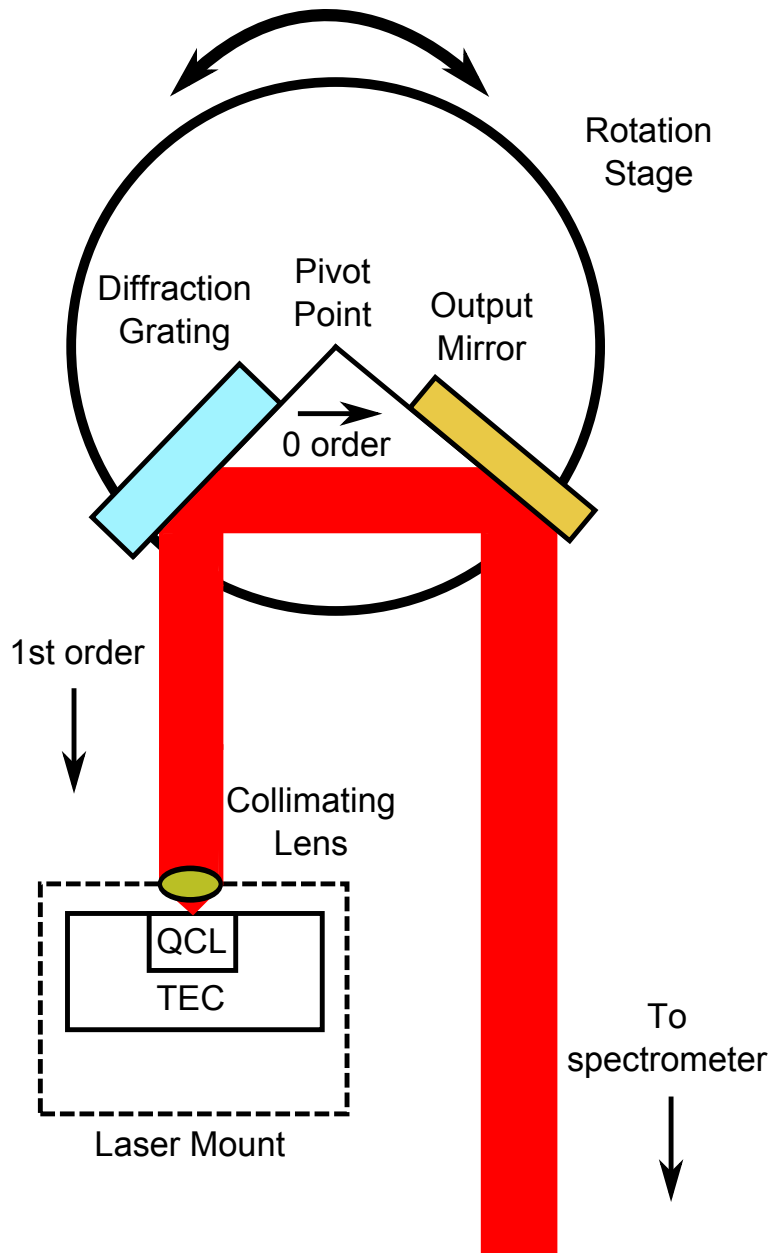


Figure 5.1: Schematic diagram of the external cavity QCL system. QCL indicates the laser chip and TEC represents the thermoelectric cooler the chip is mounted on. Zero-order light from the diffraction grating leaves the external cavity and is sent to the output mirror and on to the spectrometer. 1st order light from the grating is sent back to the QCL, forming the external cavity. The grating can be rotated using the rotation stage, and the distance from the QCL to the grating can be controlled by a translation stage (not pictured). Drawing is not to scale.

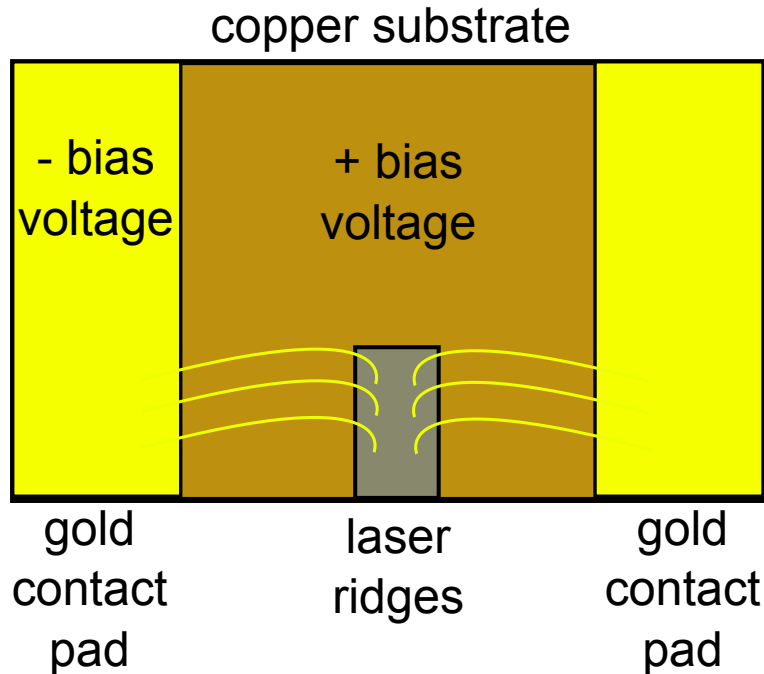


Figure 5.2: Illustration of the proper bias voltages for the laser from Princeton to ensure the laser is not damaged. Positive bias voltage is applied to the copper substrate and negative bias voltage is applied to the gold contact pad on the side of the copper substrate. The thin yellow lines represent gold wires used to connect the contact pads to the laser ridges.

to produce light. To provide power to the laser, a low-noise power supply from ILX Lightwave is used (part number LDX-3232). This power supply was also used with the liquid nitrogen cooled laser system, and was found to have excellent current stability and low noise suitable for use in a QCL system.

It is critical to mount the laser chip properly to avoid damaging it. If the wrong bias is applied to the QCL, it will permanently damage the laser. For the QCL chip from Princeton, positive bias needs to be applied to the copper substrate the chip is mounted on, while negative bias is applied to the gold pad on the side of the laser chip. This is illustrated in Figure 5.2. The mount is constructed such that the electrical leads to the laser can be placed in any necessary arrangement for running the laser. To ensure good thermal contact between the QCL and the copper mount, both the mount and the bottom of the laser substrate were cleaned with acetone. Vacuum grease (Dow Corning High Vacuum Grease) was then placed on the copper mount before placing the laser on the mount. The laser was clamped down with the screws present in the ILX Lightwave mount to keep good thermal contact and to ensure the laser does not move during operation.

The other important element of the external cavity system is the diffraction grating and output mirror setup. The diffraction grating used in the EC-QCL was purchased from Optometrics (part number ML-304). The grating has 135 grooves/mm, and has an absolute efficiency  $>90\%$  from  $\sim 6.5\text{--}13.5\ \mu\text{m}$  for s-polarized

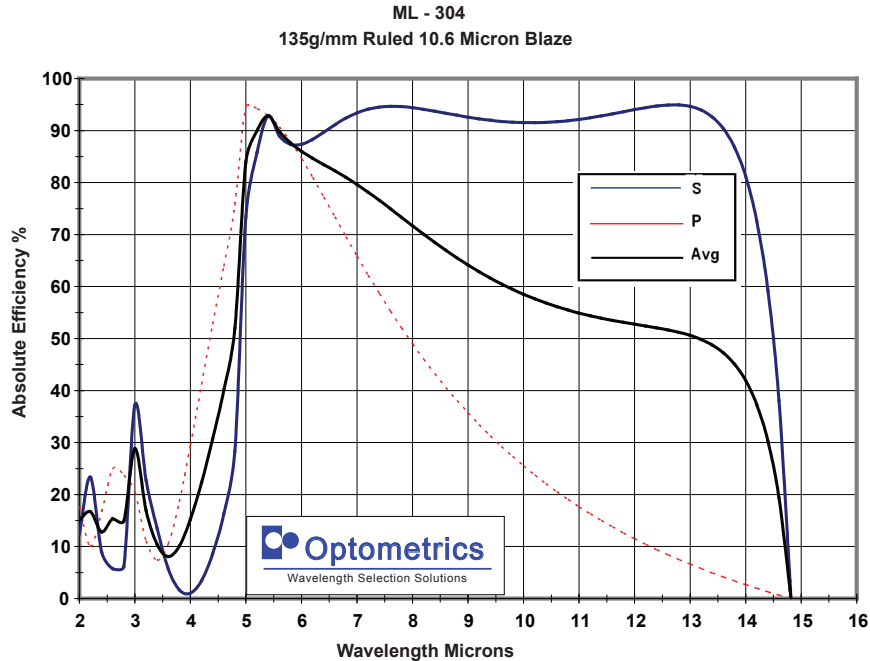


Figure 5.3: Absolute efficiency of the diffraction grating used in the EC-QCL setup versus wavelength. The absolute efficiency is plotted for both s- and p-polarized light, as well as an average efficiency for unpolarized light. The data were obtained from Optometrics.

light (see Figure 5.3). The output mirror is a simple gold mirror from ThorLabs. Both the diffraction grating and the output mirror are attached to aluminum plates, which are mounted on kinematic mounts to allow precise alignment. The diffraction grating and output mirror are placed on a rotation stage to allow control of the angle of the diffraction grating. To prevent the output beam of the laser from changing its pointing when the diffraction grating is rotated, the diffraction grating and output mirror are arranged such that the planes of the reflecting surfaces for each element intersect at the center of the rotation stage. The practical means by which this is achieved is outlined in the description of aligning the EC-QCL system below.

To control the output frequency of the laser, both the length of the external cavity and the angle of the diffraction grating need to be precisely controlled. To achieve this, the grating (and output mirror) are mounted on top of a rotation stage (Physik Instrumente M-036.DS1), which is itself mounted on top of a translation stage (Physik Instrumente M-011.00). Both of these stages are further mounted on a tilt stage (Newport TGN80), which allows the angle of the entire apparatus with respect to the ground to be adjusted. Both the rotation stage and the translation stage can be controlled via piezoelectric transducers (PZTs), and the rotation stage can also be coarsely controlled using a DC motor. The maximum travel of the PZT is  $90 \mu\text{m}$  for the translation stage, and  $700 \mu\text{rad}$  for the rotation stage. A photograph of the entire apparatus after assembly is presented in Figure 5.4, with the various parts labeled. Because the different

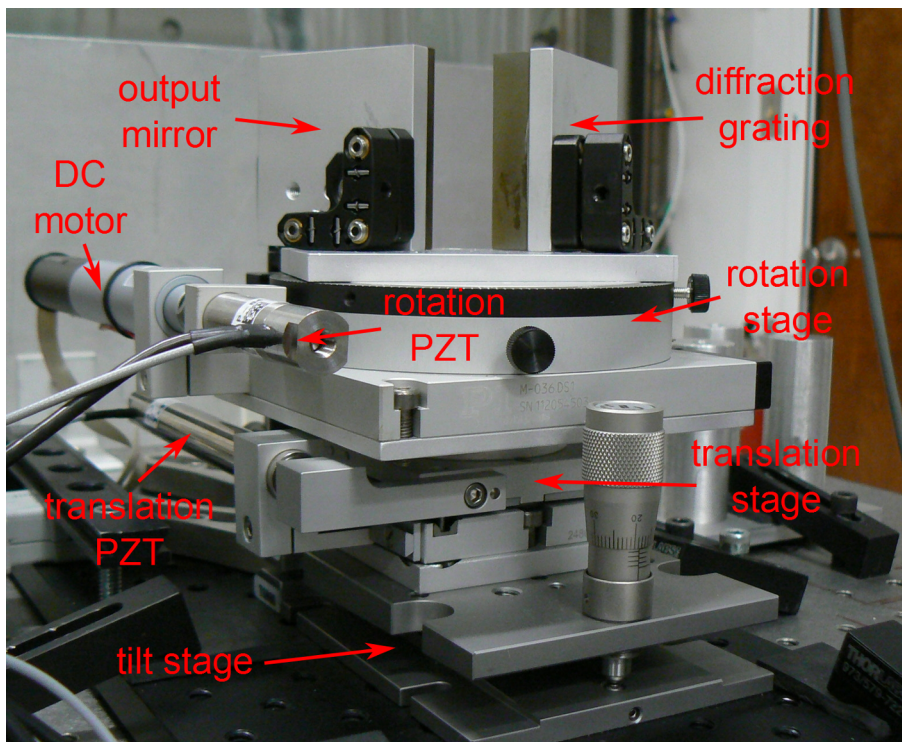


Figure 5.4: Photograph of the stack of stages underneath the diffraction grating and output mirror. The various parts are labeled in the figure.

pieces of equipment were different sizes and had different hole patterns, it was necessary to have aluminum pieces machined to fit the different stages together.

As a final note, as Figure 5.3 shows, the efficiency of the diffraction grating is highly dependent on the polarization of the light from the laser. The polarization also affects the performance of other elements of our spectrometer, especially the acousto optic modulator (AOM) which we use as a fast light switch for cw-CRDS. The output of a QCL is inherently polarized perpendicular to the direction that the electrons travel in the QCL active region. Because the laser is mounted such that the active region is vertical in the ILX Lightwave mount, the entire mount must be oriented at  $90^\circ$  to produce s-polarized light for the diffraction grating. This was achieved by attaching the laser mount to an angle brace, which was then rigidly mounted on the optics table to ensure the mount remains stable. An additional post was placed under the laser mount to bear some of the weight.

Figure 5.5 shows a photograph of the entire setup after everything is assembled. The diffraction grating and various stages are mounted on their own optical breadboard to allow them to be easily moved for alignment purposes. To try and minimize vibrations being coupled into the system, ultra-soft polyurethane rubber was placed beneath the breadboard and beneath the posts attached to the angle brace where the

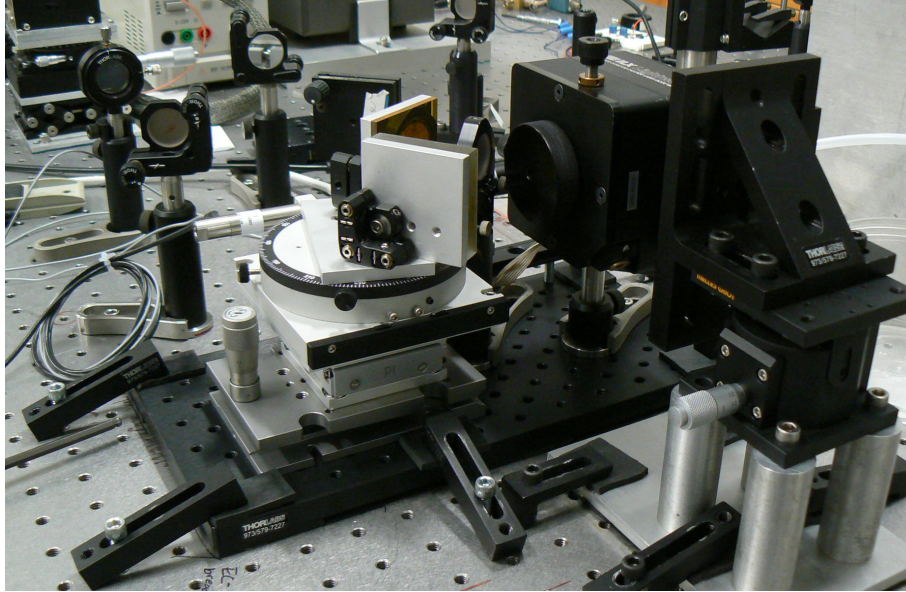


Figure 5.5: Photograph of the entire EC-QCL setup when all of the component parts are assembled. The laser mount is on the right of the photograph, and is mounted sideways to ensure the proper polarization for the diffraction grating. The knobs on the top and left side of the mount (not pictured here) are for aligning the collimating lens of the laser mount. The diffraction grating and output mirror are on top of the stack of stages in the middle of the photograph.

laser mount is attached. The entire system is fairly compact, and has an advantage over our previous QCL in that no cryogenic cooling is required to maintain operation of the laser.

### 5.3 Aligning the System

To get the EC-QCL working, it is necessary to obtain good alignment of all of the optical elements. This is achieved in several steps. First, the diffraction grating and output mirror are aligned to ensure that the laser beam pointing will not change when the angle of the rotation stage changes. Second, the collimating lens is aligned to give a collimated beam from the laser mount. Finally, the laser mount and diffraction grating are put together and aligned with each other to create the external cavity and obtain a fully working system.

To align the diffraction grating and output mirror, it is easiest to use a low power visible laser to see whether the zero order beam from the grating travels when the rotation stage is rotated. A green laser pointer, placed in a stable mount, was used for this purpose. Before using the visible laser, the diffraction grating and output mirror are coarsely aligned by eye to get the planes of the reflecting surfaces of the two elements close to intersecting at the pivot point of the rotation stage. Fine adjustments are then done using the kinematic mounts for each element. The visible beam was aligned straight and level and directed onto the diffraction grating. The diffracted beams are then reflected off the output mirror, and imaged onto a

piece of graph paper to make it easier to tell if the zero order beam travels when the rotation stage is rotated.

It is first necessary to find the zero order diffracted beam which is imaged onto the graph paper. The spot from the zero order beam moves the least when the diffraction grating is rotated by hand. To align the diffraction grating and output mirror, the rotation stage is rotated by hand and the movement of the zero order spot is observed. The kinematic mounts for the diffraction grating and output mirror are adjusted with the goal of having the zero order spot as stationary as possible when the rotation stage is turned through its full travel. For this particular setup, it was also necessary to add another mirror immediately after the output mirror so that the beam could be reflected away from the laser mount once the entire system was put together. Without the extra mirror, the zero order beam would have been blocked by the laser mount when the system was aligned properly.

After aligning the diffraction grating and output mirror, the collimating lens on the laser mount needs to be aligned. The first step for aligning the collimating lens on the QCL mount is to run the laser in pulsed mode. We originally attempted to obtain light from the QCL chip in cw mode using the ILX Lightwave power supply, but were never able to observe lasing from the chip when it was not in the external cavity setup. The setup for operating the laser in pulsed mode is presented in Figure 5.6. The laser is controlled via a dedicated pulser circuit (Directed Energy, Inc. PCO-7120). The circuit requires three inputs: a gate pulse to control the width and frequency of current pulses, a high voltage power supply to power the laser, and a +15 V power supply to power the circuit. The gate pulse was generated using a pulse generator (Quantum Composers Model 9518), with the pulse width set to 100 ns at a duty cycle of 1 % and an amplitude of 10.4 V. The high voltage was supplied using a simple variable DC power supply (Circuit Specialists CSI12001X). The amplitude of the current pulse sent to the laser is controlled by varying the voltage of this power supply. The threshold voltage where lasing was initially observed was  $\sim 12$  V on the high voltage power supply.

Once the laser is running in pulsed mode, the beam can be imaged directly and collimated using the built-in collimating lens in the laser mount. The lens is xyz adjustable even under vacuum, which greatly aids the alignment process. For initial viewing of the laser light, a thermal camera was used (FLIR Thermacam 320EX) to observe the beam directly. The thermal camera is highly sensitive to infrared radiation, and is useful for finding the initial beam which is not well collimated. By adjusting the position of the lens (particularly the distance of the lens from the laser), the diffuse beam can be focused into a tighter spot. Once the beam begins to be focused, the thermal camera is no longer necessary and could suffer damage from the high laser power. At this point, it is much easier and safer to use an infrared beam profiler. The profiler used to observe the QCL beam was a Pyrocam III from Ophir Spiricon. The profiler was run in cw mode, which gave a good image of the beam even though the laser was being run in pulsed mode. Once the

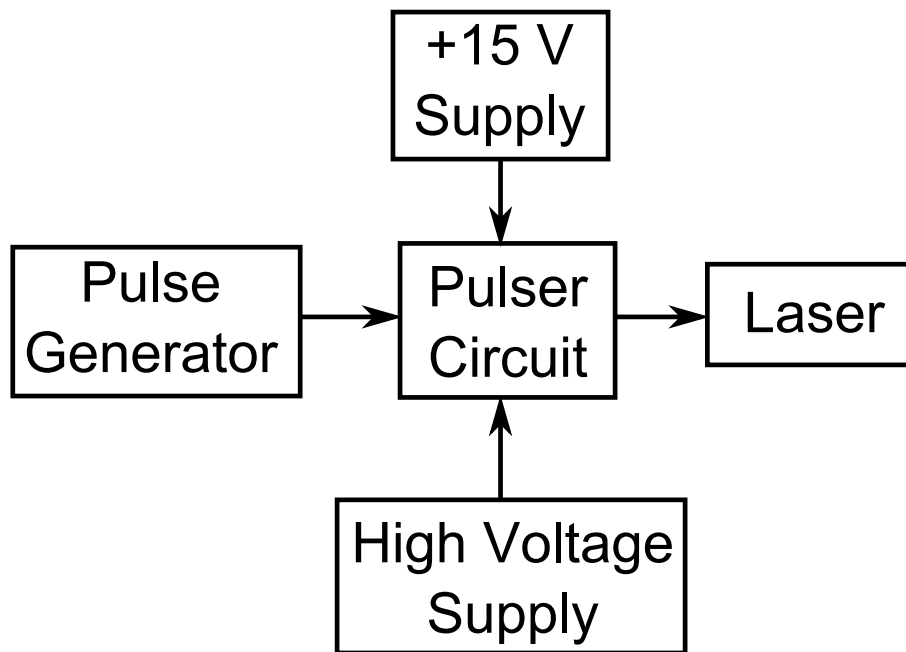


Figure 5.6: Diagram of the setup used to run the EC-QCL system in pulsed mode for aligning the collimating lens. A pulse generator provides a gate pulse to the pulser circuit, which is powered by a +15 V power supply. The current used to supply the pulse to the laser is provided by a high voltage power supply. The voltage of the high voltage power supply is adjusted to control the amplitude of the current pulse that is sent to the laser. For the system described here,  $\sim 12$  V was necessary to observe light from the QCL. The pulse generator was set to produce 100 ns pulses at 10.4 V and a duty cycle of 1 %.

beam can be viewed on the beam profiler, it can be collimated by sending the beam several meters along a straight path and focusing the beam as far from the laser mount as is possible by adjusting the position of the collimating lens.

Once the QCL is collimated and the diffraction grating and output mirror are aligned, the two systems can be put together to create the full EC-QCL setup. The laser mount is placed sideways by attaching it to an angle brace as shown in Figure 5.5. A level is used to ensure that the laser mount is pointed straight and level on the optics table and that the diffraction grating is also level with the table. Once the laser mount and diffraction grating are in the proper position, the laser is run in pulsed mode and the beam reflected off the output mirror is observed with the beam profiler to make sure that the profiler is placed in the correct position to observe the output beam when the EC-QCL is fully aligned and working. Once the profiler is in the right place, the laser is run in cw mode at a current that will be above the expected threshold for the EC-QCL system. If everything is properly aligned, an output beam will be observed on the beam profiler. This is unlikely to happen immediately, especially when initially aligning the system after setting everything up. If no light is observed from the EC-QCL, it is usually necessary to adjust the angle of the diffraction grating by hand until light is observed. The system will lase at only a fairly narrow range of angles, so the rotation stage needs to be adjusted carefully when trying to observe light. It was also seen that adjusting the z axis of the collimating lens (distance from the lens to the laser) could be used to observe initial light. Adjusting the lens must be done carefully because the performance of the system is highly sensitive to this degree of freedom.

Once initial light is observed from the EC-QCL in cw mode, the alignment of the system needs to be fine-tuned to achieve the best performance of the laser. The goal is to get the threshold of the EC-QCL at the lowest possible current. This gives the greatest tunability and the most optical power for the system. There are many degrees of freedom in the system that can be adjusted to try and lower the threshold current, but the most important ones are the tilt of the diffraction grating relative to the optics table, the angle of the diffraction grating, and the z position of the collimating lens. The easiest way to minimize the threshold current of the laser is to lower the current until the beam is almost gone on the beam profiler, then to adjust one of the degrees of freedom to make the laser bright again. By repeating this process for the different degrees of freedom, the best alignment can be achieved.

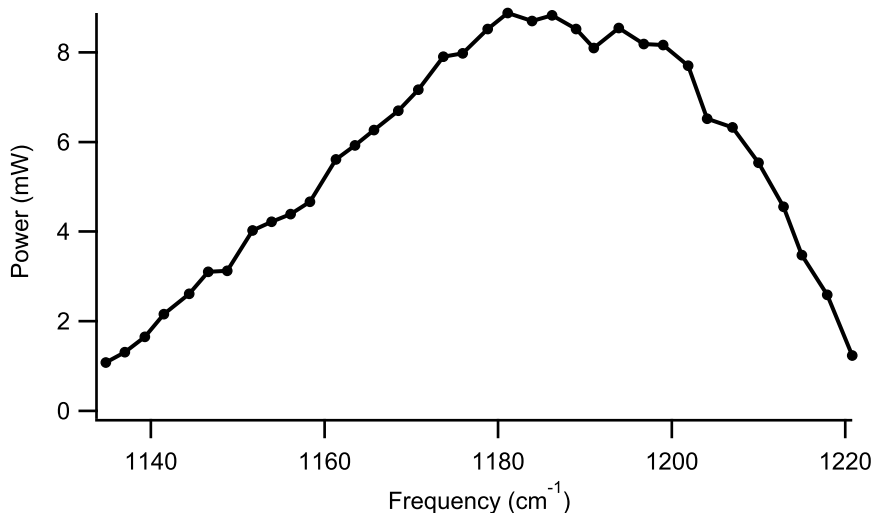


Figure 5.7: Measured optical power of the EC-QCL plotted as a function of the laser frequency. The frequency was tuned through the entire range by adjusting the angle of the diffraction grating using the DC motor to provide coarse rotation adjustments.

## 5.4 Laser Performance

After aligning and optimizing the EC-QCL by following the procedures outlined in the previous section, the power and frequency tuning of the laser were measured. The power was measured by focusing the laser onto a power meter, and the frequency was measured using a mid-IR wavemeter. The power and frequency tunability of the laser are shown in Figure 5.7. As seen in the figure, the laser can be tuned from  $\sim 1135$ – $1220$   $\text{cm}^{-1}$ , which is a greater than 4-fold improvement of the tunability of the Fabry Perot QCL used for the other experiments outlined in this dissertation. The EC-QCL covers the same range as the previous QCL, but also allows access to frequencies to the red and blue of that range. This will make it possible to observe many new molecular targets. The optical power of the EC-QCL over this frequency region is  $>1$  mW, and reaches over 8 mW at the center of the frequency coverage near  $1180$   $\text{cm}^{-1}$ . This amount of optical power is sufficient to perform cavity ringdown spectroscopy and will allow the laser to be used for highly sensitive spectroscopy over the entire tuning range.

A possible concern with using the EC-QCL for cavity ringdown spectroscopy is that the beam pointing might change significantly enough to cause the laser to be mis-aligned with the high finesse cavity as the frequency of the laser is scanned. To test whether this would be a problem, the cavity ringdown spectrometer was aligned using the EC-QCL. Once the ringdown cavity was aligned, the laser was coarsely tuned through its entire tuning range by using the DC motor on the rotation stage. As the laser was tuned, the build-up events on the ringdown detector were monitored using an oscilloscope. No change in the strength or frequency

of the cavity build-up events was observed while tuning the laser, indicating that the beam pointing did not change significantly enough to cause problems with alignment of the ringdown cavity.

Though the EC-QCL has good frequency tuning and pointing stability, the frequency stability of the laser is currently worse than the Fabry Perot QCL. This has been directly observed in two ways. First, when aligning the ringdown cavity, build-up events occur even when the cavity piezo is off and the cavity length is fixed. This means that the frequency of the laser is jittering by more than half of the free spectral range of the cavity, which is  $\sim 185$  MHz. Second, when the frequency of the EC-QCL is measured using the wavemeter, the frequency jitter can be directly observed. When the laser was held at a fixed frequency and observed using the wavemeter, the standard deviation in the frequency measurements was  $0.0075 \text{ cm}^{-1}$  (225 MHz). This amount of frequency jitter will make it difficult to resolve narrow absorption lines, so it will be necessary to reduce the jitter. The source of the jitter is still being investigated, but it is likely due to mechanical vibrations being coupled into the external cavity. This may be due to the vacuum pump or water chiller attached to the laser mount. It may be possible to reduce the frequency jitter of the laser by locking it to our ringdown cavity using the Pound-Drever-Hall locking technique. This would have the added benefit of allowing us to implement high repetition rate cavity ringdown spectroscopy.[48]

## 5.5 Mode-hop Free Tuning

With the Fabry Perot QCL used previously in our group, frequency tuning was accomplished by fixing the laser temperature and stepping the current applied to the laser. This produced a reproducible linear frequency tuning response which was generally free from mode hops. A similar approach with the EC-QCL does not provide mode-hop free tuning, because there are now three frequency selecting elements which need to be controlled to prevent mode hops, i.e. the laser current, the external cavity length, and the angle of the diffraction grating. A detailed model of this behavior is provided in Ref. [114], which has been the basis of implementing mode-hop free tuning in the EC-QCL.

To control the external cavity length and the angle of the diffraction grating, two channels of a three-channel piezo controller (ThorLabs MDT693A) are used to send signals to the PZTs attached to the translation stage and rotation stage, respectively. The voltages to control the three tuning elements are produced by a National Instruments data acquisition (DAQ) board (PCI-5122), with the values set by the software used to control the instrument. As described in Appendix C, the current of the laser is controlled by sending a constant voltage to the modulation input of the laser current driver. The 0–10 V signal produced by the DAQ board is sent through a homebuilt 30:1 voltage divider before being sent to the modulation input of the

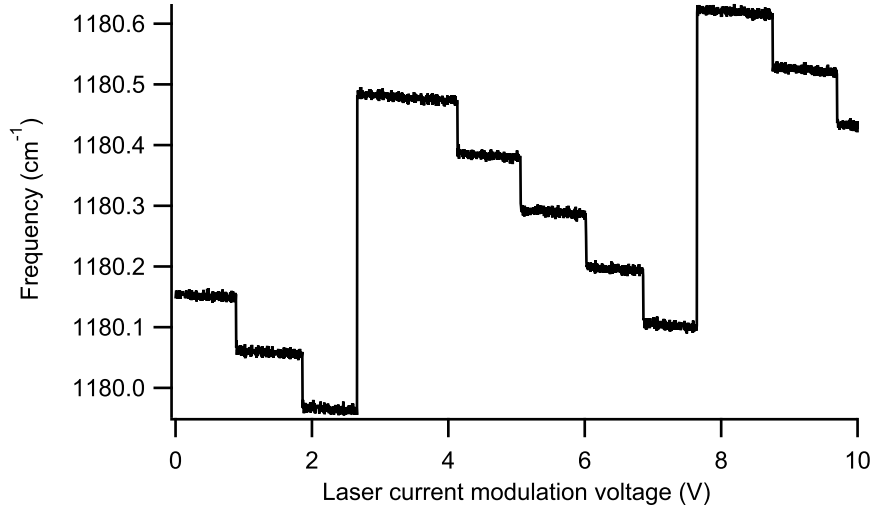


Figure 5.8: Frequency of the EC-QCL as measured by a wavemeter versus modulation voltage applied to the EC-QCL current driver when only the current applied to the laser is varied. The frequency axis shows regular mode-hops, with the smaller mode-hops arising from the external cavity modes and the larger mode-hops arising from the QCL chip modes.

laser driver. The voltage divider is used to reduce electrical noise in the signal. To control the translation and rotation stages, a multiple of the voltage sent to the current driver is sent to the two channels of the piezo controller. With the proper multiplication factors for the rotation and translation stages, mode-hop free tuning can be achieved.

Figure 5.8 shows a plot of the frequency of the laser, as read by a mid-IR wavemeter, as a function of the change in laser current when the other tuning elements are fixed. As can be seen, the laser can only scan a short distance in frequency space before suffering a mode-hop. There are two different types of mode-hops that are observed. The smaller jumps in Figure 5.8 are due to the laser hopping to different modes of the external cavity. These hops are  $\sim 0.09 \text{ cm}^{-1}$ , which corresponds to a cavity of length 5.5 cm (assuming the index of refraction is unity), which agrees well with the approximate distance from the QCL chip to the diffraction grating. The larger mode-hops in Figure 5.8 are due to the laser hopping to different modes of the cavity formed by the front and back facets of the laser chip. These mode-hops are  $\sim 0.5 \text{ cm}^{-1}$ , which is reasonable considering the length of the QCL chip and the high index of refraction for the semiconductor materials used to fabricate the chip.

When only the rotation stage is scanned, the number of mode-hops decreases, as can be seen in Figure 5.9. This figure shows the reading from the wavemeter as a function of the voltage applied to the piezoelectric transducer which controls the rotation stage of the EC-QCL. Though this type of tuning allows a larger frequency range before a mode-hop occurs, it is still not usable for scanning any significant portion of

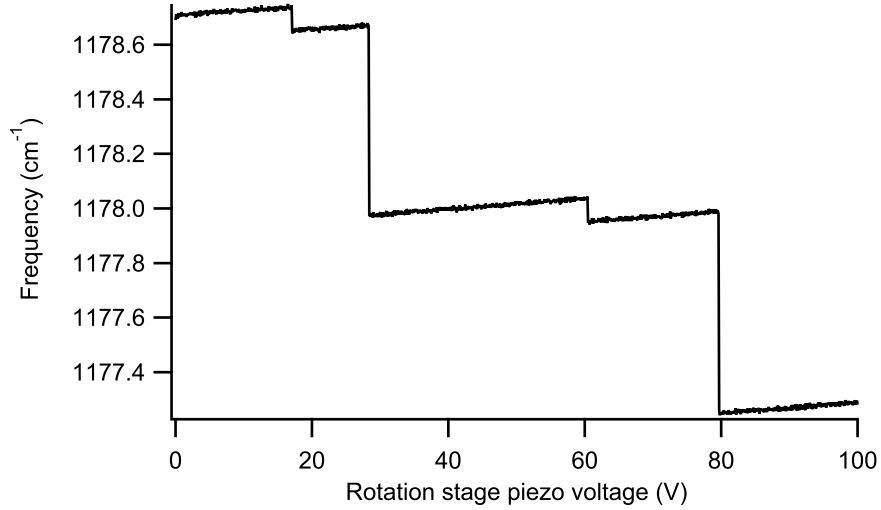


Figure 5.9: Frequency of the EC-QCL as measured by a wavemeter versus voltage applied to the rotation stage piezo when only the diffraction grating angle is varied.

frequency space. Both external cavity mode-hops and QCL chip mode-hops occur at regular intervals, preventing mode-hop free scanning of the laser. A similar situation is present if only the length of the external cavity is scanned using the translation stage PZT.

To obtain mode-hop free scanning, all elements must be controlled simultaneously in order for the different frequency tuning elements to track one another. In practice, this can be achieved by sending different multiples of the voltage used to control the current driver to the piezos controlling the translation and rotation stages. The proper multiplication factors for the translation and rotation stages were found empirically by testing different multiplicative factors and scanning the laser while observing the frequency with the wavemeter. The factors were varied to produce fewer mode-hops, until mode-hop free tuning was achieved, as shown in Figure 5.10. For this scan, the voltage sent to the rotation stage was 14 times the current driver voltage, and the voltage sent to the translation stage was 10 times the current driver voltage. Using these parameters, the laser can be tuned over  $>0.6 \text{ cm}^{-1}$  without any mode-hops. This is similar to the range we could easily scan with our previous laser, so this amount of frequency tuning is sufficient for performing spectroscopy. The amount of mode-hop free tuning that can be achieved is limited by the travel of the translation stage PZT.

## 5.6 Future Work

The EC-QCL system is still in the process of being developed, but already shows great promise for enabling high-sensitivity, high-resolution spectroscopy over a much wider frequency range than was possible using

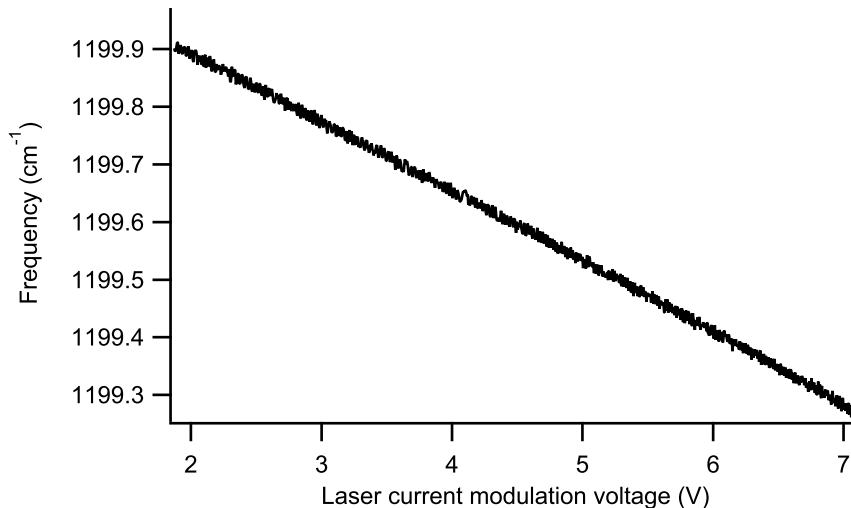


Figure 5.10: Frequency of the EC-QCL as measured by a wavemeter versus voltage applied to the EC-QCL current driver with mode-hop free tuning. The voltage sent to the rotation stage piezo was 14 times the value sent to the current driver, and the voltage sent to the translation stage piezo was 10 times the value sent to the current driver. Mode-hop free tuning was achieved over  $>0.6 \text{ cm}^{-1}$  and is limited by the travel of the translation stage piezo.

our previous Fabry Perot QCL. The frequency coverage of this particular laser will allow work to continue toward obtaining a high-resolution spectrum of  $\text{C}_{60}$ , and can also be used to extend the frequency coverage of the bending modes of  $(\text{D}_2\text{O})_2$ . Much work in the McCall group is also focused on ions of astrochemical and fundamental relevance, and the EC-QCL will enable vibrational bands of some of these ions to be observed at a lower frequency than is possible with other laser sources in the group. Two ions of particular interest are  $\text{H}_5^+$  and  $\text{CH}_5^+$ . Previous measurements of both ions have shown that they have vibrational bands that should be accessible with the EC-QCL system.[117, 118] These previous measurements were at low resolution and were unable to resolve the rotational structure of the absorption bands, while the EC-QCL system should be able to allow high-resolution spectroscopic studies of these important ions.

An additional advantage of the EC-QCL system described in this chapter is that it can be used for QCL chips throughout the mid-IR. Though the system has been developed to work specifically near  $8.5 \mu\text{m}$ , the optical elements in the EC-QCL can work across a fairly broad wavelength range. The only optical element in the laser mount is the collimating lens. This lens has an anti-reflection coating that is designed to work from  $7\text{--}14 \mu\text{m}$ , so it should be usable for any laser chips designed for this frequency range. The diffraction grating is the other critical optical element in the EC-QCL system, and as shown in Figure 5.3, the grating has  $>90\%$  absolute efficiency over most of the  $7\text{--}14 \mu\text{m}$  region. This level of performance would allow the grating to be used for any QCL chip designed to lase throughout this region of the spectrum. By obtaining different QCL chips throughout this  $7\text{--}14 \mu\text{m}$  region, it would be possible to perform high-resolution spectroscopy of

any molecule with an absorption band in this region, which is an enormous improvement over the limited tunability of our previous spectrometer.

## Appendix A

# Data sheets for the QCL chip used in the external cavity QCL system

The following data sheets were provided by the Wyoski group when the broadband QCL was loaned to the McCall group. The sheets provide measurements of the resistance of the laser, instructions for proper connections, an LIV curve, and tuning ranges achieved in an external cavity setup at Princeton. The sheets also provide pictures of front and back facets of the laser chip.

Nov 2, 2010

## 3521A1dn Report

### Dimensions:

Length: 2.05mm

Ridgewidth: 10 microns

### Connections:

★ Epi-up: Top contact (-), substrate (+)

Laser at RT: FWD: 540 $\Omega$  916 $\Omega$

Laser at -25C: FWD: 2.6 k $\Omega$

### Common Settings:

Use 6mm broadband lens

House chilled water at ~ 15-16 degC

TEC temperature: -23 degC (using ThorLabs diode/TEC driver)

Current source: ILX LDX 3232

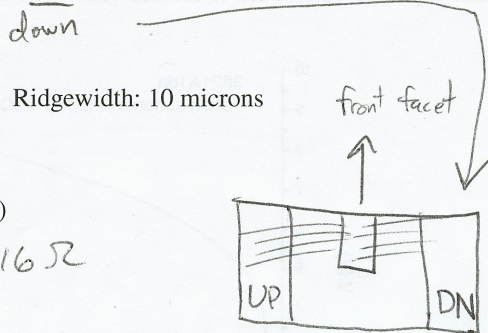
Limits: 600mA limit current; 5W (default) limit P; 0.00 Cal PD; 10V compliance voltage

Piezo control: ThorLabs

### Tips:

Increase current slowly, pausing every 50mA to allow TEC to chill and catch up. Typically takes ~30s for the TEC to recover from 50mA change

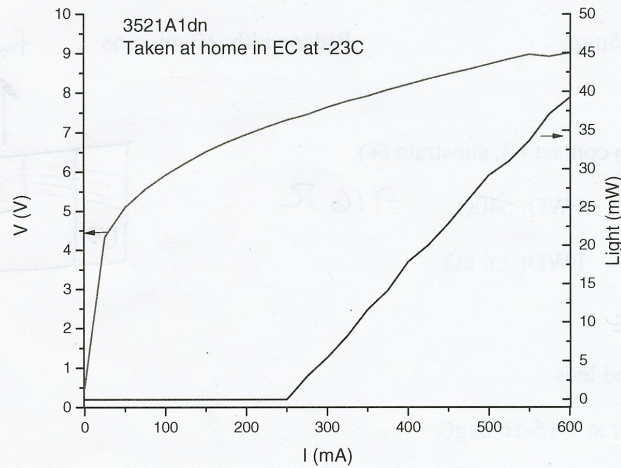
When reading the compliance voltage, at 0mA, it starts increasing like crazy. Look at 10mA = 3.436V



Nov 2, 2010

**LIV:**

Threshold at pulsed outside EC is around 432mA or 9.66V



**Tuning range:**

At 475mA, there was still no mode hopping back to main laser mode. Therefore, the tuning range can be  $>161 \text{ cm}^{-1}$  if we decide to push the current further.

300mA:  $76.4 \text{ cm}^{-1}$   
4e5 steps =  $1130.29 \text{ cm}^{-1}$   
-2.8e5 steps =  $1206.69 \text{ cm}^{-1}$

375mA:  $115.2 \text{ cm}^{-1}$   
2mm =  $1110.4 \text{ cm}^{-1}$   
-1.65mm =  $1225.6 \text{ cm}^{-1}$

400mA:  $128.9 \text{ cm}^{-1}$   
6e5 steps =  $1106.6 \text{ cm}^{-1}$   
-5.5e5 steps =  $1235.5 \text{ cm}^{-1}$

475mA:  $161.1 \text{ cm}^{-1}$   
8e5 steps =  $1249 \text{ cm}^{-1}$   
-6.5e5 steps =  $1088.4 \text{ cm}^{-1}$

**Mode Hops and Resonances:**

QCL length = 2.05 mm  
QCL FSR =  $0.76 \text{ cm}^{-1}$   
EC free space length = 42mm  
EC FSR =  $0.0934 \text{ cm}^{-1}$   
Ratio (Amplified piezo voltage/ current mA) =  $0.5418 \text{ V/mA}$

Nov 2, 2010

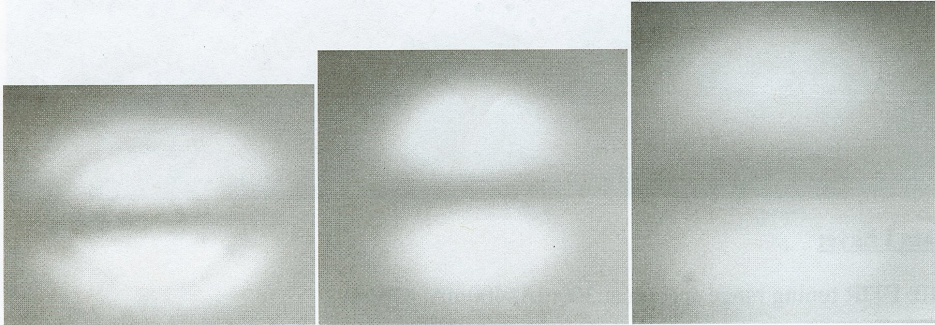
**Laser beam pictures:**

Taken at -25C pulsed mode at 9.75V or 456mA:

Closest

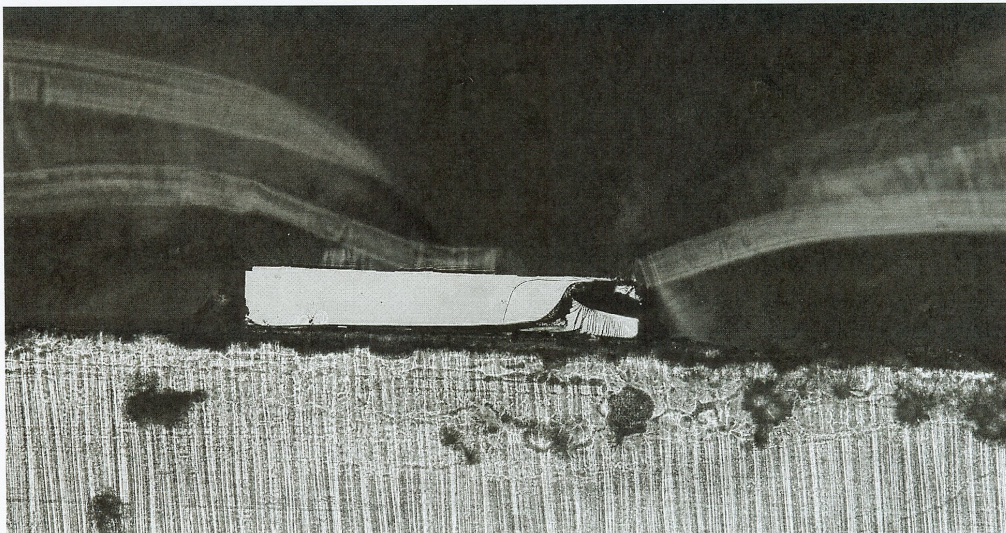
Midway

Farthest (at higher current)



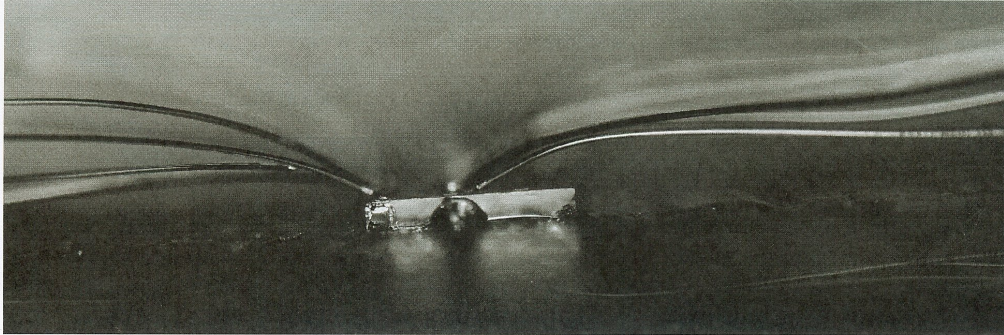
**Facet Pictures:**

Front Facet: 10x



Nov 2, 2010

Back Facet: 5x



**What data I have:**

10\_13\_10: FTIR tuning range spectra at 300mA, 400mA, 475mA

10\_14\_10: Steps throughout tuning range at 375mA

10\_20\_10: Tuning only 1 element data (mainly centered at 350mA)

Attempted some active frequency locking, but current modulation depth may be too large. Zero crossings never found.

10\_22\_10: MHF tuning at different grating angles.

11\_02\_10: Facet pictures

## Appendix B

# A quantum cascade laser cw cavity ringdown spectrometer coupled to a supersonic expansion source

This appendix is reprinted in its entirety with permission from B. E. Brumfield, J. T. Stewart, S. L. Widicus Weaver, M. D. Escarra, S. S. Howard, C. F. Gmachl, and B. J. McCall, *Review of Scientific Instruments*, 81, 063102 (2010). Copyright 2010, American Institute of Physics.

## A quantum cascade laser cw cavity ringdown spectrometer coupled to a supersonic expansion source

Brian E. Brumfield,<sup>1</sup> Jacob T. Stewart,<sup>1</sup> Susanna L. Widicus Weaver,<sup>1,a)</sup> Matthew D. Escarra,<sup>2</sup> Scott S. Howard,<sup>2,b)</sup> Claire F. Gmachl,<sup>2</sup> and Benjamin J. McCall<sup>3</sup>

<sup>1</sup>Department of Chemistry, University of Illinois, Urbana, Illinois 61801, USA

<sup>2</sup>Department of Electrical Engineering, Princeton University, Princeton, New Jersey 08544, USA

<sup>3</sup>Departments of Chemistry and Astronomy, University of Illinois, Urbana, Illinois 61801, USA

(Received 1 December 2009; accepted 19 April 2010; published online 8 June 2010)

A new instrument has been constructed that couples a supersonic expansion source to a continuous wave cavity ringdown spectrometer using a Fabry–Perot quantum cascade laser (QCL). The purpose of the instrument is to enable the acquisition of a cold, rotationally resolved gas phase spectrum of buckminsterfullerene ( $C_{60}$ ). As a first test of the system, high resolution spectra of the  $\nu_8$  vibrational band of  $CH_2Br_2$  have been acquired at  $\sim 1197\text{ cm}^{-1}$ . To our knowledge, this is the first time that a vibrational band not previously recorded with rotational resolution has been acquired with a QCL-based ringdown spectrometer. 62 transitions of the three isotopologues of  $CH_2Br_2$  were assigned and fit to effective Hamiltonians with a standard deviation of 14 MHz, which is smaller than the laser frequency step size. The spectra have a noise equivalent absorption coefficient of  $1.4 \times 10^{-8}\text{ cm}^{-1}$ . Spectral simulations of the band indicate that the supersonic source produces rotationally cold ( $\sim 7\text{ K}$ ) molecules. © 2010 American Institute of Physics. [doi:10.1063/1.3427357]

### I. INTRODUCTION

High resolution midinfrared (mid-IR) absorption spectroscopy has long been used as a sensitive tool for studying the fundamental bands of vibrational modes in polyatomic molecules. These modes serve as a molecule's "fingerprints," which not only provide important information about a molecule's structure and dynamics, but can also be used to detect its presence in nonlaboratory environments, including astronomical objects. Mid-IR spectroscopy is particularly valuable for studying symmetric molecules that lack permanent dipole moments and therefore cannot be studied using pure rotational spectroscopy. Examples of symmetric molecules that have been detected in astronomical objects based on high-resolution mid-IR laboratory spectroscopy include  $H_3^+$ ,<sup>1</sup>  $C_2H_2$ ,<sup>2</sup>  $CH_4$ ,<sup>3</sup> and  $C_6H_6$ .<sup>4</sup>

The present study is motivated by the desire to search for  $C_{60}$ , which was serendipitously discovered in the laboratory during experiments designed to understand carbon star outflow chemistry<sup>5</sup> in astronomical environments. Of the four infrared active modes of  $C_{60}$ , only the mode near  $1185\text{ cm}^{-1}$  is accessible for ground-based astronomical spectroscopy, as it lies in a region where the atmosphere is relatively transparent. The two major challenges in acquiring a rotationally resolved laboratory spectrum of  $C_{60}$  are developing a spectrometer with very high resolution and sensitivity near  $8.5\text{ }\mu\text{m}$ , and preparing a sample of cold  $C_{60}$  in the gas phase. It should be noted that similar challenges apply to the spectroscopy of other large and symmetric carbon-bearing

molecules, such as other fullerenes and polycyclic aromatic hydrocarbons. These challenges can be overcome with instruments constructed using sensitive laser direct absorption techniques coupled with high-temperature supersonic expansion sources.

Historically, there have been pulsed, and a lesser number of continuous wave (cw), laser sources available in the  $8\text{ }\mu\text{m}$  region, but fewer than available in the visible and near-IR regions of the electromagnetic spectrum. Light sources such as cw optical parametric oscillators and difference frequency generation systems based on periodically poled lithium niobate (PPLN) crystals are capable of generating light spanning  $2\text{--}5\text{ }\mu\text{m}$ , but progress of cw nonlinear light generation  $>5\text{ }\mu\text{m}$  has yet to mature to the point of offering performance comparable to those of current systems based on PPLN technology.<sup>6</sup> CO and  $CO_2$  molecular gas lasers only offer partial frequency coverage from  $5\text{--}6\text{ }\mu\text{m}$  and  $9\text{--}11\text{ }\mu\text{m}$ , respectively.<sup>6</sup> Lead salt diode lasers are available in the mid-IR, but their narrow frequency coverage has limited their application.

However, the advent of quantum cascade lasers (QCLs) has enabled the fabrication of lasers with center frequencies spanning a large wavelength region in the mid-IR, using standard semiconductor materials. This is possible because the thickness of the semiconductor layers, and not their intrinsic band gap, can be varied to control the emitted photon energy.<sup>7</sup> Whereas lead salt diode lasers tend to have poor beam quality, generally low output powers ( $<1\text{ mW}$ ), and require cryogenic cooling,<sup>6,8</sup> QCLs are now available with near-Gaussian beam output profiles, tens or hundreds of milliwatts of output power, and the capability to operate at room temperature. In addition to these favorable characteristics, free-running QCLs have short-term ( $<1\text{ s}$ ) linewidths of

<sup>a)</sup>Present address: Department of Chemistry, Emory University, Atlanta, Georgia 30322, USA.

<sup>b)</sup>Present address: School of Applied and Engineering Physics, Cornell University, Ithaca, New York 14853, USA.

$\sim 1$  MHz,<sup>9</sup> and submegahertz linewidths when actively frequency stabilized.<sup>10</sup> In comparison to nonlinear light generation methods, QCLs provide narrow spectral coverage ( $\sim 20$  cm<sup>-1</sup>), but the development of external cavity systems and fabricated QCL arrays (providing broad coverage up to  $\sim 300$  cm<sup>-1</sup>) are now overcoming this difficulty.<sup>11–13</sup>

Consequently, QCLs are emerging as an attractive option for performing high resolution spectroscopy in the mid-IR, and have been successfully implemented into a variety of spectrometers utilizing wavelength modulation,<sup>14–17</sup> frequency modulation,<sup>18</sup> sub-Doppler Lamb dip spectroscopy,<sup>15,19,20</sup> integrated cavity output spectroscopy,<sup>21–25</sup> cw cavity ringdown spectroscopy (cw-CRDS),<sup>26,27</sup> and noise immune cavity enhanced optical heterodyne spectroscopy.<sup>28</sup> A majority of these studies were motivated as proof-of-concept implementations of cw-QCLs into previously existing techniques and/or for trace gas sensing pertinent to atmospheric science, biomedical breath analysis, and pollutant monitoring. However, two studies using QCL-based spectrometers have been carried out where a pulsed supersonic expansion was used to collect rotationally cold spectra of large molecules.<sup>25,29</sup>

As mentioned above, the second challenge for spectroscopy of C<sub>60</sub> or related molecules is the preparation of a sample of rotationally cold gas-phase molecules. The use of supersonic expansions for cooling large molecules is a fairly mature science.<sup>30,31</sup> For large organic molecules, laser ablation/desorption and direct heating have been used to introduce the sample into supersonic expansions.<sup>30–35</sup> Using cw-CRDS with laser ablation adds the additional complication of timing the occurrence of ringdown events with the presence of sample in the supersonic jet. Though coupling cw-CRDS to pulsed sample delivery/generation has been achieved before,<sup>36,37</sup> given the thermal stability of C<sub>60</sub> against decomposition, it is more straightforward to heat the C<sub>60</sub> sample to high temperatures to provide a continuous feed of gas phase C<sub>60</sub>. The high temperatures necessary to generate a significant C<sub>60</sub> vapor pressure preclude the use of a pulsed supersonic expansion source, and requires a high-throughput pumping system to handle the gas load of a cw supersonic expansion source.

In the following sections, we present the experimental design and implementation of our QCL-based cw cavity ringdown spectrometer. We then present the results of our spectroscopy of a test molecule, methylene bromide (CH<sub>2</sub>Br<sub>2</sub>), which demonstrates the high resolution and sensitivity of our spectrometer, as well as the effectiveness of our supersonic expansion source when operated at room temperature.

## II. EXPERIMENTAL

An overview of the apparatus is presented in Fig. 1. The system can be broken down into four principal parts: the quantum cascade laser (and its associated control electronics and housing), the optical layout, the data acquisition system, and the supersonic expansion source; each is described in detail below.

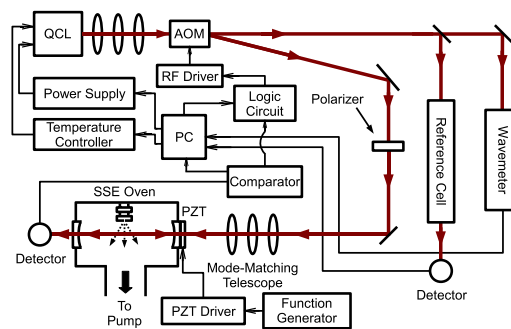


FIG. 1. (Color online) Overall experimental layout of the FP-QCL CRD spectrometer.

### A. QCL

The QCLs used in the instrument have been designed and fabricated for this experiment at Princeton, with an active region design similar to that used for previously described 8.2  $\mu\text{m}$  devices.<sup>38</sup> Unlike QCLs employing distributed feedback gratings, the lasers used in this study have short Fabry–Perot cavity lengths of  $\sim 2$  mm to reduce multimode emission at higher currents ( $\sim 700$  mA). This approach removes the complication of adding a grating to the device, while increasing the yield of devices with the desired wavelength coverage. Shorter cavity lengths lead to a trade-off in power since the gain medium length is reduced, but there is still ample power with the shorter cavity design to carry out cavity ringdown spectroscopy.

The laser is housed inside a liquid nitrogen cooled cryostat. The cryostat was originally an unmodified Janis VPF-100, but this configuration had issues with a gradual drift in the laser pointing, and the cryostat reservoir only provided enough coolant to run for 1 h at a time. Because of these issues, significant modifications were made to the cryostat configuration.

To stabilize the laser pointing, a rigid armature was constructed, as shown in Fig. 2, and was mounted in place of one of the four cryostat windows. The copper sample mount was then disconnected from the cryostat cold plate, and held by the armature through compression of washers (outer diameter 0.25 in., inner diameter 0.115 in., thickness 0.115 in.) made of garolite (G10), a very low thermal conductivity material.<sup>39</sup> This was necessary to maintain reasonable thermal isolation between the cryostat outer shell and the copper submount. Thermal contact with the cold bath was achieved using a series of folded copper ribbons between the copper laser mount and the cold plate. The addition of an armature eliminated the drifting in the laser beam pointing, but because of the reduced cross-sectional area of the copper ribbons compared to the original mounting arrangement, the lowest achievable temperature with the laser operating is  $\sim 106$  K. This issue has been addressed before with a different type of flexible thermal connection.<sup>25</sup>

In addition to the armature, the VPF-100 internal body was exchanged for a Janis Supertran FHT-ST internal body, which accepts a transfer line allowing a continuous flow of

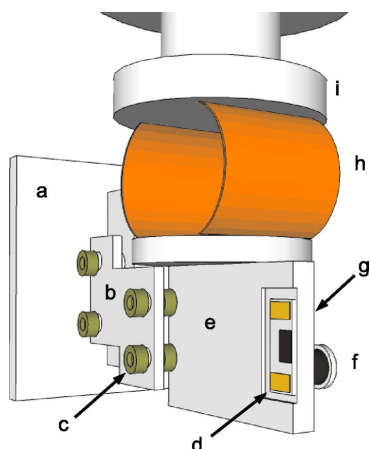


FIG. 2. (Color online) Schematic of rigid armature mount designed to eliminate laser drift as the cryostat liquid nitrogen level changed. (a) Back mounting plate; (b) armature; (c) G10 washer; (d) QCL chip; (e) copper laser mount; (f) resistive heater; (g) temperature diode (hidden from view, but adjacent to resistive heater on backside of mount); (h) copper ribbon; (i) cryostat cold plate.

liquid nitrogen to be delivered to cool the laser. This eliminated the need to refill a liquid nitrogen reservoir in hourly intervals. The liquid nitrogen is provided by an 80 L self-pressurizing liquid nitrogen Dewar (Cryofab CLPB 80-VW), which is capable of providing more than 40 h of laser run time between Dewar refills.

The laser current is provided by an ILX Lightwave (LDX-3232) power supply. To prevent inadvertent application of the wrong polarity of the applied current (which destroys the laser), a Zener diode has been added between the power supply and the laser. Additionally, the computer interface program has a high current limit that prevents a user from inadvertently applying dangerously high currents ( $>825$  mA) to the laser. Even if this fail-safe were compromised, a built-in hardware current limit has been set on the power supply.

A Lakeshore (Model 341S) temperature controller is used in conjunction with a silicon temperature diode and a resistive heater to stabilize the temperature of the copper mount holding the QCL. The positioning of the heater and temperature sensor are shown in Fig. 2. The silicon temperature diode is positioned on the bottom of the copper mount opposite the side where the QCL is mounted, and the resistive heater is positioned adjacent to the diode on the same side of the mount. The long-term temperature stability ( $\geq 1$  s) maintained using this configuration is  $\Delta T \sim \pm 0.005$  K, as estimated by the measured laser frequency jitter using the Bristol mid-IR wavemeter and the temperature-to-frequency relationship for the laser.

To protect against accidental laser operation at temperatures that would damage the laser ( $>160$  K), the laser current is routed through a relay in the temperature controller. The relay is programmed to close only after the cryostat temperature dips below 90 K, and to open if the laser temperature exceeds 160 K, thus preventing operation of the

laser when the liquid nitrogen has run out in the self-pressurizing Dewar.

Laser frequency tuning is carried out by manipulating both the laser current start point and the temperature of the submount. By increasing the laser core temperature, either by increasing the laser current or the temperature of the laser mount, the laser output is downshifted in frequency. From empirical observations the laser has a frequency-to-current conversion of  $\sim 8$   $\text{cm}^{-1}/\text{A}$ , and a frequency-to-temperature conversion of  $\sim 0.08$   $\text{cm}^{-1}/\text{K}$ .

Using a variety of temperature and current conditions, it is possible to tune the laser in regions between 1183 and 1201  $\text{cm}^{-1}$ . Complete coverage of the 18  $\text{cm}^{-1}$  frequency span is not achieved due to laser mode-hops. The position of the mode-hops and tuning regions where the laser is stable can vary after an optical alignment. In regions where the laser can scan, it is possible to cover up to  $\sim 1$   $\text{cm}^{-1}$  before a mode-hop.

The frequency output of the QCL depends strongly on the temperature of the submount (and therefore the laser) when the laser current is brought above threshold. By monitoring the frequency output of the QCL using a cw wavemeter (Bristol 621B), it is possible to map out these temperature regions, allowing one to reproducibly bring the laser above threshold at a desired output frequency. The conditions for adjusting the laser output around 1185  $\text{cm}^{-1}$  ( $\text{C}_{60}$ ) and 1197  $\text{cm}^{-1}$  ( $\text{CH}_2\text{Br}_2$ ) can be determined through trial and error for a given optical alignment.

## B. Optical layout

The divergent light output from the QCL passes through an antireflective (AR)-coated 3 in. diameter ZnSe window on the cryostat and is collimated by a 1 in. diameter AR-coated ZnSe aspheric lens ( $f=2.54$  cm). Light exiting the sphere is sent to a two element telescope comprised of a plano-convex  $\text{BaF}_2$  lens ( $f=50$  cm) and a biconvex  $\text{BaF}_2$  lens ( $f=6.35$  cm). This produces a small diameter beam that is then passed through an acousto-optic modulator (AOM). By careful alignment of the orientation of the AOM (Modulator Isomet 1207B with rf driver RFA241), and adjustment of the applied rf power, it is possible to attain a first order deflection efficiency approaching 85%. The first order beam is captured and gradually refocused using another plano-convex  $\text{BaF}_2$  lens ( $f=50$  cm), and used for ringdown spectroscopy; the zero order beam is used for reference measurements.

The QCL is extremely sensitive to optical feedback, leading to issues with both the frequency coverage and the amount of mode-hop free tuning coverage achieved. To get the laser to scan stably, two approaches were utilized. First, it was necessary to tilt all of the optical components in the beam path. Second, the first order beam was passed through a holographic wire grid polarizer (Thorlabs WP25H-B). During scanning the wire grid polarizer transmission axis was kept at  $20^\circ$ – $45^\circ$  with respect to the horizontal polarization of the laser beam, corresponding to losses of 10% to 50%. In this capacity the wire grid polarizer may have served as a variable attenuator, reducing the amount of power available

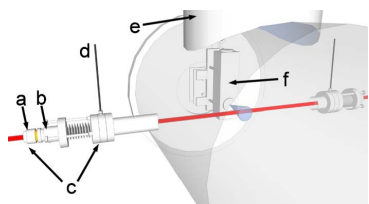


FIG. 3. (Color online) View of the chamber showing how the ringdown cavity axis is perpendicular to the expansion axis from the supersonic source. The vacuum chamber is rendered translucent in the figure. The laser beam is shown entering the mirror mount and crosses the free-jet (shown as a cone) emerging from the source. (a) Cavity ringdown mirror mount; (b) PZT; (c) kinematic mirror mount assembly; (d)  $N_2$  purge gas line; (e) roots blower; (f) supersonic expansion source.

to back-reflect off the input ringdown mirror high reflectivity coating. The combination of these approaches reduced back reflections to the point where  $\sim 1 \text{ cm}^{-1}$  mode-hop free scanning is possible. A prototype optical isolator was also tested, but the amount of absorption from the optical isolator medium for a given amount of optical rotation made this approach unsuitable.

After passing through the polarizer, the first-order beam is coupled into the high finesse cavity using a three lens mode-matching telescope mounted on a meter-long dove-tail optics rail. This telescope facilitates mode-matching to the  $TEM_{00}$  mode of the ringdown cavity, and consists of a plano-convex  $BaF_2$  ( $f_l=20 \text{ cm}$ ), a biconcave  $CaF_2$  ( $f_l=-7.6 \text{ cm}$ ), and a plano-convex  $BaF_2$  lens ( $f_l=50 \text{ cm}$ ).

The ringdown cavity is formed from two  $R(\lambda \sim 8.5 \mu\text{m}) > 0.9998$  mirrors (Laser Power Optics) with 6 m radius of curvature. The mirrors are held in homemade kinematic mounts with three precision screws to allow two-axis adjustment of their orientation. These mounts mate to Con-Flat half-nipples that have been welded to the stainless steel vacuum chamber. The ringdown cavity axis is perpendicular to the supersonic expansion axis, as shown in Fig. 3. Between the vacuum chamber housing the source and the ringdown mirrors there are Swagelok connections for flowing  $N_2$  purge gas at roughly 700 SCCM (SCCM denotes cubic centimeters per minute at STP) to protect the ringdown mirrors, and to bring the chamber up to ambient pressure without risk of particulates settling onto the mirror surfaces.

The ringdown mirror on the same side as the mode-matching telescope is mounted to a piezoelectric transducer (PZT) (Piezomechanik HPSt 150/20-15/25 VS-35) driven by a high voltage driver (Thorlabs MDT694A), with a sawtooth voltage waveform provided by a function generator. The voltage ramp applied to the PZT dithers the cavity resonances by more than one free spectral range to ensure that the laser frequency will come into resonance with the cavity at least twice during one PZT modulation cycle. Light leaking out of the cavity is focused by a short focal length plano-convex  $BaF_2$  lens ( $f_l=6.35 \text{ cm}$ ) onto a photoconductive mercury cadmium telluride detector (PC-MCT) (Infrared Associates MCT-9-1.0) with a 1 MHz preamplifier (Infrared Development Systems 1205). The noise equivalent power for the detector with the amplifier is  $1.85 \times 10^{-12} \text{ W}/\sqrt{\text{Hz}}$ . The

output from the MCT preamplifier is split to a high speed comparator and a 100 MHz 14-bit high speed digitizer card (National Instruments PCI-5122).

The reference arm of the optical layout relies on the zero order beam exiting the AOM. This beam is gradually re-focused using a long focal length (98.7 cm) plano-convex  $CaF_2$  lens. A ZnSe window is used as a beamsplitter, sending a small portion of the beam through a 45 cm long absorption cell, which is normally filled with  $SO_2$  or  $N_2O$ . Light exiting the absorption cell is focused by an off-axis parabolic mirror (Janos  $f_l=7.63 \text{ cm}$ ) onto a photovoltaic mercury zinc cadmium telluride detector (Vigo Technologies PVM-10.6) with a 1 MHz bandwidth preamplifier (VPDC-1S). The voltage output from the detector is connected to the input channel on a data acquisition board (National Instruments PCI-6221).

The remainder of the zero order beam is sent to a wavemeter. The QCL beam and the  $50 \mu\text{W}$  red tracer beam from the wavemeter are initially made collinear over 1 m to align the QCL beam into the wavemeter. In this process, the QCL beam is visualized by observing the scattered mid-IR light on irises using a thermal infrared imaging camera (FLIR ThermoCam 320EX). The wavemeter has a specified accuracy of  $0.001 \text{ cm}^{-1}$  if it is properly aligned. However, good alignment produced a sufficient back reflection to promote laser mode-hops, and we therefore deliberately misalign the QCL beam such that the wavemeter reading is offset by  $\sim 200\text{--}300 \text{ MHz}$ . To account for this, we calibrate the wavemeter reading using absorption lines in the direct absorption cell. The wavemeter therefore serves only as a relative frequency measurement tool, but also provides a lower accuracy real-time measure of the QCL frequency as the laser current and temperature are actively adjusted. The difference between the frequency of the first and zero order beams due to the Bragg downshifting of the first order beam is 40 MHz, and is accounted for during the frequency calibration procedure.

### C. Data acquisition

During acquisition of a spectrum, the laser mount is held at a fixed temperature, while the current is stepped in small user-defined increments. The PZT is constantly dithered, bringing the ringdown cavity periodically in resonance with the laser, a scheme originally employed by Ref. 40. At each laser current, a number of ringdown transients are acquired and fit to exponential decays. Finally, direct absorption and wavemeter data are then acquired for frequency calibration. After the calibration data are collected, the laser current is then stepped. The data acquisition process is controlled by a personal computer (PC) running homemade LabWindows code, a comparator, and an AOM control circuit, as explained in more detail below.

The collection of each ringdown event begins when the cavity comes into resonance with the laser frequency, due to sweeping of the PZT, and the voltage output of the PC-MCT sharply increases. When this voltage reaches a user-defined threshold, the comparator sends out a transistor transistor logic (TTL) high pulse to the trigger input of the high speed

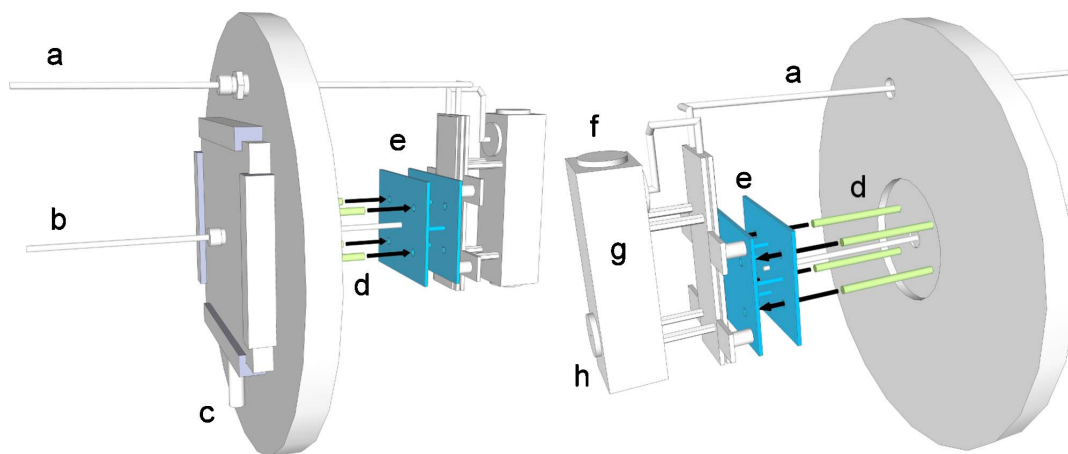


FIG. 4. (Color online) Two perspectives of the supersonic source mounted on a translatable plate attached to the back flange of the vacuum chamber. (a) Gas feedline to expansion source; (b) push-rod for adjusting nozzle distance from cavity axis; (c) height adjustment micrometer for the translatable plate; (d) rods for supporting source carriage; (e) source carriage plates; (f) Conflat blank used to seal source bore; (g) expansion source body; (h) pinhole nozzle machined into Conflat blank.

digitizer, and a TTL low pulse is sent to the AOM control circuit. The latter pulse triggers the AOM control circuit to output a TTL low pulse to the AOM rf driver, which removes the rf power from the AOM, suppressing the first order beam by  $-38$  dB. The duration of this TTL low signal is a user set value on the comparator, and is adjusted so that one complete ringdown event can be collected without being spoiled by subsequent injection of light into the cavity. While the light going into the cavity is being attenuated, the TTL high pulse initiates data collection by the high speed digitizer. The decay event is fit in a data acquisition program using a fast algorithm that accommodates a nonzero baseline on the exponential decay.<sup>41</sup> Once the output time of the comparator TTL low signal has elapsed, the first order beam is turned on again, allowing the process of ringdown collection at a fixed laser current to continue.

Once the user defined number of ringdowns (typically 100) has been collected, a box-and-whiskers algorithm is used to remove the top and bottom quartile of the measured time constants. The remaining time constant values are then averaged, converted to an absorption coefficient, and recorded. The PC then sends a TTL high signal to the AOM control circuit, which overrides the signal sent from the comparator, and turns the AOM off for sufficient time to acquire calibration data. The intensity of light on the PC-MZCT detector (after passing through the direct absorption cell) is measured by the digital acquisition board, and the wavemeter is read through a universal serial bus interface. Also at this time, the laser current and temperature are read through a general purpose interface bus (GPIB) interface and recorded. Once the calibration data have been obtained, the LabWindows program uses the GPIB interface to step the laser current by a user-defined amount (typically 0.1 mA, which corresponds to  $\sim 23$  MHz), and the data collection process starts again. This cycle continues until the laser current reaches the end of the desired scan range.

#### D. Supersonic expansion source and sample introduction

Figure 4 shows an overall view of the supersonic expansion source and its mounting in the vacuum chamber. The supersonic expansion source is composed of a stainless steel body with an attached pair of plates. The gas exits the oven body through a nozzle machined into a 1 1/3 in. ConFlat blank, which fits to a ConFlat “flange” machined into the source body (item h Fig. 4). This design makes it possible to test a variety of nozzle geometries by machining 1 1/3 in. ConFlat blanks.

For the current methylene bromide jet studies a 700  $\mu\text{m}$  pinhole nozzle was used. Slit nozzles were also available but not used. The slit nozzle would provide a reduction in linewidth in comparison to a pinhole nozzle,<sup>42,43</sup> and would provide a higher signal-to-noise (S/N) ratio for the transitions observed, but this increase is limited by the 30 MHz ( $0.001\text{ cm}^{-1}$ ) linewidth of the laser. When carrying out  $\text{C}_{60}$  spectroscopy a slit nozzle geometry may be preferable because it affords better vibrational cooling due to an increase in the number of collisions early in the expansion, but this will come at the expense of an increased rotational temperature in comparison to a pinhole nozzle.<sup>44</sup> For flexibility it is preferable to have both nozzle types when the instrument will be used for  $\text{C}_{60}$  spectroscopy.

The source body is mounted to a carriage with two plates held in parallel (item e in Fig. 4). The parallel plates have four through-holes that line up with four rods extending from a  $x$ - $y$  translatable flange on the back of the vacuum chamber (item d in Fig. 4). A rod is attached to the carriage and exits the chamber through an Ultra-Torr connection on the back flange (item b in Fig. 4); this allows the entire source assembly to be translated perpendicular to the ringdown cavity axis, thereby controlling the distance from the nozzle where the expansion is probed spectroscopically. The  $x$ - $y$  translat-

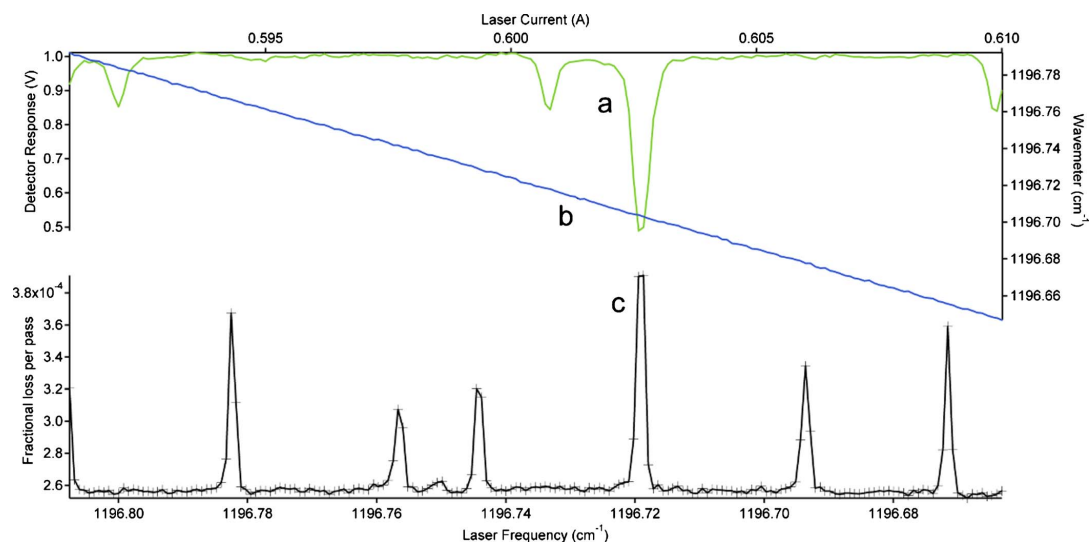


FIG. 5. (Color online) Example  $\text{CH}_2\text{Br}_2$  scanning window of room temperature gas leaked into the chamber from 1196.792–1196.647  $\text{cm}^{-1}$ . (a) Direct absorption scan (normalized) of  $\text{SO}_2$ . (b) Frequency readings from calibrated wavemeter. (c) Cavity ringdown spectrum of  $\text{CH}_2\text{Br}_2$ .

able flange allows adjustment of the vertical offset between the expansion and the cavity axis through the adjustment of a micrometer (item c in Fig. 4) that pushes against the translatable flange.

The supersonic source is backed by gas delivered from a mixing manifold constructed from four mass flow controllers (MKS M100B and 247D). One of the flow controllers is backed by Ar (S.J. Smith 99.95% purity) that is bubbled through methylene bromide (Aldrich 99% purity), while a second flow controller is backed with only Ar. The mole fraction of methylene bromide seeded in the expansion can then be adjusted by adjusting these two flow controllers.

While the mixing manifold and bubbler are useful for the introduction of methylene bromide to the source, the  $\text{C}_{60}$  sample introduction will be carried out differently. The  $\text{C}_{60}$  sample can be loaded directly into the hollow source bore (covered by the conflat blank labeled f in Fig. 4), which is accessible via another 1 1/3 in. ConFlat. The solid sample can be loaded in pellets that are held in place by sitting on top of a plug of quartz wool, separating the sample from the region of the bore just before the nozzle exit.

The extreme source temperatures when attempting  $\text{C}_{60}$  spectroscopy make it impractical to implement a pulsed supersonic expansion source. The large gas load generated by operating the source continuously is handled by a two-stage pumping system composed of a roots blower (Oerlikon-Leybold WS2001) and a rotary vane pump (Oerlikon-Leybold SV630). During normal flow conditions, with  $\sim 1$  atm pressure measured after the flow controllers, and  $\text{N}_2$  curtain gas flowing over the ringdown mirrors, the typical chamber background pressure is  $\sim 20$ – $40$  mTorr ( $\sim 700$  SCCM  $\text{N}_2$  flow rate).

### III. RESULTS AND DISCUSSION

#### A. Ringdown spectrometer performance

The performance of the spectrometer and the supersonic expansion source (operated at room temperature) have been evaluated using the  $\nu_8$  band of methylene bromide. Methylene bromide was selected as a test molecule because it has a vibrational band falling within the frequency coverage of our QCL. Several other molecules were considered, but methylene bromide has the advantages of being small (only five atoms), being commercially available, and whose mass is dominated by two heavy atoms making it a near prolate top with small rotational constants. The latter characteristics combine to make the rovibrational structure of the band simple, but also compact, so that it is not necessary to scan over a broad spectral window in order to estimate the rotational temperature in the expansion.

Figure 5 provides an example of one scanning window covering 0.15  $\text{cm}^{-1}$  of the  $\text{CH}_2\text{Br}_2$  vibrational band. This spectrum is not of a jet-cooled sample. The methylene bromide in this scan was leaked into the chamber through an open 0.25 in. inner diameter tube. Using the calibration traces, the maximum full width at half maximum (FWHM) of the spectral features seen in trace (c) is estimated to be 0.0013  $\text{cm}^{-1}$  (40 MHz). Assuming a 30 MHz instrument linewidth, the estimated linewidth for the transition is  $\sim 30$  MHz, which compares favorably with the 0.0011  $\text{cm}^{-1}$  (33 MHz) FWHM Doppler broadening for a single methylene bromide line at room temperature. Between the spectral features the baseline standard deviation in the absorption coefficient is  $\sim 1.4 \times 10^{-8} \text{ cm}^{-1}$ , and represents the typical noise level of the system. Many spectra covering short frequency spans have been collected providing coverage from 1195.4 to 1197.15  $\text{cm}^{-1}$ .

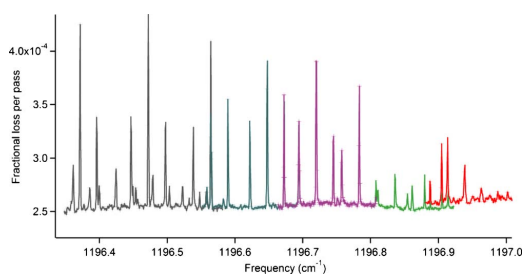


FIG. 6. (Color online) Collection of calibrated overlapped  $\text{CH}_2\text{Br}_2$  spectra from 1196.5 to 1197.0  $\text{cm}^{-1}$  illustrating the prominence of the strong Q-branch features from all three isotopologues. All these spectra are of room temperature gas that has been leaked into the chamber.

This is the first time that the  $\nu_8$  band of methylene bromide has been observed with sufficient resolution to reveal the rotational structure; previous spectra in the literature were acquired at low resolution, showing only the band contours of the P, Q, and R branches.<sup>45,46</sup> In order to evaluate the rotational cooling in the expansion, it was necessary to assign the high resolution spectrum of the jet-cooled sample.

Methylene bromide is a near-prolate asymmetric top with a Ray's asymmetry parameter of  $\approx -0.996$ .<sup>47</sup> The  $\text{CH}_2$  wagging motion of the  $\nu_8$  band results in a change of the dipole moment predominantly along the molecular  $a$ -axis, giving a parallel band structure. This leads to an easily assignable band structure, but the high abundance of two bromine isotopes provides an additional complication. The natural abundance of the  $^{79}\text{Br}$  and  $^{81}\text{Br}$  isotopes is roughly 1:1, and with the presence of two bromine atoms in methylene bromide a 1:2:1 abundance of  $\text{CH}_2^{79}\text{Br}_2$ ,  $\text{CH}_2^{79}\text{Br}^{81}\text{Br}$ , and  $\text{CH}_2^{81}\text{Br}_2$  isotopologues is expected in the sample. Each isotopologue will have its own parallel band, with small differences in the vibrational band center positions and rotational constants.

The detailed assignment was carried out using PGOPHER, a spectral assignment and fitting software package.<sup>48</sup> Ground state rotational constants from microwave spectroscopy of the  $\text{CH}_2^{79}\text{Br}_2$ ,<sup>49</sup>  $\text{CH}_2^{81}\text{Br}_2$ ,<sup>49</sup> and  $\text{CH}_2^{79}\text{Br}^{81}\text{Br}$  (Ref. 50) isotopologues were used for both the ground and vibrational excited states for the initial spectral prediction.

The first set of assignments involved a progression of strong sharp spectral features seen in the spectrum of room temperature methylene bromide leaked into the chamber, as shown in Fig. 6. These features represent a series of Q-branch progressions for all three of the isotopologues. A single feature is composed of a series of tightly packed unresolved transitions sharing the same upper and lower  $K_a$  values. Because the features are narrow and not resolvable, each Q-branch feature is assigned to a single  $(\nu'=1, J'=K_a'', K_a'=K_a'', K_c'=1) \leftarrow (\nu''=0, J''=K_a'', K_a''=K_a'', K_c''=0)$  transition. In the figure, a rough 1:2:1 intensity ratio can be seen because of the isotope abundance, with the strongest features in the sequence belonging to the  $\text{CH}_2^{79}\text{Br}^{81}\text{Br}$  isotopologue. It is important to note that not all of the spectral windows displayed in the figure were carried out with the same mole fraction of methylene bromide, so the intensities between

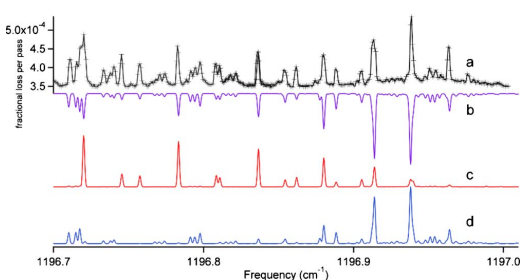


FIG. 7. (Color online) Comparison between recorded experimental spectra of  $\text{CH}_2\text{Br}_2$  and simulated spectra with all three isotopologues at two different rotational temperatures. (a) Experimental spectra from 1196.50 to 1197.00  $\text{cm}^{-1}$  with the nozzle 2.5 cm from the region probed, with the flow rates of the Ar only and Ar/ $\text{CH}_2\text{Br}_2$  set to 660 and 102 SCCM, respectively; (b) simulated spectrum composed of a linearly scaled coaddition from simulations (c) and (d); (c) simulated spectrum at  $T_{\text{rot}}=7$  K with a Gaussian linewidth of 0.0015  $\text{cm}^{-1}$ ; (d) simulated spectrum at  $T_{\text{rot}}=300$  K with a Gaussian linewidth of 0.0015  $\text{cm}^{-1}$ .

different scanning windows cannot be directly compared.

Using these initial assignments of the Q-branches for  $\text{CH}_2^{79}\text{Br}^{81}\text{Br}$ , the experimental spectrum was fit, allowing only the band origin  $\nu_0$  and the excited state rotational constant  $A'$  to vary, with all other rotational constants constrained to values determined through pure rotational microwave spectroscopy. The Q-branch pattern resulting from fitting to these  $\text{CH}_2^{79}\text{Br}^{81}\text{Br}$  assignments was then shifted higher in frequency to match the Q-branch progression for  $\text{CH}_2^{79}\text{Br}_2$ , and lower in frequency to assign the heavier  $\text{CH}_2^{81}\text{Br}_2$  isotopologue. Comparison of simulations generated from fitting of the Q-branch features to the experimental spectra then enabled assignment of low  $J''$  P-branch lines seen in the jet-cooled spectra as shown in Fig. 7.

The final results of the assignment and fitting are presented in Table I. The largest average  $|\text{observed}-\text{calculated}|$  (Avg.  $|\text{o}-\text{c}|$ ) achieved for fitting to Q and P-branch transitions was 0.000 45  $\text{cm}^{-1}$  (14 MHz). Given that the spectral features are under-sampled, that the spectra were acquired taking 0.000 77  $\text{cm}^{-1}$  (23 MHz) frequency steps, and that only six parameters were used to fit 62 transitions, we consider this average o-c to be acceptable.

While the line frequencies of the simulations clearly match those of the experimental spectra, the simulated relative intensities (assuming a single rotational temperature) fail to match the experimental spectra acquired in the free-jet. Figure 7 highlights this by presenting two simulated spectra at  $T_{\text{rot}}$  of 300 and 7 K, traces (c) and (d), respectively. Neither simulation is a good match to the experimental spectra shown in trace (a). However, trace (b), which is a scaled linear combination of traces (c) and (d), compares better to the relative intensities of the experimental spectrum.

These results indicate that the observed spectrum is due to a combination of room temperature and rotationally cooled  $\text{CH}_2\text{Br}_2$ . Close to the band center, the Q-branch features corresponding to low  $K_a$  are dominated by the jet-cooled sample, while the room temperature contribution is negligible. Farther from the band origin (higher values of  $K_a$ ), the intensity of the Q-branch features are dominated by

TABLE I. Compilation of spectroscopic constants obtained by fitting experimental spectra for all three isotopologues using PGOPHER. Only  $\nu_0$  and  $A'$  were fit, with the  $1\sigma$  uncertainties from the fit provided in parentheses next to the value.  $A''$  is taken from microwave studies, and shown for comparison to  $A'$ . The rightmost columns provide the average observed minus calculated for the fit, and the number of assigned lines for each isotopologue, respectively. The B and C rotational constants for all three isotopologues are not provided in the table because they were constrained to their values from microwave studies.

	Band constants ( $\text{cm}^{-1}$ )			Avg.  o-c  ( $\text{cm}^{-1}$ )	# Assg. Lines
	$\nu_0$	$A''$	$A'$		
$\text{CH}_2$ $^{79}\text{Br}_2$	1196.983 63(99)	0.868 311	0.863 451 9(22)	0.000 35	20
$\text{CH}_2$ $^{79}\text{Br}^{81}\text{Br}$	1196.957 97(12)	0.867 519	0.862 664 9(28)	0.000 45	22
$\text{CH}_2$ $^{81}\text{Br}_2$	1196.932 06(12)	0.866 756	0.861 910 8(23)	0.000 44	20

the room temperature background gas. The strength of the contribution from the background is not surprising because a majority of the 75 cm path length probed is chamber background gas, while the jet comprises a much smaller amount of the pathlength.

Near the band center, the relative intensities of the Q-branch features ( $K_a \leq 2$ ) and the low-J P-branch transitions are best described by a simulation with  $T_{\text{rot}} = 7$  K. This illustrates the effectiveness of the expansion source for producing rotationally cold molecules, at least when operated at room temperature. The strength of the Q-branch features near the band center also serves as a feedback signal to optimize alignment overlap between the pinhole expansion source and the ringdown cavity axis.

The FWHM of the jet-cooled methylene bromide features is estimated to be  $\sim 50$ – $60$  MHz. The estimated FWHM is broader than transitions associated with the room temperature background sample. The linewidth discrepancy between the jet and background features agrees with past studies in Ar free-jets in the mid-IR, showing that the Doppler broadening associated with the expansion is greater than the room temperature Doppler broadening.<sup>51–56</sup> Our observed jet-cooled linewidth is comparable to, but narrower than, that seen in those previous studies.<sup>51–56</sup>

## B. Comparison to previous QCL ringdown spectrometers

Two previous cw cavity ringdown spectrometers have been reported using QCLs.<sup>26,27</sup> Table II compares their single-shot standard deviations in the time constant and absorption coefficient with ours. In the two previous studies these single-shot values were determined in an empty cavity while holding the laser at a fixed frequency. The single-shot information for the current study is estimated from the mea-

sured standard deviation in the absorption coefficient ( $\sigma_\alpha$ ) in collected room temperature methylene bromide spectra where there are no measurable spectral features, and from the average ringdown collection rate and time constant. Close investigation of the baseline regions used did not reveal periodic fringing, as seen in the CRD study by Kosterev *et al.*<sup>27</sup> Because the ringdown spectra are the result of using the box-and-whiskers algorithm, the unfiltered noise level is likely worse than estimated. The  $\sigma_\alpha$  was calculated using the following formula<sup>27</sup>

$$\sigma_\alpha = \frac{\sigma_\tau}{c\langle\tau\rangle}, \quad (1)$$

where  $\langle\tau\rangle$  is the average time constant, and  $\sigma_\tau$  is the standard deviation of the time constant.

With a knowledge of the  $\sigma_\alpha$ , and the ringdown repetition rate ( $f_{\text{rep}}$ ), it is possible to calculate the instrumental sensitivity ( $S_y$ ) using the following expression:<sup>57</sup>

$$S_y = \frac{\sigma_\alpha}{\sqrt{f_{\text{rep}}}}. \quad (2)$$

The  $S_y$  of the current study is significantly higher than the prior studies. The high  $S_y$  is related to the poor performance of our PC-MCT detector. While recording ringdown events it was necessary to start the exponential fit  $\sim 14$   $\mu\text{s}$  after receiving the TTL high trigger because of the long response time of the PC-MCT. This wait reduces the S/N in the portion of the decay that can be fit to a single exponential, leading to an increase in  $\sigma_\tau$ . The comparator level also had to be set to a high voltage threshold in a trade-off between recording ringdown events with a significantly high S/N to

TABLE II. Comparison of the performance of previously reported QCL cw ringdown spectrometers with that of the current instrument.

	$\langle\tau\rangle$ ( $\mu\text{s}$ )	$\sigma_\tau/\langle\tau\rangle$	$\sigma_\alpha$ ( $\text{cm}^{-1}$ )	$f_{\text{rep}}$ transients (Hz)	$S_y$ ( $\text{cm}^{-1} \text{Hz}^{-1/2}$ )
Paldus <i>et al.</i> (Ref. 26)	0.949	$2 \times 10^{-3}$	$7.2 \times 10^{-8}$	600	$2.98 \times 10^{-9}$
Kosterev <i>et al.</i> (Ref. 27)	3.48	$2.2 \times 10^{-3}$	$2.2 \times 10^{-8}$	1600	$5.50 \times 10^{-10}$
This work	$\sim 10$	$\sim 4.7 \times 10^{-2}$	$1.58 \times 10^{-7}$	10	$5.06 \times 10^{-8}$

improve the  $\sigma_r$  at the cost of a reduced ringdown collection rate, further impacting the instrumental sensitivity.

The manufacturer indicated that the rise time for the PC-MCT detector should be from 1 to 2  $\mu\text{s}$ , which is in stark contrast to what was seen experimentally. This performance issue could in principle be due to saturation from the large amount of power directed at the detector, to issues with the AOM response, or due to a flaw with the detector itself. The power reaching the PC-MCT was reduced by two orders of magnitude, and no improvement was seen in the response of the detector to a single ringdown event. The AOM response was explored by triggering the AOM while looking at both the reference detector and PC-MCT response. The reference detector responded in 1  $\mu\text{s}$  to the switching off of the AOM, while the PC-MCT took nearly 10  $\mu\text{s}$  to decay to the background level.

Given these results, a PV-MCT from Kolmar Technologies (KMPV11-1-J1/AC) with a postamplifier (KA100-E2) was recently purchased as a replacement detector. This PV-MCT eliminated the long trigger delay issue, making it possible to fit after a 2.5 ms delay. Preliminary tests in an empty cavity have provided a  $\sigma_r/\langle\tau\rangle \leq 1 \times 10^{-2}$ , and a ringdown collection rate  $\approx 50$  Hz. The current noise level achieved with the detector does not appear limited by the  $-38$  dB on/off modulation ratio of the AOM, but this effect is known to cause an increase in the noise level of a cw-CRD spectrometer.<sup>58</sup>

#### IV. CONCLUSIONS

The first high-resolution spectrum of the  $\nu_8$  band of methylene bromide has been collected using a quantum cascade laser based cw cavity ringdown spectrometer, coupled to a supersonic expansion source. To our knowledge, this represents the first time that a cw ringdown QCL spectrometer has been coupled with a supersonic free-jet for the purposes of spectral discovery. The high resolution of the spectrometer has allowed the assignment and fitting of the rovibrational bands for each isotopologue, which in turn has demonstrated the effectiveness of our supersonic expansion source for producing rotationally cold molecules. The methylene bromide spectrum can now be used as a tool to optimize the overlap between the supersonic expansion and the ringdown cavity when the oven is operating at room temperature.

#### ACKNOWLEDGMENTS

The authors wish to thank Richard Saykally for the loan of the cryostat and the cavity ringdown mirrors used in this work, and Frank Tittel for helpful conversations regarding the frequency stability of QCLs. We also wish to acknowledge experimental assistance from Brian Siller, Brian Pohrte, and Brett McGuire. The Illinois team acknowledges financial support from NASA Laboratory Astrophysics Grant No. NNG05GE59G, the Camille and Henry Dreyfus Foundation, the David and Lucile Packard Foundation, and the University of Illinois. The Princeton team has been supported by funding from the Mid-Infrared Technologies for Health and the Environment NSF Engineering Research Center.

- <sup>1</sup>T. R. Geballe and T. Oka, *Nature (London)* **384**, 334 (1996).
- <sup>2</sup>J. H. Lacy, N. J. Evans, J. M. Achtermann, D. E. Bruce, J. F. Arens, and J. S. Carr, *Astrophys. J.* **342**, L43 (1989).
- <sup>3</sup>J. H. Lacy, J. S. Carr, N. J. Evans, F. Baas, J. M. Achtermann, and J. F. Arens, *Astrophys. J.* **376**, 556 (1991).
- <sup>4</sup>J. Cernicharo, A. M. Heras, A. G. G. M. Tielens, J. R. Pardo, F. Herpin, M. Guelin, and L. B. F. M. Waters, *Astrophys. J. Lett.* **546**, L123 (2001).
- <sup>5</sup>H. Kroto, J. Heath, S. O'Brien, R. Curl, and R. Smalley, *Nature (London)* **318**, 162 (1985).
- <sup>6</sup>A. Godard, *C. R. Phys.* **8**, 1100 (2007).
- <sup>7</sup>F. Capasso, C. Gmachl, D. L. Sivco, and A. Y. Cho, *Phys. Today* **55**(5), 34 (2002).
- <sup>8</sup>W. Tam, I. Leonov, and Y. Xu, *Rev. Sci. Instrum.* **77**, 063117 (2006).
- <sup>9</sup>D. Weidmann, L. Joly, V. Parpillon, D. Courtois, Y. Bonetti, T. Aellen, M. Beck, J. Faist, and D. Hofstetter, *Opt. Lett.* **28**, 704 (2003).
- <sup>10</sup>R. M. Williams, J. F. Kelly, J. S. Hartman, S. W. Sharpe, M. S. Taubman, J. L. Hall, F. Capasso, C. Gmachl, D. L. Sivco, J. N. Baillargeon, and A. Y. Cho, *Opt. Lett.* **24**, 1844 (1999).
- <sup>11</sup>G. Wysocki, R. Lewicki, R. F. Curl, F. K. Tittel, L. Diehl, F. Capasso, M. Troccoli, G. Hofler, D. Bour, S. Corzine, R. Maulini, M. Giovannini, and J. Faist, *Appl. Phys. B: Lasers Opt.* **92**, 305 (2008).
- <sup>12</sup>B. G. Lee, M. A. Belkin, R. Audet, J. MacArthur, L. Diehl, C. Pflugl, F. Capasso, D. C. Oakley, D. Chapman, A. Napoleone, D. Bour, S. Corzine, G. Höfler, and J. Faist, *Appl. Phys. Lett.* **91**, 231101 (2007).
- <sup>13</sup>B. Lee, H. Zhang, C. Pflugl, L. Diehl, M. Belkin, M. Fischer, A. Wittmann, J. Faist, and F. Capasso, *IEEE Photonics Technol. Lett.* **21**, 914 (2009).
- <sup>14</sup>W. Weber, J. Remillard, R. Chase, J. Richert, F. Capasso, C. Gmachl, A. Hutchinson, D. Sivco, J. Baillargeon, and A. Cho, *Appl. Spectrosc.* **56**, 706 (2002).
- <sup>15</sup>A. Castrillo, E. De Tommasi, L. Gianfrani, L. Sirigu, and J. Faist, *Opt. Lett.* **31**, 3040 (2006).
- <sup>16</sup>B. W. M. Moeskops, S. M. Cristescu, and F. J. M. Harren, *Opt. Lett.* **31**, 823 (2006).
- <sup>17</sup>G. Hancock, J. H. van Helden, R. Peverall, G. A. D. Ritchie, and R. J. Walker, *Appl. Phys. Lett.* **94**, 201110 (2009).
- <sup>18</sup>S. Borri, S. Bartalini, P. De Natale, M. Inguscio, C. Gmachl, F. Capasso, D. L. Sivco, and A. Y. Cho, *Appl. Phys. B: Lasers Opt.* **85**, 223 (2006).
- <sup>19</sup>J. Remillard, D. Uy, W. Weber, F. Capasso, C. Gmachl, A. Hutchinson, D. Sivco, J. Baillargeon, and A. Cho, *Opt. Express* **7**, 243 (2000).
- <sup>20</sup>N. Mukherjee and C. K. N. Patel, *Chem. Phys. Lett.* **462**, 10 (2008).
- <sup>21</sup>Y. Bakhrkin, A. Kosterev, C. Roller, R. Curl, and F. Tittel, *Appl. Opt.* **43**, 2257 (2004).
- <sup>22</sup>Y. Bakhrkin, A. Kosterev, R. Curl, F. Tittel, D. Yarekha, L. Hvozdar, M. Giovannini, and J. Faist, *Appl. Phys. B: Lasers Opt.* **82**, 149 (2006).
- <sup>23</sup>M. R. McCurdy, Y. A. Bakhrkin, and F. K. Tittel, *Appl. Phys. B: Lasers Opt.* **85**, 445 (2006).
- <sup>24</sup>M. R. McCurdy, Y. Bakhrkin, G. Wysocki, and F. K. Tittel, *J. Biomed. Opt.* **12**, 034034 (2007).
- <sup>25</sup>Y. Xu, X. Liu, Z. Su, R. M. Kulkarni, W. S. Tam, C. Kang, I. Leonov, and L. D'Agostino, *Proc. SPIE* **7222**, 722208 (2009).
- <sup>26</sup>B. Paldus, C. Harb, T. Spence, R. Zare, C. Gmachl, F. Capasso, D. Sivco, J. Baillargeon, A. Hutchinson, and A. Cho, *Opt. Lett.* **25**, 666 (2000).
- <sup>27</sup>A. A. Kosterev, A. L. Malinovsky, F. K. Tittel, C. Gmachl, F. Capasso, D. L. Sivco, J. N. Baillargeon, A. L. Hutchinson, and A. Y. Cho, *Appl. Opt.* **40**, 5522 (2001).
- <sup>28</sup>M. S. Taubman, T. L. Myers, B. D. Cannon, and R. M. Williams, *Spectrochim. Acta, Part A* **60**, 3457 (2004).
- <sup>29</sup>J. F. Kelly, A. Maki, T. A. Blake, and R. L. Sams, *J. Mol. Spectrosc.* **252**, 81 (2008).
- <sup>30</sup>A. Amirav, U. Even, and J. Jortner, *Chem. Phys.* **51**, 31 (1980).
- <sup>31</sup>A. Amirav, U. Even, and J. Jortner, *Chem. Phys. Lett.* **83**, 1 (1981).
- <sup>32</sup>J. R. Cable, M. J. Tubergen, and D. H. Levy, *J. Am. Chem. Soc.* **109**, 6198 (1987).
- <sup>33</sup>N. A. van Dantzig, P. Piotrowiak, and D. H. Levy, *Chem. Phys. Lett.* **223**, 127 (1994).
- <sup>34</sup>J. W. Elam and D. H. Levy, *J. Phys. Chem. B* **102**, 8113 (1998).
- <sup>35</sup>L. C. Snoek, T. V. Mourik, and J. P. Simons, *Mol. Phys.* **101**, 1239 (2003).
- <sup>36</sup>M. Hippler and M. Quack, *Chem. Phys. Lett.* **314**, 273 (1999).
- <sup>37</sup>J. Thiébaud and C. Fittschen, *Appl. Phys. B: Lasers Opt.* **85**, 383 (2006).
- <sup>38</sup>Z. Liu, D. Wasserman, S. Howard, A. Hoffman, C. Gmachl, X. Wang, T. Tannun-Ek, L. Cheng, and F.-S. Choa, *IEEE Photonics Technol. Lett.* **18**, 1347 (2006).

## Appendix C

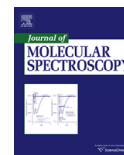
# High-resolution spectroscopy of the $\nu_8$ band of methylene bromide using a quantum cascade laser

This appendix is reprinted in its entirety with permission from B. E. Brumfield, J. T. Stewart, and B. J. McCall, *Journal of Molecular Spectroscopy*, 266, 57 (2011). Copyright 2011, Elsevier Inc.



Contents lists available at ScienceDirect

## Journal of Molecular Spectroscopy

journal homepage: [www.elsevier.com/locate/jms](http://www.elsevier.com/locate/jms)

## High-resolution spectroscopy of the $\nu_8$ band of methylene bromide using a quantum cascade laser

Brian E. Brumfield<sup>a</sup>, Jacob T. Stewart<sup>a</sup>, Benjamin J. McCall<sup>b,\*</sup>

<sup>a</sup> Department of Chemistry, University of Illinois, 600 South Mathews Avenue, Urbana, IL 61801, USA

<sup>b</sup> Departments of Chemistry and Astronomy, University of Illinois, Urbana, IL 61801, USA

### ARTICLE INFO

#### Article history:

Received 28 December 2010

In revised form 12 February 2011

#### Keywords:

Methylene bromide  
Quantum cascade laser  
Fresnel rhomb

### ABSTRACT

A continuous wave cavity ringdown spectrometer with a Fabry-Perot quantum cascade laser has been used to collect a rotationally-resolved infrared spectrum of the  $\nu_8$  vibrational band of methylene bromide in a slit nozzle expansion. In our laboratory, previous observations of the vibrational band were limited by spectral coverage to only the P and Q-branches and by the 24 MHz step-size of the laser [1]. The issue of limited spectral coverage has been resolved using a Fresnel rhomb and a wire grid polarizer to protect the laser from the destabilizing effects of back-reflection from the ringdown cavity. The frequency step-size of the spectrometer has been reduced from 24 MHz to 2 MHz. With both of these instrument enhancements, we have been able to record the R-branch of the vibrational band, and can resolve many lines that were previously blended in spectra acquired using a pinhole expansion nozzle. Significant hyperfine splitting was observed for the low- $J$  transitions in the P and R-branches. It was possible to neglect the effects of hyperfine splitting for transitions involving  $J' > 2$  in the spectral assignment, and simulations using the constants obtained by fitting to Watson's S-reduced Hamiltonian for  $\text{CH}_2^{79}\text{Br}^{81}\text{Br}$ , and the A-reduced form for  $\text{CH}_2^{79}\text{Br}_2$  and  $\text{CH}_2^{81}\text{Br}_2$ , provide a good match to experimental spectra. A total of 297 transitions have been assigned for all three isotopologues, with a standard deviation of  $0.00024 \text{ cm}^{-1}$  ( $\sim 7 \text{ MHz}$ ).

© 2011 Elsevier Inc. All rights reserved.

### 1. Introduction

High-resolution gas-phase spectroscopy in the mid-infrared (mid-IR) is useful for studying the fundamental vibrational modes of molecules and molecular clusters. Lead salt diode lasers have been used to collect high-resolution gas-phase spectra of large molecules [2–6] and clusters [7–9] in supersonic expansions. Further development of lead salt diode laser spectrometers is stymied by their limited frequency coverage, low output powers, poor beam quality, and cryogenic operation.

By comparison, quantum cascade lasers (QCLs) offer several significant advantages over lead salt diode lasers. The narrow laser linewidths ( $<30 \text{ MHz}$ ), good beam quality, and high cw output powers ( $\sim 1\text{--}100 \text{ mW}$ ) make quantum cascade lasers desirable for sensitive, high-resolution spectroscopy applications. The issue of narrow frequency coverage ( $\sim 20 \text{ cm}^{-1}$ ) can be overcome by using an external cavity system [10–12]. Though there is a wealth of literature leveraging the development of QCL spectrometers towards trace gas sensing applications [13], there have been far fewer studies incorporating QCL spectrometers with supersonic expansions [1,14–16].

\* Corresponding author.

E-mail address: [bjmccall@illinois.edu](mailto:bjmccall@illinois.edu) (B.J. McCall).

We are developing a continuous wave cavity ringdown (cw-CRD) spectrometer to acquire a rotationally-resolved, cold, gas-phase spectrum of a vibrational band of buckminsterfullerene ( $\text{C}_{60}$ ) around  $8.5 \mu\text{m}$ . In previously published work we used a supersonic expansion of methylene bromide ( $\text{CH}_2\text{Br}_2$ ) seeded in argon to test the sensitivity and resolution of our QCL-based cw-CRD spectrometer [1]. During this testing several problems negatively influenced the sensitivity and resolution of the instrument. The photoconductive mercury-cadmium-telluride (PC-MCT) detector was found to have a slower response time than quoted by the manufacturer. This impaired the fitting of the ringdown decays, leading to a higher than expected noise level. Optical feedback from light rejected by the cavity induced mode-hops during scanning, and may have played a role in reducing the sensitivity of the instrument [17]. A limitation on the current step-size output by the laser power supply led to an undersampling of the methylene bromide lines.

Recently we have been able to modify the instrument to address the concerns mentioned above. To resolve the detector response time issues experienced in the previous study, we have replaced the PC-MCT detector with a photovoltaic mercury-cadmium-telluride (PV-MCT) detector. The influence of optical back-reflection has been mitigated with the addition of a Fresnel rhomb-based optical isolator. We have also decreased the current step-size of

our laser power supply, allowing us to sample methylene bromide transitions with several points per line. With our improved spectrometer, we have re-visited our earlier work on the  $\nu_8$  vibrational band of methylene bromide with better sensitivity and resolution. The following work highlights the improved instrument performance, and presents a more detailed analysis of the  $\nu_8$  vibrational band of methylene bromide for all three isotopologues.

## 2. Experimental

The experimental layout in this paper is similar to that presented in Brumfield et al. [1] with some modifications detailed below. We use a Fabry-Perot QCL provided by our collaborators at Princeton University.

An ILX Lightwave (LDX-3232) power supply is used to source current to the QCL. Previously, the laser current was controlled through a custom LabWindows program that communicated with the power supply over a GPIB interface. Communication over the GPIB limited the current step-size to 0.1 mA, corresponding to a frequency step-size of  $\sim 24$  MHz. This limitation was overcome by using the external modulation input of the power supply. At the start of a scan the laser is brought to an initial current using the GPIB interface. A voltage output from a data acquisition (DAQ) board, which can be scanned from 0 to a maximum of 10 V, is fed into a homemade 30:1 voltage divider before entering the external modulation input. The voltage divider is used to reduce the electrical noise coupled into the cable between the DAQ board output and the power supply modulation input. During spectral acquisition the current is stepped by increasing the applied voltage to the modulation input. Using this method methylene bromide spectra were acquired with  $\sim 2$  MHz frequency steps.

Infrared light exiting the QCL is collimated by a series of lenses and then passed through a Ge acousto-optic modulator (AOM). The zero order beam is sent to the reference arm of the experiment, which is comprised of a wavemeter and a 40 cm absorption cell filled with  $\sim 4$  Torr of  $\text{SO}_2$ . The zero order beam is passed through the absorption cell in a triple-pass configuration to achieve a higher  $S/N$  on the  $\text{SO}_2$  absorption features.

After sample ringdown collection, the computer sends a signal to turn off the AOM. The duration of this delay depends on whether or not a wavemeter reading will be acquired with the direct absorption cell data. For recording a frequency reading with the wavemeter, it was found that delaying 7 s after turning off the AOM provided a stable reading. This long delay is due to the limited time response of an auto-gain circuit in the wavemeter. To save time during data acquisition the wavemeter is only used every 10–50 data points. After reference data is collected the applied modulation input voltage is stepped and the process is repeated.

The first order beam passes through a wire grid polarizer (ThorLabs WP25H-B) and a ZnSe quarter wave rhomb (II-VI Infrared FRZ-8.4-.55-90-90RM). The polarizer is set to pass the horizontal polarization of the laser light. Light exiting the polarizer then passes through the quarter wave rhomb and exits as circularly polarized light. Any light that is reflected by the input ringdown mirror has the handedness of its circular polarization reversed, and upon transmission back through the rhomb is converted into vertically polarized light. The vertically polarized light is then attenuated by the  $\sim 400:1$  extinction coefficient of the wire grid polarizer. This provides a potential maximum optical isolation of  $\sim 25$  dB against optical back-reflection, but the achieved experimental isolation was likely less than this due to alignment errors and the actual retardation provided by the rhomb. Experimentally, the rhomb has provided sufficient protection against optical back-reflection to reduce the number of mode-hops experienced during

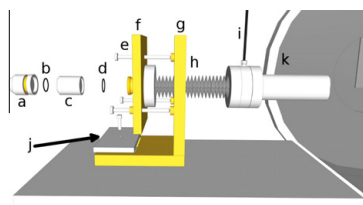


**Fig. 1.** Diagram showing a close-up of one of the new ringdown mounts used to form our cavity: (a) ringdown mirror in two piece aluminum holder, o-ring seal made between mirror HR surface and rightmost piece of the mirror holder, (b) o-ring for making a vacuum seal between ringdown mirror holder and piezoelectric transducer, (c) piezoelectric transducer, (d) o-ring for making a seal between the piezoelectric transducer and kinematic portion of brass mount, (e) knob adjustment screws, (f) brass kinematic plate, (g) stationary portion of brass mount, (h) metal bellows with  $2 \frac{3}{4}$ " conflat connections to the kinematic brass plate and the CF assembly connected to the half-nipple welded directly to the vacuum chamber, (i) purge gas line, (j) aluminum compression plate to secure stationary part of brass mount, (k) welded CF half-nipple extending from vacuum chamber.

scanning. A similar optical isolation scheme has been used with a lead salt diode laser heterodyne spectrometer [18].

After passing through the Fresnel rhomb the laser light is coupled into the  $\sim 85$  cm long ringdown cavity (FSR  $\sim 176$  MHz) using a three lens telescope. We recently acquired two new high reflectivity mirrors (Los Gatos 901-0010-8300) with 1 m radii of curvature to form our high finesse cavity. The planar side of the mirrors have an  $8\text{--}12 \mu\text{m}$  broadband AR coating. New mirror mounts (shown in Fig. 1) were designed to minimize the impact of anisotropic thermal expansion of the vacuum chamber when it is under a heat load from our high-temperature oven expansion source. Each ringdown mirror is held in a two piece holder machined from aluminum. Direct contact between the piece of the aluminum holder pressed against the AR side of the mirror is cushioned by a teflon gasket. A vacuum seal is maintained on the HR side of the mirror by an o-ring seated in a groove on the second piece of the aluminum holder. This o-ring seal is not shown in Fig. 1. The mirror holder then threads onto the end of a piezoelectric transducer (PZT). A vacuum seal is formed by an o-ring (b) compressed between (a) and (c). The PZT threads onto the end of the brass kinematic plate (f). The brass kinematic plate has an o-ring groove machined onto the end, forming a vacuum seal between (c) and (f). The opposite side of the kinematic plate has a machined knife edge to create a Conflat (CF) seal with the long bellows (h). The mirror is aligned by using knob adjustment screws (e). The springs providing the restoring force holding the kinematic plate to the stationary part of the brass holder are not shown in Fig. 1. The stationary portion of the holder (g) is secured to the optics breadboard platform by compression using an aluminum plate with a through-hole for a  $\frac{1}{4}$ "-20 screw. This made it possible to compress a sorbathane sheet between (g) and the breadboard platform. A 4" long bellows (h) provides a flexible connection that maintains the vacuum between the ringdown mirror and the chamber by  $2 \frac{3}{4}$ " Conflat connections. The mirrors are protected from chamber dust by using the purge gas lines (i). The other ringdown mirror mount is the same as that shown in Fig. 1, but does not have the PZT (c) or o-ring (b).

We create a supersonic expansion from a  $12 \text{ mm} \times 150 \mu\text{m} \times 7 \text{ mm}$  (length  $\times$  width  $\times$  channel depth) slit that has been machined into a  $1 \frac{1}{8}$ " conflat blank. In the previous study we used an  $800 \mu\text{m}$  pinhole nozzle [1]. The backing pressure for the expansion is provided by two flow controllers, one that is fed by argon that has passed through a bubbler with methylene bromide (Aldrich 99% purity), and another drawing straight from an argon cylinder (S.J. Smith 99.95% purity). Gas exiting the flow controllers

is split to a continuous dump provided by a Welch pump and to a solenoid valve. The solenoid valve (Parker Hannifin 9S1-A1-P1-9B07) controls the flow of gas to the supersonic expansion source. When the valve is open data is taken with the jet and sample present. When the valve is closed a background spectrum is taken in the absence of the jet and sample. The delay for data acquisition between open and closed states of the valve was 2 s, and is controlled by the computer. The data was collected this way so fringing that was normally present during data collection could be subtracted. As a result of this collection process, scanning proceeded slowly at a rate of  $\sim 0.05 \text{ cm}^{-1}$  per hour. The frequency drift of the QCL is  $< 0.006 \text{ cm}^{-1}$  after the laser has been on for an hour. This slow temperature drift is likely due to the temperature equilibration of the laser and cryostat mount. An example of the fringe subtraction is shown in Fig. 2.

The period and amplitude of the fringing is sensitive to the optical alignment. The frequency of the fringing falls between 400 and 600 MHz. The amplitude of the fringing varied between  $\sim 10^{-5}$  and  $10^{-6}$  fractional loss per pass. All the lenses and infrared detectors in the experiment have been tilted to try to minimize etalon effects.

We have implemented a new homemade driver for the piezoelectric transducer using an audio amplifier (Samson Servo 300). Our new driver can sweep the cavity over one free spectral range at a repetition frequency greater than 250 Hz, which is a significant improvement over our previous driver's performance ( $< 80 \text{ Hz}$ ). The ringdown collection rate varied between 50 and 200 ringdowns/s, and was dependent on the quality of the cavity alignment and the comparator trigger level setting.

Light leaking out of the cavity is focused onto a PV-MCT detector (Kolmar Technologies KMPV11-1-J1/AC). The signal from the PV-MCT is post-amplified (Kolmar Technologies KA100-E2/AC) by a factor of 20 V/V, and sent into a homemade comparator triggering circuit and a 14-bit high speed digitizer to be recorded for later processing.

When a cavity build-up event meets the comparator threshold, the comparator sends a signal to trigger the high-speed digitizer to record data. Simultaneously the computer sends out a signal to turn off the AOM so light is not being coupled into the cavity while the ringdown decay is being collected. Two sets of 100 ringdowns per point are collected per modulation voltage step because of the sample and background subtraction from the supersonic jet.

### 3. Results and discussion

The  $\nu_8$  band of methylene bromide was acquired from 1196.14 to 1197.92  $\text{cm}^{-1}$ . Fig. 3 shows the experimental data collected over

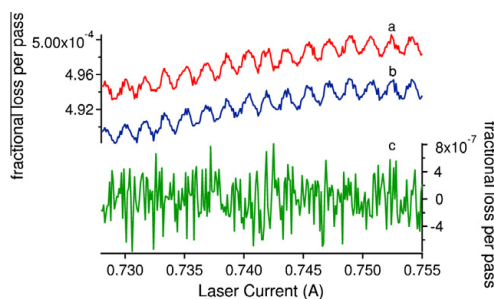


**Fig. 2.** Ringdown spectra of fractional loss per pass versus laser current illustrating effectiveness of background subtraction to remove fringing. There was no sample present in the expansion during this scan. Traces (a) and (b) are recorded with the jet on and off respectively. Trace (a) is offset to ease comparison with Trace (b). Trace (c) is the subtracted result from Traces (a) and (b).

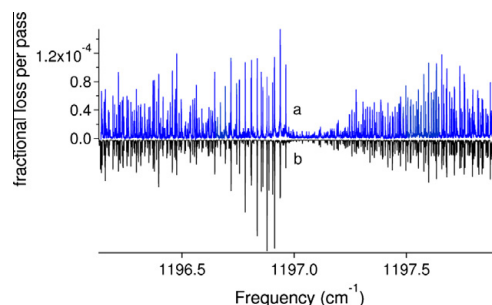


**Fig. 3.** Trace (a) is the experimental spectrum. Trace (b) is a simulated spectrum resulting from the assignment and fitting of the vibrational band. Trace (b) is composed of two co-added simulations created using PGOPHER [19]. One is a simulation with  $T_{rot} = 20 \text{ K}$  and linewidths of  $0.00045 \text{ cm}^{-1}$  for jet-cooled methylene bromide. The second simulation is for the residual background sample contribution with  $T_{rot} = 300 \text{ K}$  and linewidths of  $0.0011 \text{ cm}^{-1}$ . The 300 K simulation is scaled by a factor of 1.5 with respect to the 20 K simulation in the co-addition.

this range plotted with our simulation of the band. The total frequency coverage of the vibrational band was  $1.78 \text{ cm}^{-1}$ . Previously we covered  $1.75 \text{ cm}^{-1}$  of the methylene bromide band using a pin-hole nozzle [1]. This prior coverage only spanned the Q and P-branches of the vibrational band because it was not possible to get reliable mode-hop free spectral coverage beyond  $1197 \text{ cm}^{-1}$  due to back-reflection induced instability. By using the Fresnel rhomb optical isolator we were able to center our spectral coverage over the band center and record portions of both the P and R-branches.

To properly simulate our experimental data, it was necessary to include a room temperature contribution because residual methylene bromide was present in the vacuum chamber. This residual sample is present because the solenoid pulse open duration is on the order of a second. It should be noted that Trace (a) in Fig. 3 is composed of many spectra spanning  $0.08\text{--}0.34 \text{ cm}^{-1}$  that were independently calibrated; Fig. 4 provides an example of one of these spectra.

The distance from the slit nozzle to the cavity axis was  $\sim 6 \text{ mm}$  for all scans. For all scanning windows a flow rate of 75 sccm of Ar bubbled through methylene bromide and 1500 sccm of pure Ar were used. With these flow rates, when the solenoid valve was open the pressure in our vacuum chamber would rise to 70–90 mTorr.

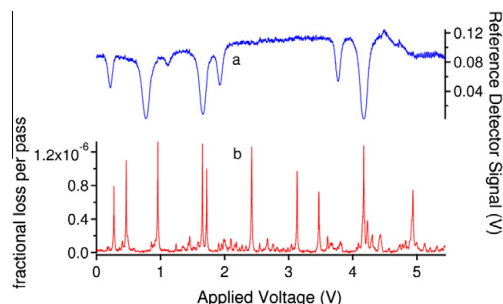


**Fig. 4.** Trace (a) is the signal from the direct absorption cell filled with  $\text{SO}_2$  used for absolute frequency calibration. Trace (b) is the fringe subtracted cavity ringdown spectrum of a portion of the methylene bromide Q-branch. Both traces are plotted against the voltage applied to the modulation input on the laser power supply.

To calibrate our spectra, we utilized the wavemeter for relative frequency calibration, and SO<sub>2</sub> lines for absolute frequency calibration. Wavemeter data were fit to a 4th order polynomial, which was used to convert the voltage applied to the modulation input into a frequency scale. The SO<sub>2</sub> reference scan was then plotted against the wavemeter frequency scale. Each of the reference lines was fit to a Gaussian profile. From the Gaussian fitting a line center position calibrated to the wavemeter frequency is obtained. Because the wavemeter is intentionally misaligned, to reduce back-reflections to the QCL, there exists a frequency offset between the true frequency and that provided by the wavemeter. This offset was generally found to be between 100 and 300 MHz, and was dependent on the wavemeter alignment. To determine this offset, the difference between the wavemeter calibrated frequency and the HITRAN2008 [20] transition frequency is calculated for all the observed reference lines. All these offset values are averaged, and the resulting average is added to the wavemeter calibration, generating an absolute frequency scale for the methylene bromide spectra. The 40 MHz Bragg downshift of the AOM is also accounted for in the calibration procedure.

Overlap between individual spectra after calibration is usually good, with a difference <15 MHz. In the worst cases, the difference can be as large as 30 MHz; this is possibly limited by the uncertainty and systematic errors that exist for the SO<sub>2</sub> reference data in HITRAN2008 [20]. In the HITRAN2008 database, the listed uncertainty in the line positions is in the range of 3–30 MHz. In addition to these issues, some of the residuals resulting from fitting the wavemeter traces provide evidence of periodic drifting in the laser frequency less than or equal to 24 MHz. Such drifts could be explained by gradual changes in the laser temperature <0.01 K. The laser temperature control loop is not capable of correcting for such small temperature changes.

Previous work we carried out on the  $\nu_8$  band of methylene bromide was done using a pinhole nozzle expansion source [1]. Using a slit nozzle in this study provided narrower linewidths at the expense of a warmer rotational temperature. In our previous work the linewidth was around 45 MHz (0.0015 cm<sup>-1</sup>), and many of the closely spaced methylene bromide lines for the three isotopologues were blended and not assignable. The narrowest transitions seen in the current work are 13.5 MHz (0.00045 cm<sup>-1</sup>), which has allowed us to assign many more transitions. Assignment of the  $\nu_8$  band was initially guided by our previous assignment [1], which was refined using the new spectra. The band was then simulated using PGOPHER [19]. Methylene bromide is a near prolate top with a ground state  $\kappa \sim -0.996$ , and fitting was done to the A-reduced form of the asymmetric top Hamiltonian for CH<sub>2</sub><sup>79</sup>Br<sub>2</sub> and CH<sub>2</sub><sup>81</sup>Br<sub>2</sub>, while the S-reduced form was used for CH<sub>2</sub><sup>79</sup>Br<sup>81</sup>Br. The choice of reduction was based on the availability of the ground state constants provided in microwave spectroscopy studies of methylene bromide [21,22]. The  $I'$  representation was used for all three isotopologues. Nuclear spin statistical weights of 9:7:7:9 ( $J_{ee}; J_{eo}; J_{oe}; J_{oo}$ ) were included for the CH<sub>2</sub><sup>79</sup>Br<sub>2</sub> and CH<sub>2</sub><sup>81</sup>Br<sub>2</sub> isotopologues. The CH<sub>2</sub><sup>79</sup>Br<sup>81</sup>Br isotopologue lacks nuclear spin statistics because of its lower symmetry. Because of the nearly equal abundance of <sup>79</sup>Br and <sup>81</sup>Br, a 1:2:1 abundance of CH<sub>2</sub><sup>79</sup>Br<sub>2</sub>:CH<sub>2</sub><sup>79</sup>Br<sup>81</sup>Br:CH<sub>2</sub><sup>81</sup>Br<sub>2</sub> exists in the sample. This ratio was accounted for in the simulation. Only the excited vibrational state constants  $\nu_0$ ,  $A'$ ,  $B'$ ,  $C'$ , and  $D'_K(\Delta'_K)$  were allowed to float during the fitting process, while the ground state constants were fixed to their values determined through microwave spectroscopy [21,22]. For CH<sub>2</sub><sup>79</sup>Br<sup>81</sup>Br, the value of  $D'_K$  is not known, so instead the value of  $\Delta D_K = D'_K - D''_K$  was determined in the fitting process. The results of fitting the excited state spectroscopic constants are shown for CH<sub>2</sub><sup>79</sup>Br<sup>81</sup>Br in Table 1, and for CH<sub>2</sub><sup>79</sup>Br<sub>2</sub> and CH<sub>2</sub><sup>81</sup>Br<sub>2</sub> in Table 2. The list for the assigned transitions is provided in the Supplementary material for this article.

**Table 1**

Listing of spectroscopic constants for the  $\nu_8$  vibrational band of CH<sub>2</sub><sup>79</sup>Br<sup>81</sup>Br obtained by fitting to Watson's S-reduced form of the asymmetric top Hamiltonian [23]. Spectroscopic constants determined in this work are presented for each isotopologue under the "Current" column. Results of fitting from Brumfield et al. [1] are listed under the "Previous" column. The rotational constants fixed in the ground state are provided under the "Microwave" column. The units for the spectroscopic constants and the standard deviation are in wavenumbers (cm<sup>-1</sup>). The 1 $\sigma$  uncertainties resulting from the fit are provided in parentheses at the end of each value.

	CH <sub>2</sub> <sup>79</sup> Br <sup>81</sup> Br		
	$\nu_8=1$		$\nu_8=0$
	Previous [1]	Current	Microwave <sup>a</sup> [22]
$\nu_0$	1196.95797(12)	1196.957052(37)	
$A$	0.8626649(28)	0.8626518(25)	0.86751916(86)
$B$		0.0408228(16)	0.040804716(73)
$C$		0.0392382(14)	0.039253679(87)
$\Delta D_K^b$		$-2.17(22) \times 10^{-7}$	
$D_J^c$			$7.75(25) \times 10^{-9}$
$D_{JK}^c$			$-3.81(16) \times 10^{-7}$
$d_1^c$			$-6.44(90) \times 10^{-10}$
$d_2^c$			$-1.03(1.03) \times 10^{-9}$
# Assigned transitions	22	123	
Standard deviation	0.00044	0.00023	

<sup>a</sup> Rotational constants provided from microwave spectroscopy are for the ground state.

<sup>b</sup>  $\Delta D_K = D'_K - D''_K$

<sup>c</sup> Parameter in upper state fixed to values determined from microwave spectroscopy on ground state.

The standard deviation presented in the table is defined as [19]:

$$\text{standard deviation} = \sqrt{\frac{\sum_i^{n_{\text{obs}}} (\text{obs}_i - \text{calc}_i)^2}{n_{\text{obs}} - n_{\text{para}}}} \quad (1)$$

where the total number of assigned transitions is  $n_{\text{obs}}$ ,  $\text{obs}_i$  is the observed frequency position for the  $i$ th assigned transition,  $\text{calc}_i$  is the calculated frequency position for the  $i$ th transition, and  $n_{\text{para}}$  is the number of parameters floated in the least squares fitting of the spectroscopic data. The standard deviation values for the pinhole expansion work were also presented in Brumfield et al. [1], but they were mislabeled as the average  $|\text{obs} - \text{calc}|$ .

To evaluate the relative accuracy of the frequency calibration for the infrared spectra, a combination differences analysis was carried out using the infrared spectral assignments for the CH<sub>2</sub><sup>79</sup>Br<sup>81</sup>Br isotopologue. The residuals between the 27 combination differences from the infrared data and ground state data simulated using the rotational constants from Niide et al. [22] were obtained. The standard deviation for the combination differences residuals is 0.00037 cm<sup>-1</sup>, with a mean of  $3.4 \times 10^{-5}$  cm<sup>-1</sup>. The resulting standard deviation is within a factor of 2 of the standard deviation results from the fit, and may be larger because of the smaller sample size of the combination differences in comparison to the number of assigned lines in the fit.

The increase in the number of assignments for P and R-branch transitions compared to the previous work allowed for additional excited state parameters to be fit. The failure of the current values of  $\nu_0$  to agree within their listed fit uncertainties between both studies is likely due to the use of HITRAN2004 [24] SO<sub>2</sub> line positions in the previous paper. A majority of the HITRAN2008 SO<sub>2</sub> line positions from 1197.00 to 1196.70 cm<sup>-1</sup> are red-shifted by 20–30 MHz with respect to the frequency positions listed in HITRAN2004. This also explains the systematic red-shift in  $\nu_0$  compared to the values from the previous study. The addition of  $D'_K$  for CH<sub>2</sub><sup>79</sup>Br<sub>2</sub> and CH<sub>2</sub><sup>81</sup>Br<sub>2</sub> ( $\Delta D_K$  for CH<sub>2</sub><sup>79</sup>Br<sup>81</sup>Br) as a floated parameter for fitting the newest data is the reason why the values of  $A'$

**Table 2**

Listing of spectroscopic constants for the  $\nu_8$  vibrational band of  $\text{CH}_2^{79}\text{Br}_2$  and  $\text{CH}_2^{81}\text{Br}_2$  obtained by fitting to Watson's A-reduced form of the asymmetric top Hamiltonian [23]. Spectroscopic constants determined in this work are presented for each isotopologue under the "Current" column.

	$\text{CH}_2^{79}\text{Br}_2$			$\text{CH}_2^{81}\text{Br}_2$		
	$\nu_8=1$	$\nu_8=0$	$\nu_8=0$	$\nu_8=1$	$\nu_8=0$	$\nu_8=0$
	Previous [1]	Current	Microwave <sup>a</sup> [21]	Previous [1]	Current	Microwave <sup>a</sup> [21]
$\nu_0$	1196.98363(99)	1196.982565(56)		1196.93206(12)	1196.931350(46)	
$A$	0.8634519(22)	0.8634374(31)	0.868441(13)	0.8619108(23)	0.8618897(32)	0.86675642(56)
$B$		0.0413299(24)	0.041313137(47)		0.0403157(14)	0.040297341(27)
$C$		0.0397103(22)	0.039725549(53)		0.0387663(13)	0.038782329(30)
$A_K$		$1.2676(22) \times 10^{-5}$	$1.2922 \times 10^{-5c}$		$1.2667(33) \times 10^{-5}$	$1.2879(15) \times 10^{-5}$
$A_J^b$			$7.9321 \times 10^{-9c}$			$7.5662(40) \times 10^{-9}$
$A_{JK}^b$			$-3.8403(70) \times 10^{-7}$			$-3.7483(20) \times 10^{-7}$
$\delta_J^b$			$5.2279(63) \times 10^{-10}$			$4.8773(70) \times 10^{-10}$
$\delta_K^b$			$3.93 \times 10^{-8c}$			$3.782(50) \times 10^{-8}$
# Assigned transitions	20	92		20	82	
Standard deviation	0.00035	0.00027		0.00044	0.00022	

<sup>a</sup> Rotational constants provided from microwave work are for the ground state.

<sup>b</sup> Parameter in upper state fixed to values determined from microwave spectroscopy on the ground state.

<sup>c</sup> This parameter was constrained in the microwave work and has no reported uncertainty.

between the two studies do not agree within their listed uncertainties.

We observed complex hyperfine splitting in the low- $J$  P and R-branch features due to the presence of the two bromine nuclei in the molecule (see Fig. 5). The presence of significant hyperfine splitting in methylene bromide was discussed in previous microwave work [25,26,22], and it was emphasized that the low- $J$  transitions present the most complex splitting [26]. Modeling of the complex hyperfine splitting is beyond the scope of this current work, and we did not assign the  $P(1)$ ,  $R(0)$ , or  $R(1)$  transitions.

However, at higher  $J$  the microwave work showed that the hyperfine splitting simplified to a triplet pattern, with the peak close to the center of where a transition would be expected without the influence of hyperfine splitting [25,26]. Fig. 6 shows the occurrence of triplet patterns in a section of the R-branch spectrum for all three isotopologues. Transitions assigned with this triplet pattern are marked in the linelist included as Supplementary material to this article. Here it is assumed that the structure seen in the transition is due to hyperfine splitting, and that the asymmetry splitting of the two overlapped transitions is not resolvable given the instrument resolution. Fewer, but similar patterns are found in spectra acquired in the P-branch. In some situations a P-branch transition is seen that is broader than would be expected given the experimental linewidth, and it is likely that this broadening is the result of unresolved hyperfine splitting.

Fig. 7 shows experimental spectra acquired farther from the band center. The simulation and the experimental spectrum are in good agreement despite neglecting hyperfine interactions.

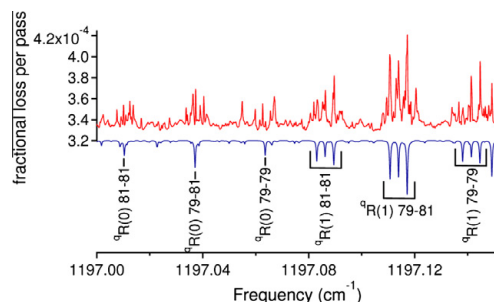


**Fig. 5.** The top trace is an experimental spectrum of the R-branch. The bottom trace is a section of the simulation shown in Fig. 3. The transitions in the simulation are labeled based on the isotopologue assuming no hyperfine splitting.

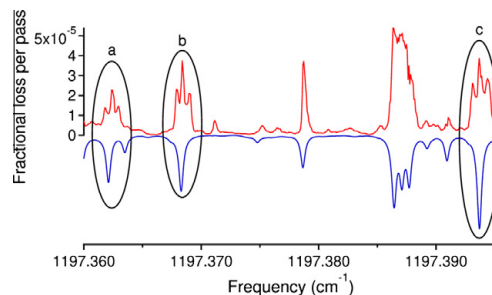


**Fig. 6.** The top trace is an experimental spectrum of the R-branch spanning 1197.360–1197.395  $\text{cm}^{-1}$ . The bottom trace is a section of the simulation shown in Fig. 3. The simulated transitions paired with the triplet patterns observed in the experimental spectrum are circled. The central peak of (a) has been assigned to  $^{81}\text{R}_{3,3}(5)$  and  $^{81}\text{R}_{3,2}(5)$  of  $\text{CH}_2^{81}\text{Br}_2$ . The central peak of (b) has been assigned to  $^{79}\text{R}_{2,2}(4)$  and  $^{79}\text{R}_{2,3}(4)$  of  $\text{CH}_2^{79}\text{Br}_2$ . The central peak of (c) has been assigned to  $^{81}\text{R}_{3,3}(5)$  and  $^{81}\text{R}_{3,2}(4)$  of  $\text{CH}_2^{79}\text{Br}_2$ .

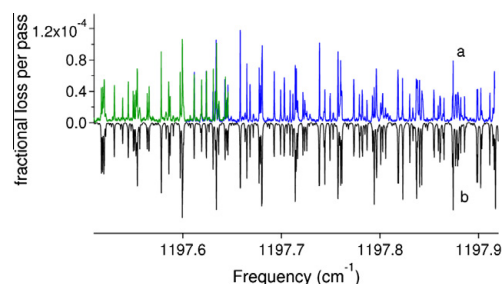


**Fig. 7.** Trace (a) shows two overlapped cavity ringdown spectra covering 1197.51–1197.92  $\text{cm}^{-1}$  in the R-branch. Trace (b) is a section of the simulation shown in Fig. 3.

#### 4. Conclusions

Recent improvements to our QCL cw-CRD spectrometer have led to an increase in the resolution and sensitivity of the instrument. As a result of these improvements, the  $\nu_8$  band of methylene

bromide was re-visited and previous spectral assignments were refined, while the total number of assignments was expanded from 62 to 297. The increase in resolution and spectral coverage revealed the presence of complex hyperfine splitting for the  $P(1)$ ,  $R(0)$ , and  $R(1)$  transitions that could not be assigned. Despite the absence of the low- $J$  assignments, fitting of the bulk of the vibrational band was carried out successfully with a standard deviation of  $0.00024\text{ cm}^{-1}$ . This study illustrates the suitability of QCL-based spectrometers for high-resolution mid-IR jet spectroscopy.

#### Acknowledgments

The authors wish to thank Matt Escarra and Professor Claire Gmachl from the Electrical Engineering Department at Princeton University for providing the quantum cascade lasers used in this work. Funding for this research was provided by a Packard Fellowship through the David and Lucile Packard Foundation. Jacob T. Stewart has been supported by a Robert C. and Carolyn J. Springborn Fellowship from the University of Illinois. The authors also wish to thank Professor Kevin Lehmann for suggesting the use of a Fresnel rhomb to build an optical isolator for the QCL spectrometer.

#### Appendix A. Supplementary data

Supplementary data associated with this article can be found, in the online version, at doi:10.1016/j.jms.2011.02.013.

Supplementary data for this article are available on ScienceDirect ([www.sciencedirect.com](http://www.sciencedirect.com)) and as part of the Ohio State University Molecular Spectroscopy Archives ([http://library.osu.edu/sites/msa/jmsa\\_hp.htm](http://library.osu.edu/sites/msa/jmsa_hp.htm)).

#### References

- [1] B.E. Brumfield, J.T. Stewart, S.L. Widicus Weaver, M.D. Escarra, S.S. Howard, C.F. Gmachl, B.J. McCall, *Rev. Sci. Instrum.* **81** (2010) 063102.
- [2] P. Asselin, P. Souillard, L. Manceron, V. Boudon, G. Pierre, *J. Mol. Spectrosc.* **517–518** (2000) 145–155.
- [3] G.M. Hansford, P.B. Davies, J. Gang, D.K. Russell, *Spectrochim. Acta Part A* **53** (1997) 1755–1759.
- [4] P.R. Brown, P.B. Davies, G.M. Hansford, N.A. Martin, *J. Mol. Spectrosc.* **158** (1993) 468–478.
- [5] P.B. Davies, G.M. Hansford, T.C. Killian, *J. Mol. Spectrosc.* **163** (1994) 138–158.
- [6] J. Gang, M. Pennington, D.K. Russell, F.J. Basterrechea, P.B. Davies, G.M. Hansford, *J. Opt. Soc. Am. B* **11** (1994) 184–190.
- [7] H. Qian, W.A. Herrebout, B.J. Howard, *Mol. Phys.* **91** (1997) 689–696.
- [8] M. Wangler, D. Roth, I. Pak, G. Winnewisser, P. Wormer, A. van der Avoird, *J. Mol. Spectrosc.* **222** (2003) 109–120.
- [9] G. Winnewisser, T. Drascher, T. Giesen, I. Pak, F. Schiilling, R. Schieder, *Spectrochim. Acta Part A* **55** (1999) 2121–2142.
- [10] B.G. Lee, M.A. Belkin, R. Audet, J. MacArthur, L. Diehl, C. Pflugl, F. Capasso, D.C. Oakley, D. Chapman, A. Napoleone, D. Bour, S. Corzine, G. Hoffer, J. Faist, *Appl. Phys. Lett.* **91** (2007) 231101–231103.
- [11] G. Wysocki, R. Lewicki, R. Curl, F. Tittel, L. Diehl, F. Capasso, M. Troccoli, G. Hoffer, D. Bour, S. Corzine, R. Maulini, M. Giovannini, J. Faist, *Appl. Phys. B: Lasers Opt.* **92** (2008) 305–311.
- [12] R. Maulini, I. Dunayevskiy, A. Lyakh, A. Tsekoun, C. Patel, L. Diehl, C. Pflugl, F. Capasso, *Electron. Lett.* **45** (2009) 107–108.
- [13] A. Kosterev, G. Wysocki, Y. Bakhrkin, S. So, R. Lewicki, M. Fraser, F. Tittel, R. Curl, *Appl. Phys. B: Lasers Opt.* **90** (2008) 165–176.
- [14] J.F. Kelly, A. Maki, T.A. Blake, R.L. Sams, *J. Mol. Spectrosc.* **252** (2008) 81–89.
- [15] Y. Xu, X. Liu, Z. Su, R.M. Kulkarni, W.S. Tam, C. Kang, I. Leonov, L. D'Agostino, *Proc. SPIE* **7222** (2009) 722208–722211.
- [16] J. Krieg, V. Lutter, F.X. Hardy, S. Schlemmer, T.F. Giesen, *J. Chem. Phys.* **132** (2010) 224306.
- [17] G.N. Rao, A. Karpf, *Appl. Opt.* **49** (2010) 4906–4914.
- [18] R. Schieder, *Infrared Phys. Technol.* **35** (1994) 477–486.
- [19] C.M. Western, P. Gopher, a program for simulating rotational structure, 2010. <<http://pgopher.chm.bris.ac.uk>>.
- [20] L. Rothman, I. Gordon, A. Barbe, D. Benner, P. Bernath, M. Birk, V. Boudon, L. Brown, A. Campargue, J.-P. Champion, K. Chance, L. Coudert, V. Dana, V. Devi, S. Fally, J. Flaud, R. Gamache, A. Goldman, I. Jacquemart, D. Kleiner, N. Lacombe, W. Lafferty, J. Mandin, S. Massie, S. Mikhailenko, C. Miller, N. Moazzen-Ahmadi, O. Naumenko, A. Nikitin, J. Orphal, V. Perevalov, A. Perrin, A. Predoi-Cross, C. Rinsland, M. Rotger, M. Šimečková, M. Smith, K. Sung, S. Tashkun, J. Tennyson, R. Toth, A. Vandaele, J. Vander Auwera, *J. Quant. Spectrosc. Radiat. Transfer* **110** (2009) 533–572.
- [21] R.W. Davis, M.C.L. Gerry, *J. Mol. Spectrosc.* **109** (1985) 269–282.
- [22] Y. Niide, H. Tanaka, I. Ohkoshi, *J. Mol. Spectrosc.* **139** (1990) 11–29.
- [23] J. Watson, *Vibrational Spectra and Structure*, vol. 6, Elsevier, 1977, pp. 2–89.
- [24] L. Rothman, D. Jacquemart, A. Barbe, D. Chris Benner, M. Birk, L. Brown, M. Carleer, C. Chackerian Jr., K. Chance, L. Coudert, V. Dana, V. Devi, J.-M. Flaud, R. Gamache, A. Goldman, J.-M. Hartmann, K. Jucks, A. Maki, J.-Y. Mandin, S. Massie, J. Orphal, A. Perrin, C. Rinsland, M. Smith, J. Tennyson, R. Tolchenov, R. Toth, J. Vander Auwera, P. Varanasi, G. Wagner, *J. Quant. Spectrosc. Radiat. Transfer* **96** (2005) 139–204.
- [25] D. Chadwick, D.J. Millen, *Trans. Faraday Soc.* **67** (1971) 1539–1550.
- [26] D. Chadwick, D.J. Millen, *Trans. Faraday Soc.* **67** (1971) 1551–1568.

## Appendix D

# Extending the limits of rotationally resolved absorption spectroscopy: Pyrene

This appendix is reprinted in its entirety with permission from B. E. Brumfield, J. T. Stewart, and B. J. McCall, *Journal of Physical Chemistry Letters*, 3, 1985 (2012). Copyright 2012, American Chemical Society.

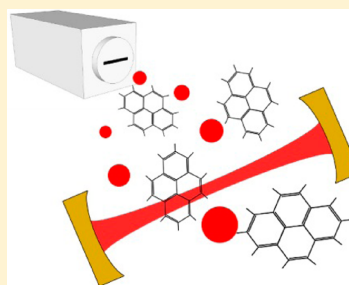
## Extending the Limits of Rotationally Resolved Absorption Spectroscopy: Pyrene

Brian E. Brumfield,<sup>†</sup> Jacob T. Stewart, and Benjamin J. McCall\*

Department of Chemistry, University of Illinois, Urbana, Illinois 61801, United States

### Supporting Information

**ABSTRACT:** We report the rotationally resolved gas phase spectrum of pyrene ( $C_{16}H_{10}$ ), which is now the largest molecule to be observed with rotational resolution using absorption spectroscopy. This represents a significant advance in the application of absorption spectroscopy to large carbon-containing molecules of fundamental chemical and astronomical importance. Such spectra will facilitate the search for large and highly symmetric molecules in interstellar space, where they may be abundant but cannot be detected without the support of high-resolution laboratory spectra. Detailed assignment and analysis of our spectrum indicates that pyrene is the most rigid rotor yet observed, and that a supersonic expansion cools both the rotational and vibrational temperatures of pyrene vapor produced in an oven source.



**SECTION:** Spectroscopy, Photochemistry, and Excited States

The field of astrochemistry seeks insight into the rich, diverse, and unique chemistry occurring in remote regions of the universe where environmental conditions differ radically from those encountered in a terrestrial laboratory. Understanding the possible chemical pathways that can lead from simple molecular precursors, such as acetylene, to large potentially prebiotic molecules in space is an important challenge in the field. To piece together this puzzle, it is necessary to identify molecules in space through observation of their unique absorption or emission features. The identity, temperature, and density of the surrounding chemical environment can be obtained from astronomical spectra, but only after molecules are identified with the aid of laboratory spectra. In particular, high-resolution gas phase molecular spectroscopy is an invaluable tool that can enable unequivocal detection of molecules in space. While many small (e.g.,  $H_2$ ,  $H_3^+$ , and  $CO$ )<sup>1–3</sup> and intermediate size molecules (e.g.,  $C_2H_2$ ,  $CH_4$ ,  $C_3$ , and  $C_6H_6$ )<sup>4–7</sup> have been detected in space and identified with the aid of laboratory spectra, there is a lack of high-resolution spectra of large potentially prebiotic molecules; this presents a significant challenge to identifying such molecules in space, and the field of high-resolution molecular spectroscopy must rise to this challenge. High-resolution studies of large molecules are also important from a fundamental chemical standpoint, as analysis of such spectra can provide insight into the structure and dynamics of large molecules.

A majority of astronomical observations of molecules are made using microwave or millimeter-wave spectroscopy of pure rotational transitions of molecules with permanent electric dipole moments. However, there are many large carbon containing molecules of potential prebiotic significance, such as linear carbon chains, symmetric fullerenes, and polycyclic

aromatic hydrocarbons (PAHs) that lack a permanent dipole moment and can only be observed by vibrational or electronic spectroscopy. Linear carbon chains have already been detected astronomically in space, and PAHs of extraterrestrial origin have been identified in meteorites.<sup>8</sup> However, acquiring high-resolution gas-phase spectra of large molecules using direct absorption spectroscopy is challenging because these molecules tend to have low vapor pressures at room temperature, and usually require direct heating or laser ablation techniques to put a sufficient number density of the sample into the gas phase.<sup>9–14</sup> The rotational and vibrational temperatures of these hot molecules can be cooled using the well-developed supersonic expansion technique. Large symmetric PAHs, such as pyrene ( $C_{16}H_{10}$ ) or coronene ( $C_{24}H_{12}$ ), present ideal challenges for pushing the limit of these experimental techniques and enabling new astronomical detections. Although laser-induced fluorescence (LIF) studies have shown the effectiveness of vibrational cooling of large organic molecules using pulsed sources,<sup>9,10,24</sup> there is little information about the degree of vibrational cooling achievable using a heated cw supersonic expansion source for absorption spectroscopy studies.

In this Letter, we present the rotationally resolved absorption spectrum of a C–H bending mode of pyrene, which is the largest molecule to be observed with rotational resolution by absorption spectroscopy. The necessity of good vibrational cooling in the supersonic expansion is also discussed, and an

Received: June 13, 2012

Accepted: July 11, 2012

Published: July 11, 2012

estimate for the vibrational temperature is presented. This work represents a significant step in high-resolution absorption spectroscopy of large carbon-containing and potentially prebiotic molecules.

Pyrene is a planar asymmetric rotor of  $D_{2h}$  point group symmetry, and the  $\nu_{68}$  vibrational mode studied here has  $B_{3u}$  symmetry and involves C–H bending in concert with an in-plane displacement of the two central carbon atoms in the fused-ring structure (see Figure 1). Low-resolution absorption

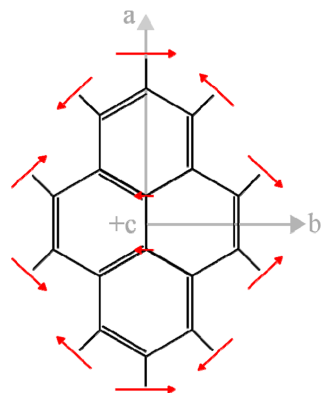


**Figure 1.** The structure and principal axes (a,b,c) of pyrene with arrows illustrating the displacement of the nuclei associated with the observed  $\nu_{68}$  C–H bending mode.

spectra of this C–H bending mode have been obtained<sup>15,16</sup> in rare gas matrices and in high-temperature gas phase samples. These data predict that the vibrational band center for the C–H bending mode will be near  $1184\text{ cm}^{-1}$  ( $8.44\text{ }\mu\text{m}$ ), and this is close to a widely observed astronomical feature at  $8.6\text{ }\mu\text{m}$ , part of the so-called unidentified infrared bands.<sup>17</sup> While the matrix and hot gas phase spectra of pyrene are helpful for guiding a high-resolution spectroscopic search, they are inadequate for definitive comparisons to high-resolution infrared astronomical spectra. The best mid-IR spectrographs are capable of  $0.01\text{ cm}^{-1}$  resolution in comparison to the  $1\text{ cm}^{-1}$  resolution of the

matrix and hot gas phase measurements. Additionally, the shift in the vibrational band center due to interactions with the rare-gas matrix can be on the order of several wavenumbers, and in the astronomical environment where spectral congestion can be high, such an uncertainty in the vibrational band center is unacceptable. The resolution of the current study is  $<0.001\text{ cm}^{-1}$ , providing more resolution than is necessary to meet the requirements for astronomical searches.

The  $\nu_{68}$  C–H bending mode was probed using a quantum cascade laser-based continuous-wave cavity ringdown spectrometer coupled to a heated supersonic expansion source that was operated continuously while collecting experimental spectra. Details regarding the spectrometer have been presented in two prior publications,<sup>18,19</sup> and details regarding the heated supersonic expansion source can be found in the Supporting Information. Briefly, argon gas was passed through a heated (420 K) oven containing pyrene, and the mixture was supersonically expanded through a slit nozzle. The expansion was overlapped with the ringdown cavity axis 6 mm downstream from the nozzle.

Through temperature and current tuning of the laser, it was possible to record the pyrene vibrational band from  $1182.77 - 1185.06\text{ cm}^{-1}$ , as displayed in Figure 2. Our spectra were calibrated to an accuracy of  $0.00049\text{ cm}^{-1}$  (15 MHz) using  $\text{SO}_2$  absorption line features and a wavemeter; further information on the calibration procedures is in the Supporting Information. The observed line width for transitions in the supersonic expansion was  $0.0004\text{ cm}^{-1}$  (12 MHz), which is sufficient to resolve the detailed rotational structure of the vibrational band.

To extract quantitative information on the structure of pyrene, we assigned the line center frequency positions for 694 observed lines (representing 2222 rotation–vibration transitions). The line center assignments were then used in a least-squares fitting optimization routine to a model asymmetric top Hamiltonian using PGOPHER.<sup>20</sup> Initially, we constrained the values of the ground state rotational constants to those obtained from a fluorescence excitation study of an electronic band of pyrene.<sup>21</sup> However, this failed to produce good agreement over the entire spectrum (see Supporting Information), so it was necessary to fit both ground and excited state rotational constants. The derived molecular constants are listed in Table 1, and the standard deviation of the residuals to the fit is only  $0.00053\text{ cm}^{-1}$  (16 MHz). The

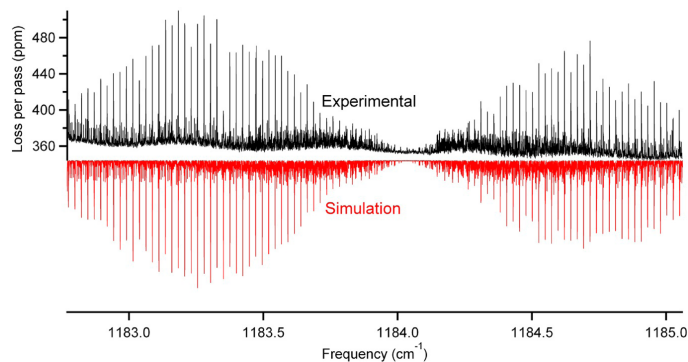


**Figure 2.** Cavity ringdown spectrum of the  $\nu_{68}$  band of pyrene (top trace, in black) in units of fractional loss per-pass (ppm) versus frequency ( $\text{cm}^{-1}$ ), compared with simulated spectrum (lower trace, in red).

**Table 1. Derived Molecular Constants (in  $\text{cm}^{-1}$ , with Uncertainties in Last Digits in Parentheses)**

	ground state	excited state	percent change
$\nu_0$		1184.035595(20)	
A	0.03372547(66)	0.03372116(67)	-0.0128(28)%
B	0.01855623(43)	0.01855635(43)	+0.0006(33)%
C	0.01197350(33)	0.01197172(34)	-0.0149(40)%

final simulation is in excellent agreement with the recorded spectrum, as seen for the entire band in Figure 2 and for a few select regions in Figure 3 (an expanded view of the entire spectrum is available in the Supporting Information).

One important result of this work is that the change in the rotational constants upon vibrational excitation is quite small: the relative changes for A, B, and C are -0.0128%, 0.0006%, and -0.0149%, respectively. The change in B is so small that it is not statistically significant, given the uncertainties in the fit. Molecules similar to pyrene, such as pyrazine and naphthalene, have been observed to have small changes in rotational constants when vibrationally excited,<sup>22</sup> but pyrene is remarkable in that all three constants change by less than 0.02% in the excited vibrational state. The rotational constant of adamantane, which has a more compact structure than pyrene but the same number of atoms, also exhibits larger changes in its rotational constant upon vibrational excitation.<sup>23</sup>

Another exceptional aspect of this result is that no centrifugal distortion constants were required to fit the spectrum. In a trial fit, we added a  $D_K$  constant, but the standard deviation only decreased by  $0.00004 \text{ cm}^{-1}$ , which we do not consider significant given the accuracy of our frequency calibration using  $\text{SO}_2$ . The fact that the spectrum can be fit without any distortion constants, combined with the very small changes in rotational constants upon vibrational excitation, shows that pyrene comes close to behaving like an ideal rigid asymmetric rotor.

By comparing the relative intensities of the observed spectral lines with simulations at various temperatures, we were able to estimate the rotational temperature of the pyrene in our supersonic expansion to be  $\approx 23 \text{ K}$ . (for more details, see Supporting Information). This effective rotational cooling from

the source temperature of  $\approx 420 \text{ K}$  is consistent with the well-known efficiency of rotational-to-translational energy transfer in expansions.<sup>9</sup>

A driving motivation of the current work was to explore the efficiency of vibrational relaxation of such a large molecule in a supersonic expansion from a heated source. Vibrational cooling is critical because absorption from the ground vibrational state to an excited state is most relevant for enabling astronomical detections of molecules in the low temperature conditions of interstellar space. Adequate vibrational cooling is also experimentally important because of the strong temperature dependence of the vibrational partition function for large molecules. This occurs because large molecules have many vibrational modes and even at modest vibrational temperatures a significant portion of the molecular population can be partitioned into excited vibrational states. The concomitant depletion of population from the ground vibrational state reduces the absorption signal, potentially rendering observation of the spectrum technically infeasible even with sensitive absorption spectroscopy techniques. However, transfer of energy from vibrational degrees of freedom into rotation and translation is generally less efficient than rotation-translation transfer. For pyrene, with 72 vibrational normal modes, if there were no vibrational relaxation from the initial source temperature of  $420 \text{ K}$ , only 1 in 3000 pyrene molecules would be in the ground vibrational state. At a vibrational temperature of  $50 \text{ K}$ , in contrast, most of the pyrene molecules in the expansion are in the ground state.

To evaluate the vibrational cooling of pyrene, we used the quantitative absorption strength information from the cavity ringdown spectra. By calculating the total number density of pyrene in the cavity, and comparing the expected absorption intensity with that observed (see Supporting Information for details), we were able to infer the vibrational partition function ( $Q_{\text{vib}}$ ) to be  $1.41 \pm 0.17$ . This corresponds to a  $3\sigma$  upper bound on the vibrational temperature of  $111 \text{ K}$ ; we consider the rotational temperature of  $23 \text{ K}$  to be the lower bound of the vibrational temperature. This is consistent with vibrational temperature estimates from LIF studies of large organic molecules seeded in heated supersonic expansion sources.<sup>9,10,24</sup>

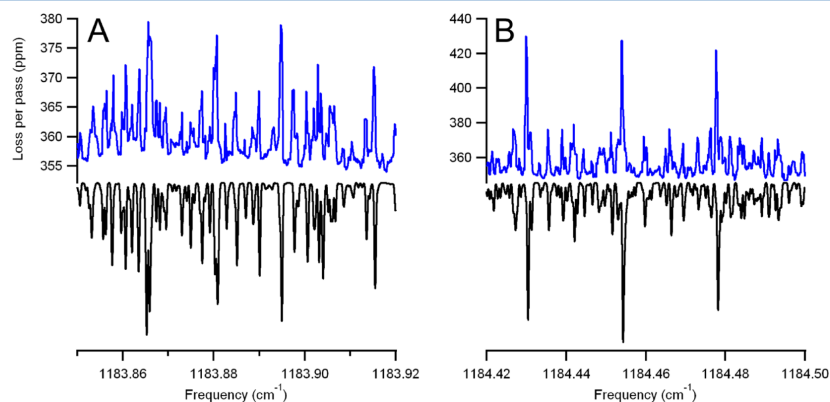


**Figure 3.** Expanded views of the observed (top traces, blue) and simulated (lower traces, black) spectrum near the band center (panel A), and in the R-branch (panel B).

In summary, pyrene is now the largest molecule to be studied with rotational resolution by absorption spectroscopy, and this work illustrates the feasibility of high-resolution large molecule spectroscopy using a simple heated oven supersonic expansion source. Analysis of the spectrum led to extraction of rotational constants for the ground and vibrationally excited states, revealing the extraordinarily rigid molecular structure of pyrene, in agreement with previous knowledge regarding the relative stiffness of PAHs. Larger PAHs, like coronene ( $C_{24}H_{16}$ ), are ideal targets to continue to test the limits of high-resolution absorption spectroscopy of large molecules, and to study the effectiveness of vibrational cooling in a slit nozzle supersonic expansion. Knowledge gained from these studies will offer insight into the feasibility of rotationally resolved infrared absorption spectroscopy of large potentially prebiotic molecules and fullerenes such as  $C_{60}$  and  $C_{70}$ . The resulting rotationally resolved spectra of PAHs and fullerenes will enable the first high-resolution astronomical searches for these large molecules in the interstellar medium.

## ■ ASSOCIATED CONTENT

### ● Supporting Information

Detailed comparison between experimental and simulated spectra, determination of rotational temperature, estimate of vibrational temperature, heated oven source details, frequency calibration, and a spectral line list are provided in the Supporting Information. This material is available free of charge via the Internet at <http://pubs.acs.org>.

## ■ AUTHOR INFORMATION

### Corresponding Author

\*E-mail: [bjmccall@illinois.edu](mailto:bjmccall@illinois.edu).

### Present Address

†Department of Electrical Engineering, Princeton University, Princeton, NJ 08544, United States.

### Author Contributions

The manuscript was written through contributions of all authors.

### Notes

The authors declare no competing financial interest.

## ■ ACKNOWLEDGMENTS

The authors wish to thank Matt Escarra and Professor Claire Gmachl from the Electrical Engineering Department at Princeton University for providing the quantum cascade laser used in this work. The development of our cavity ringdown spectrometer has been supported by the NASA Laboratory Astrophysics program and a David and Lucile Packard Fellowship. J.T.S. has been supported by a Robert C. and Carolyn J. Springborn Fellowship from the University of Illinois.

## ■ REFERENCES

- (1) Carruthers, G. R. Rocket Observation of Interstellar Molecular Hydrogen. *Astrophys. J. Lett.* **1970**, *161*, L81–L85.
- (2) Geballe, T. R.; Oka, T. Detection of  $H_3^+$  in Interstellar Space. *Nature* **1996**, *384*, 334–335.
- (3) Wilson, R. W.; Jefferts, K. B.; Penzias, A. A. Carbon Monoxide in the Orion Nebula. *Astrophys. J.* **1970**, *161*, L43–L44.
- (4) Lacy, J. H.; Evans, N. J., II; Achtermann, J. M.; Bruce, D. E.; Arens, J. F.; Carr, J. S. Discovery of Interstellar Acetylene. *Astrophys. J.* **1989**, *342*, L43–L46.

- (5) Lacy, J. H.; Carr, J. S.; Evans, N. J., II; Baas, F.; Achtermann, J. M.; Arens, J. F. Discovery of Interstellar Methane - Observations of Gaseous and Solid  $CH_4$  Absorption Toward Young Stars in Molecular Clouds. *Astrophys. J.* **1991**, *376*, 556–560.
- (6) Bernath, P. F.; Hinkle, K. H.; Keady, J. J. Detection of  $C_3$  in the Circumstellar Shell of IRC+10216. *Science* **1989**, *244*, 562–564.
- (7) Cernicharo, J.; Heras, A. M.; Tielens, A. G. G. M.; Pardo, J. R.; Herpin, F.; Gualin, M.; Waters, L. B. F. M. Infrared Space Observatory's Discovery of  $C_4H_2$ ,  $C_6H_2$ , and Benzene in CRL 618. *Astrophys. J. Lett.* **2001**, *546*, L123–L126.
- (8) Botta, O.; Bada, J. L. Extraterrestrial Organic Compounds in Meteorites. *Surv. Geophys.* **2002**, *23*, 411–467.
- (9) Amirav, A.; Even, U.; Jortner, J. Cooling of Large and Heavy Molecules in Seeded Supersonic Beams. *Chem. Phys.* **1980**, *51*, 31–42.
- (10) Amirav, A.; Even, U.; Jortner, J. Absorption Spectroscopy of Ultracold Large Molecules in Planar Supersonic Expansions. *Chem. Phys. Lett.* **1981**, *83*, 1–4.
- (11) Cable, J. R.; Tubergen, M. J.; Levy, D. H. Laser Desorption Molecular Beam Spectroscopy: The Electronic Spectra of Tryptophan Peptides in the Gas Phase. *J. Am. Chem. Soc.* **1987**, *109*, 6198–6199.
- (12) Elam, J. W.; Levy, D. H. Laser Ablation of Trp–Gly. *J. Phys. Chem. B* **1998**, *102*, 8113–8120.
- (13) Snoek, L. C.; van Mourik, T.; Simons, J. P. Neurotransmitters in the Gas Phase: A Computational and Spectroscopic Study of Noradrenaline. *Mol. Phys.* **2003**, *101*, 1239–1248.
- (14) van Dantzig, N. A.; Piotrowiak, P.; Levy, D. H. van der Waals Complexes of the Bichromophore Spirobifluorene. *Chem. Phys. Lett.* **1994**, *223*, 127–132.
- (15) Vala, M.; Szczepanski, J.; Pauzat, F.; Parisel, O.; Talbi, D.; Ellinger, Y. Electronic and Vibrational Spectra of Matrix-Isolated Pyrene Radical Cations: Theoretical and Experimental Aspects. *J. Phys. Chem.* **1994**, *98*, 9187–9196.
- (16) Joblin, C.; Boissel, P.; Leger, A.; D'Hendecourt, L.; Defourneau, D. Infrared Spectroscopy of Gas-Phase PAH Molecules. II. Role of the Temperature. *Astron. Astrophys.* **1995**, *299*, 835–846.
- (17) Allamandola, L. J.; Tielens, A. G. G. M.; Barker, J. R. Interstellar Polycyclic Aromatic Hydrocarbons: The Infrared Emission Bands, the Excitation/Emission Mechanism, and the Astrophysical Implications. *Astrophys. J. Suppl.* **1989**, *71*, 733–775.
- (18) Brumfield, B. E.; Stewart, J. T.; Widicus Weaver, S. L.; Escarra, M. D.; Howard, S. S.; Gmachl, C. F.; McCall, B. J. A Quantum Cascade Laser CW Cavity Ringdown Spectrometer Coupled to a Supersonic Expansion Source. *Rev. Sci. Instrum.* **2010**, *81*, 063102.
- (19) Brumfield, B. E.; Stewart, J. T.; McCall, B. J. High-Resolution Spectroscopy of the  $\nu_8$  Band of Methylene Bromide Using a Quantum Cascade Laser. *J. Mol. Spectrosc.* **2011**, *266*, 57–62.
- (20) Western, C. M. PGOPHER, a Program for Simulating Rotational Structure, <http://pgopher.chm.bris.ac.uk>, 2010.
- (21) Baba, M.; Saitoh, M.; Kowaka, Y.; Taguma, K.; Yoshida, K.; Semba, Y.; Kasahara, S.; Yamanaka, T.; Ohshima, Y.; Hsu, Y.-C.; Lin, S. H. Vibrational and Rotational Structure and Excited-State Dynamics of Pyrene. *J. Chem. Phys.* **2009**, *131*, 224318.
- (22) Hewett, K. B.; Shen, M.; Brummel, C. L.; Philips, L. A. High Resolution Infrared Spectroscopy of Pyrazine and Naphthalene in a Molecular Beam. *J. Chem. Phys.* **1994**, *100*, 4077–4086.
- (23) Piralì, O.; Boudon, V.; Oomens, J.; Vervloet, M. Rotationally Resolved Infrared Spectroscopy of Adamantane. *J. Chem. Phys.* **2012**, *136*, 024310.
- (24) Amirav, A.; Even, U.; Jortner, J. Energetics and Intramolecular Dynamics of the Isolated Ultracold Tetracene Molecule in Its First Excited Singlet State. *J. Chem. Phys.* **1981**, *75*, 3770–3793.

# Extending the Limits of Rotationally Resolved Absorption

## Spectroscopy: Pyrene

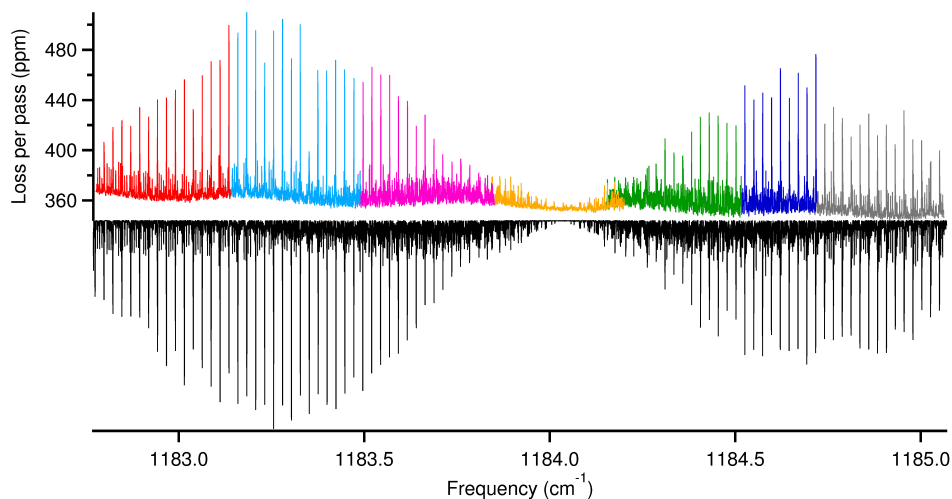
### Supporting Information

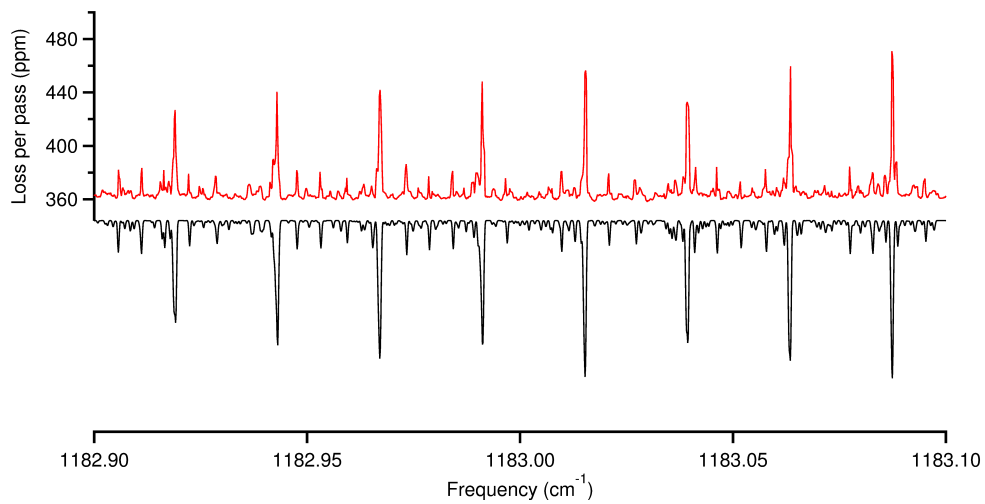
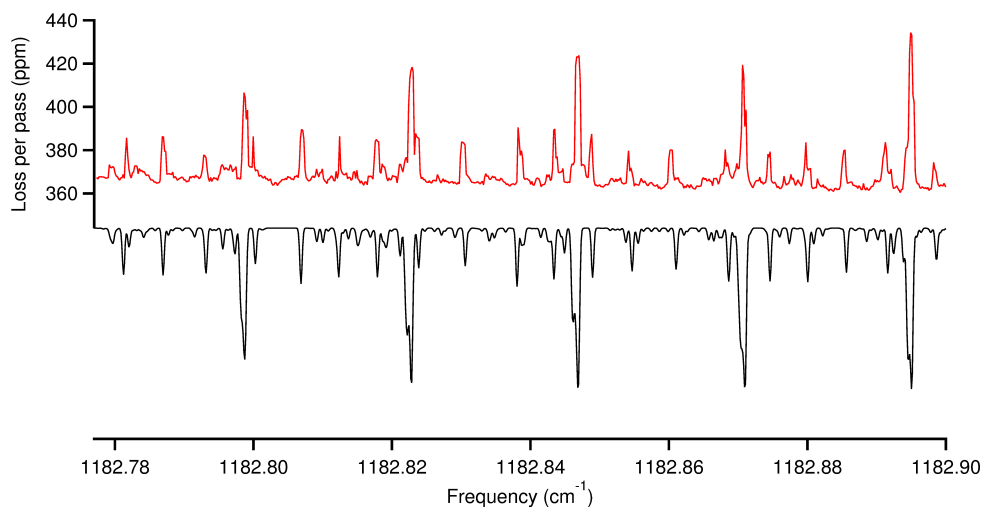
Brian Brumfield, Jacob Stewart, Benjamin McCall

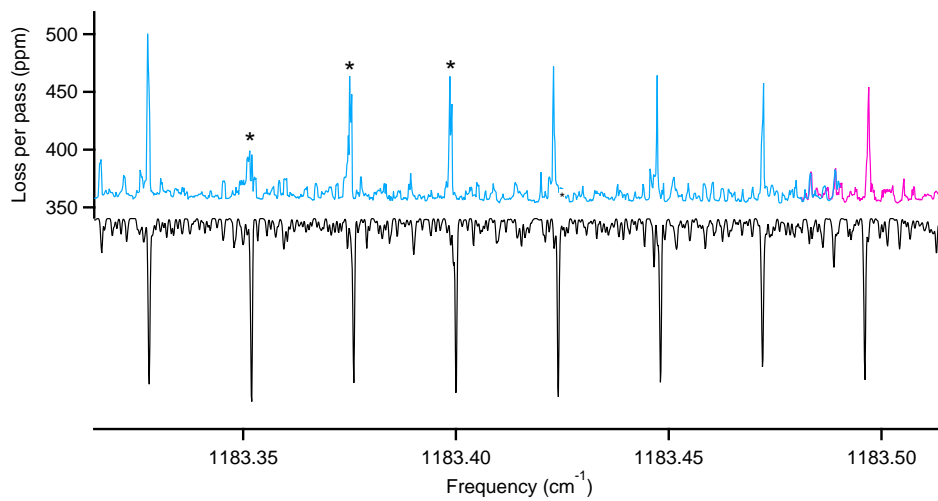
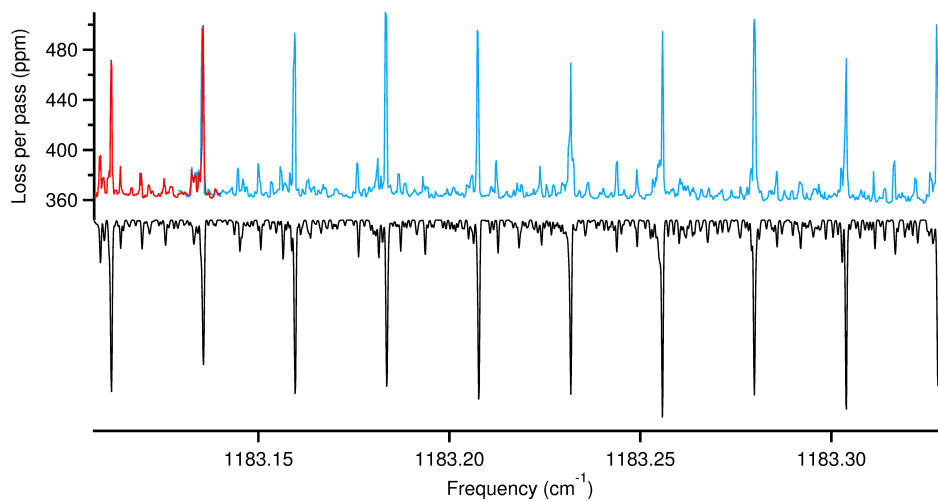
Department of Chemistry, University of Illinois, Urbana, Illinois 61801, United States

## 1 Comparison Between Experimental and Simulated Spectra

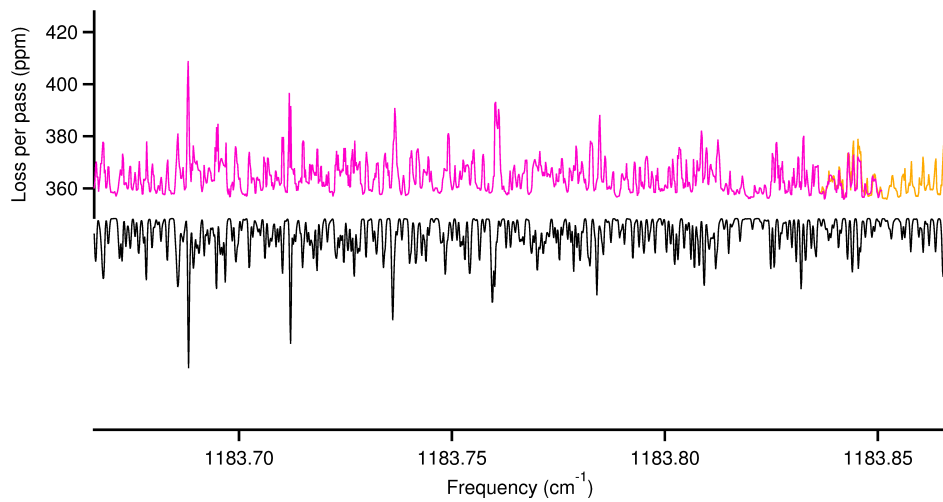
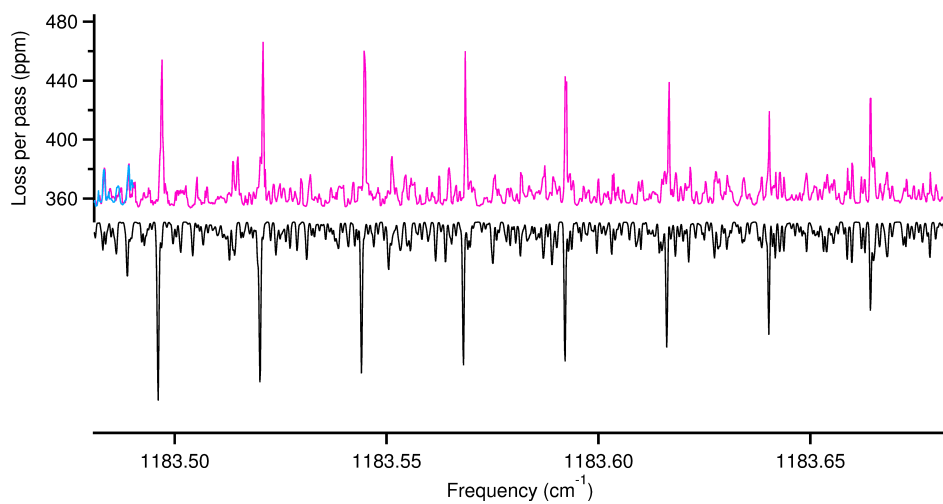
The following figures present the collected experimental spectra plotted against a simulated spectrum using molecular constants obtained from fitting to the asymmetric top Hamiltonian. The simulated spectrum was generated in Pgopher using a  $T_{rot}$  of 23 K and a Gaussian linewidth of 12 MHz ( $0.0004 \text{ cm}^{-1}$ ). The overall experimental coverage of the pyrene bending mode was achieved by overlapping multiple scans. In the figures below, each overlapping scan is indicated using a different color. Some of the figures are annotated to draw attention to specific details in the experimental spectra. Explanations for the figure annotations are provided beneath the figure.

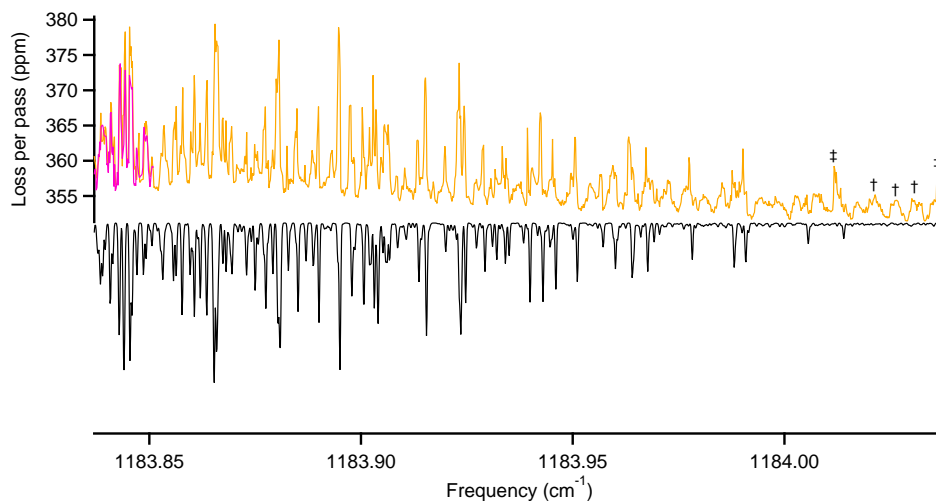






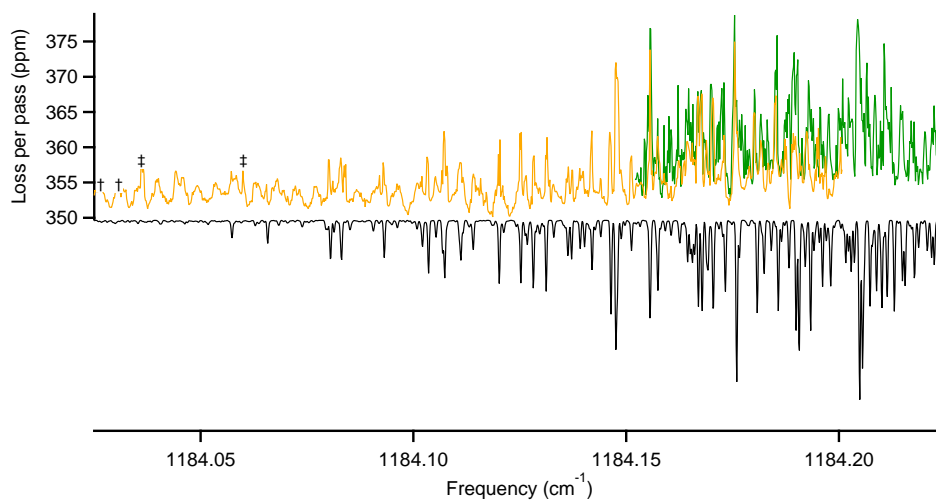
\*: Jagged lineshapes were observed for the features marked in this spectrum. This may have been an issue associated with laser frequency instability while scanning. Rescanning of this spectral region yielded spectral features without a jagged appearance.





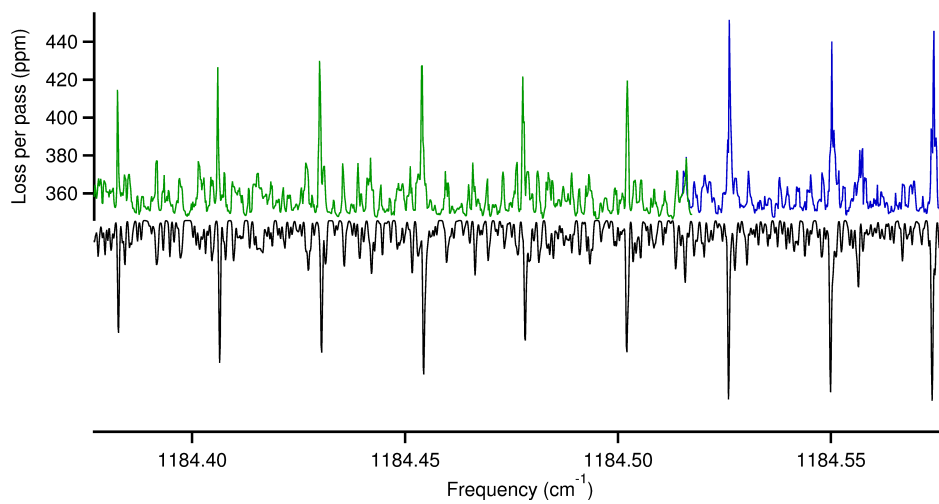
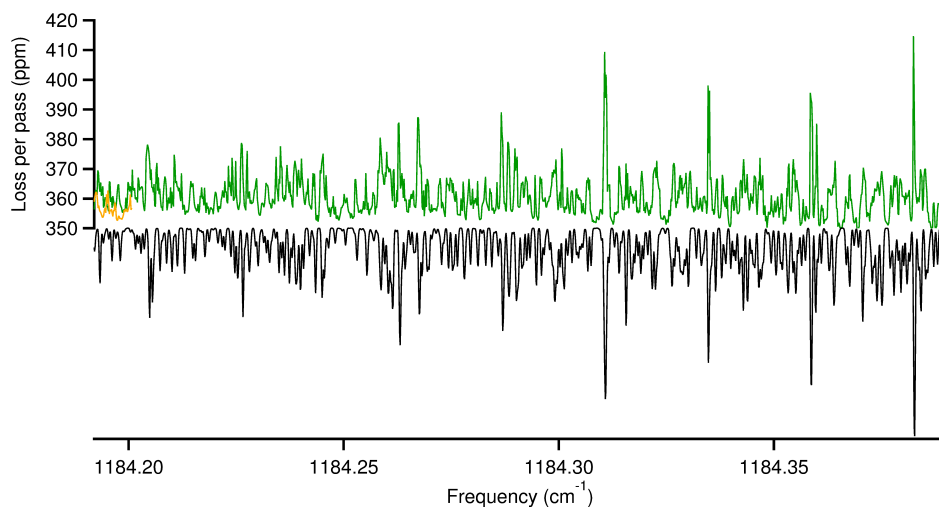
†: Near the band center, where spectral congestion is light, the presence of a periodic 2 ppm peak-to-peak feature can be seen. This has been seen in previous work, and is sensitive to the alignment of the ringdown mirrors.

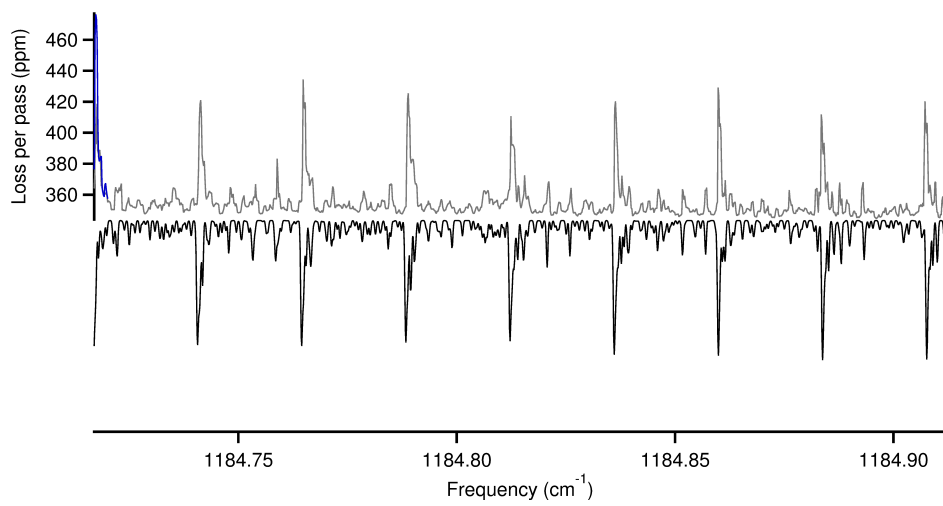
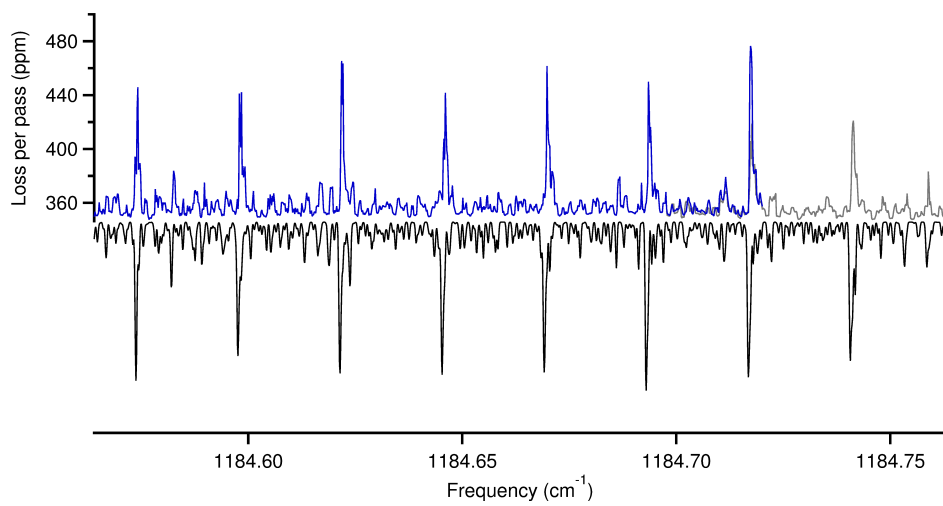
‡: Unidentified spectral features found near the band center that are significantly stronger than anything predicted for the C-H bending mode of  $^{12}\text{C}_{16}\text{H}_{10}$ .

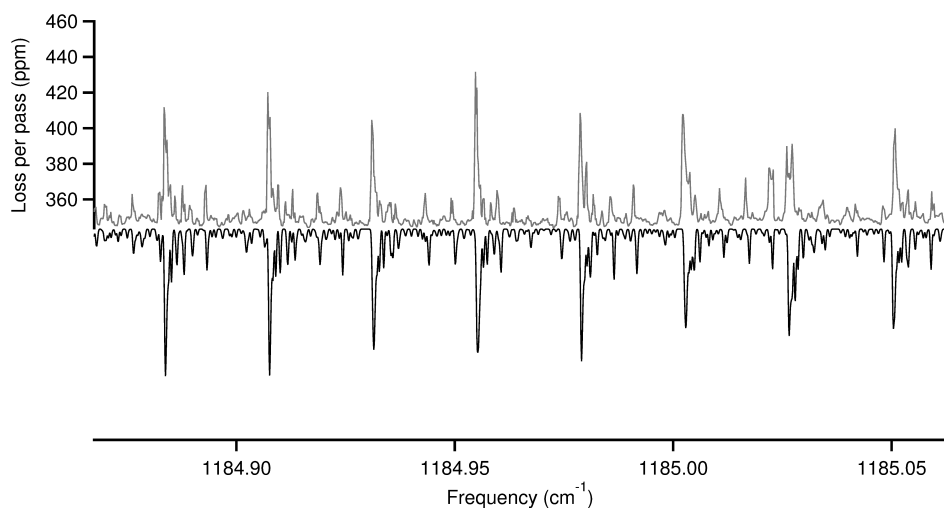


†: Near the band center, where spectral congestion is light, the presence of a periodic 2 ppm peak-to-peak feature can be seen. This has been seen in previous work, and is sensitive to the alignment of the ringdown mirrors.

‡: Unidentified spectral features found near the band center that are significantly stronger than anything predicted for the C-H bending mode of  $^{12}\text{C}_{16}\text{H}_{10}$ .







## 2 Determination of Rotational Temperature

A gross estimate of the rotational temperature of pyrene in the slit nozzle expansion was first made by observing the overall shape of the P and R branch rotational contours. In the following four figures the entire experimental spectrum is compared to a series of simulations at specific rotational temperatures for the entire vibrational band. In each figure the experimental spectrum is shown as trace A and the simulation as trace B.

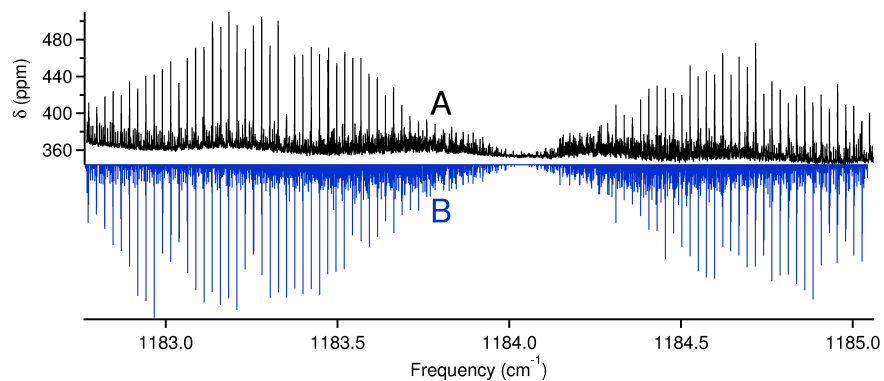


Figure 1: Experimental spectrum compared to simulation of vibrational band at a rotational temperature of 15 K.

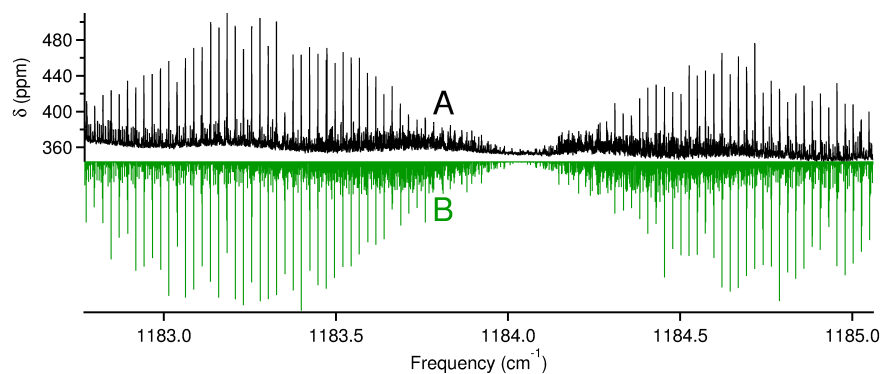


Figure 2: Experimental spectrum compared to simulation of vibrational band at a rotational temperature of 20 K.

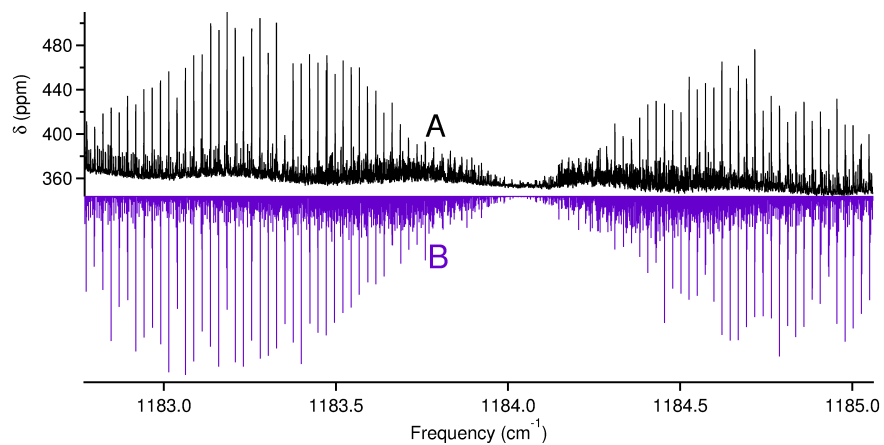


Figure 3: Experimental spectrum compared to simulation of vibrational band at a rotational temperature of 25 K.

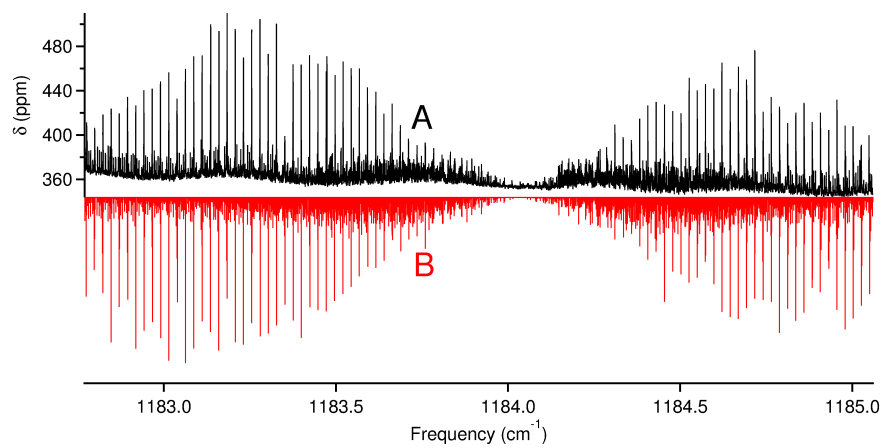


Figure 4: Experimental spectrum compared to simulation of vibrational band at a rotational temperature of 30 K.

Qualitative agreement between the experimental and simulated rotational band contours at 20 and 25 K is better than for simulations done at 15 and 30 K. This indicates that the experimental rotational temperature is between 20 and 25 K. To get a quantitative estimate of the rotational temperature an additional metric was applied comparing the peak intensities of 54 spectral features in the P and R branches of the experimental spectrum to a series of simulated spectra at rotational temperatures between 15 to 30 K done at 2.5 K intervals. First, the peak intensities of 54 spectral features in the experimental spectrum were normalized to the peak intensity for a single R-branch spectral feature. This same normalization process was then carried out for every spectral simulation run at different rotational temperatures, and the same R-branch spectral feature was used for normalization of the peak intensities in the simulated spectra. The differences between the normalized intensities for each spectral feature were then used in the following expression to generate a numerical value (Q) for the agreement between the experimental and simulation rotational temperature:

$$Q = \sum_{n=1}^{54} (I_{exptl, norm, n} - I_{sim, norm, n})^2 \quad (1)$$

The lower the value of Q from the peak intensity comparison the closer the simulation temperature is the actual rotational temperature observed in the experimental spectrum. Figure 5 shows a plot of this Q metric versus the simulated rotational temperature. From this plot the value for Q was lowest for the simulation with a rotational temperature of 22.5 K.

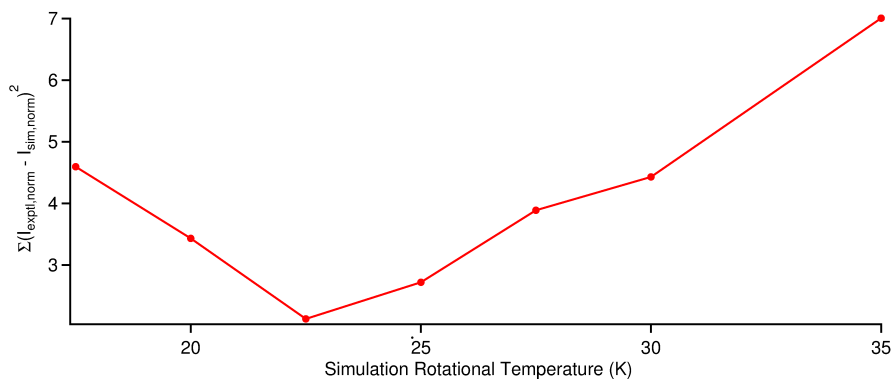


Figure 5: Plot of the quality of the rotational temperature comparison metric against the simulated rotational temperatures for 54 spectral features.

### 3 Estimate of Vibrational Temperature

In this section of the supplementary material the procedure used to estimate the vibrational temperature ( $T_{vib}$ ) in the expansion will be presented. In Figure 6 an overall view of the geometry of the overlap between the  $TEM_{00}$  mode of the cavity and the supersonic jet emerging from the expansion is presented. The forward direction of the supersonic expansion is collinear with the  $z$  direction, while the axis of the laser beam is defined collinear with the  $x$ -axis. The  $y$ -axis in Figure 6 is perpendicular to both the supersonic jet and the laser beam. The first goal of this section is to calculate the number density of

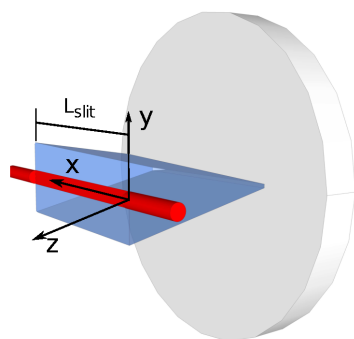


Figure 6: Illustration of the overlap of the  $TEM_{00}$  cavity mode with the supersonic expansion emerging from the slit nozzle.

pyrene probed in the supersonic expansion. In the process of carrying out this calculation the following assumptions will be made:

- 1.) The concentration variation along the axis of the laser beam ( $x$ -axis) can be neglected due to the small expansion divergence along this direction.
- 2.) The concentration variation along the supersonic expansion direction ( $z$ -axis) can be neglected because the beam waist of the  $TEM_{00}$  cavity is small compared to the distance between the slit and the laser beam.
- 3.) The concentration variation of pyrene in the direction perpendicular to both the expansion and the laser beam ( $y$ -axis) can also be neglected.

Because of the relatively small cross-section of the cavity mode with respect to the profile of the supersonic expansion along the  $y$ -axis, only a fraction of the total pyrene molecules are actually probed. Because of this the profile of the supersonic expansion along the  $y$ -axis will be evaluated by observing the change in the intensities of three pyrene spectral features.

Estimating the  $T_{vib}$  of pyrene in the supersonic expansion begins first with analysis of the mass loss from the oven expansion source. Spectra in this work were acquired using 25 grams of pyrene that ran

out in  $\sim 20$  hours at an oven temperature of  $155 - 160$  °C. Using the following formula

$$\dot{N}_{pyrene} = \frac{m_{pyrene} * N_A}{202.25 \frac{g}{mol}} \times T \times 0.837 \quad (2)$$

the number of pyrene molecules lost from the source per unit time ( $\dot{N}_{pyrene}$ ) is determined by multiplying the pyrene mass ( $m_{pyrene}$ ) by Avogadro's number ( $N_A$ ), and dividing that quantity by the gram formula mass for pyrene ( $202.25$  g/mol) multiplied by the time duration ( $T$ ) of the sample loss in seconds. This entire quantity is then multiplied by  $0.837$  because the natural abundance of  $^{13}\text{C}$  leads to a sample that is only  $83.7\%$  composed of all  $^{12}\text{C}$  pyrene. Inserting the appropriate values into equation (2),  $\dot{N}_{pyrene}$  was found to be  $8.6 \times 10^{17}$  molecules/s.

The expansion overlaps with the  $\text{TEM}_{00}$  mode of the ringdown cavity  $6$  mm downstream of the nozzle. Knowledge of the overlap between the  $\text{TEM}_{00}$  cavity mode with the supersonic expansion is critical for being able to calculate the maximum theoretical absorption depth of pyrene transitions. Knowledge of the cross-sectional area of the  $\text{TEM}_{00}$  cavity mode can be determined by calculating the cavity beam waist ( $\omega_0$ ) as follows:

$$\omega_0 = \sqrt{\frac{R\lambda}{\pi}} \times \sqrt{\frac{1+g}{4(1-g)}} \quad (3)$$

The size of  $\omega_0$  depends on the radius of curvature ( $R$ ) of the ringdown mirrors and the wavelength ( $\lambda$ ) of light being coupled into the cavity. The  $g$ -parameter is given by [1]:

$$g = 1 - \frac{L}{R} \quad (4)$$

where ( $L$ ) is the separation of the ringdown mirrors. Using equation (3), the calculated beam waist at  $8.5$   $\mu\text{m}$  for the current ringdown cavity configuration is  $1.1$  mm. The  $1.27$  cm length of the slit nozzle can be used for the interaction length because the divergence of the supersonic flow along this dimension is minimal. The total cross-sectional area perpendicular to the gas flow presented by the laser beam is then:

$$\sigma_{\text{TEM}_{00}} = 2\omega_0 \times L_{\text{slit}} \quad (5)$$

where  $\omega_0$  is the beam waist determined using equation (3), and  $L_{\text{slit}}$  is the length of the slit.

The fraction of  $\dot{N}_{pyrene}$  that overlaps with this cross-section is dependent on the vertical column density profile of the slit expansion. This information was found by studying the change in the peak heights for a series of strong pyrene spectral features as the source vertical position was adjusted. It was assumed that the changes in the column density of the transitions probed is only due to the fall-off in the center line number density of the expansion, and not due to possible spatial gradients in rotational temperature ( $T_{rot}$ ) or vibrational temperature  $T_{vib}$ . Figure 7 shows the three pyrene spectral features that were selected for monitoring the changes in peak height as a function of vertical source displacement.

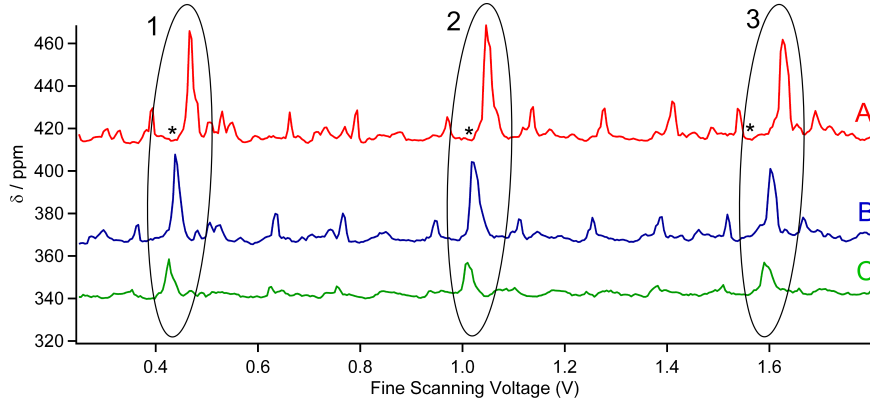


Figure 7: Plot of three scans over the same frequency region of the pyrene vibrational band with fractional loss in ppm plotted against the fine scanning DC voltage. The oven temperature during collection of these spectra drifted between 160.0 - 161.2 °C. Traces A, B, and C correspond to source height positions of 7 mm, 10.7 mm, and 12.7 mm respectively. The three spectral features whose peak heights were monitored as the source height was adjusted are enclosed in ellipses. These spectral features are labeled 1, 2, and 3 respectively. The peaks do not line up horizontally because of slow frequency drift in the laser over time. Trace A and Trace B have y-offsets of 70 and 30 ppm respectively. The asterisks mark the positions used for the baseline value of the adjacent spectral feature.

The peak height for the three features was determined by subtracting the fractional loss per pass for the tallest feature by the baseline value marked with an asterisk in Figure 7. The changes in the peak height for feature 3 as a function of vertical displacement are shown in Figure 8. The resulting peak intensity data for all three features was fit using a Gaussian profile as shown in Figure 8. The average value for the FWHM of the vertical column density profile for all three features was found to be  $8.3 \pm 0.8$  mm. Assuming that the expansion and cavity mode are centered, then the resulting overlap from integrating over the Gaussian column density profile is  $\sim 0.20$ . Dividing the fraction of  $\dot{N}_{pyrene}$  by the cross-sectional area of the cavity mode provided a value for the sample flux, but of primary interest was the probed number density ( $n_{pyrene}$ ).  $n_{pyrene}$  can be calculated by dividing the flux by the flow velocity  $v_{max}$  of the pyrene molecules. Because pyrene is the minority component of the expansion, its flow velocity in the expansion is dominated by the Ar carrier gas. The  $v_{max}$  for Ar can be calculated by [2, see eqn 6 in reference]:

$$v_{max} = \sqrt{\frac{5}{2}} \times \sqrt{\frac{2kT_0}{m}} \quad (6)$$

where  $v_{max}$  is determined by the pre-expansion temperature ( $T_0$ ) of the gas in the oven source times Boltzmann's constant ( $k$ ), and divided by the Ar mass ( $m$ ). At a pre-expansion temperature of 160 °C,  $v_{max}$  is  $\sim 6.7 \times 10^4$  cm/s. The use of  $v_{max}$  40 nozzle diameters downstream is a reasonable assumption [3], as this is close to the asymptotic limit of the Mach velocity in an ideal slit expansion. With  $v_{max}$ , the

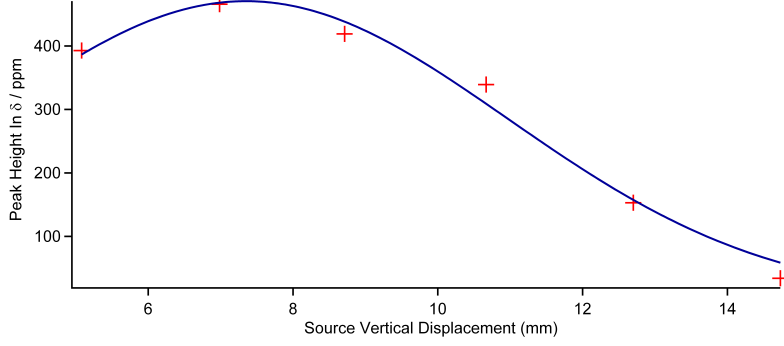


Figure 8: Plot of the peak height for feature 3 versus vertical source displacement. The red crosses are the experimental peak heights, and the blue curve is a Gaussian fit to the peak height data.

following expression was used to calculate  $n_{pyrene}$ :

$$n_{pyrene} = \frac{0.20 \times \dot{N}_{pyrene}}{\sigma_{TEM_{00}} v_{max}} \quad (7)$$

Using equation (7), the  $n_{pyrene}$  probed in the slit expansion at an oven temperature between 155 – 160 °C is estimated to be  $9.2 \times 10^{12} \text{ cm}^{-3}$ .

The next step in the process of estimating the vibrational cooling in the expansion involves comparing experimental absorption depths for selected P-branch transitions to calculated values of the absorption depth of the lines neglecting the contribution of clustering and the vibrational partition function. Because of the spectral density of transitions in the experimental pyrene spectra, the measured lines used to evaluate the experimental absorption depth were selected on the basis of their relative isolation from other spectral features. The five spectral lines selected are shown in Figure 9. These five lines are significantly weaker than the strongest features in the spectrum. The strongest features were neglected because they involve the partial overlap of multiple transitions. The experimental spectrum shows that these strong features are broader than the weaker lines, and show structure that is not always reproduced well by the simulation. In comparison, the weaker lines are the narrowest transitions seen in the spectrum, and involve an overlap of only two transitions that occur at nearly the same frequency. The weak lines selected still have an estimated S/N > 30. The experimentally measured absorption depth ( $A_E$ ) can be thought of as the reduction of maximum possible absorption depth ( $A_C$ ) due to clustering and the vibrational partition function:

$$A_E = \frac{A_C}{Q_{vib} \times C_{cluster}} \quad (8)$$

where  $Q_{vib}$  represents the contribution of the partition function, and  $C_{cluster}$  is a factor greater than or equal to 1 that accounts for the reduction in the calculated absorption depth due to the removal of pyrene

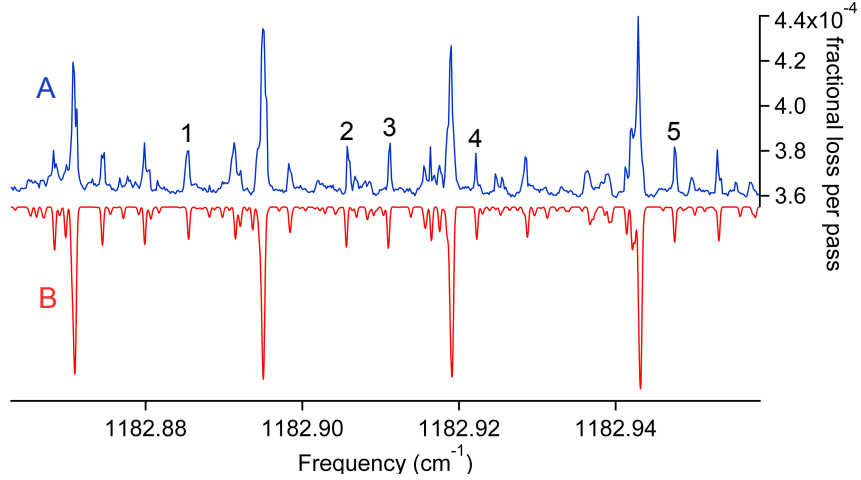


Figure 9: Trace (A) is an experimental section of the P-branch for the pyrene vibrational band acquired with an oven temperature between 155 - 160 °C 6 mm downstream of the expansion nozzle. Trace (B) is a simulation of the frequency region shown in Trace (A), with a  $T_{rot} = 25$  K. The numbers shown in Trace (A) denote the spectral features used to calculate the experimental absorption depth.

monomer concentration in the expansion. A factor has not been added for reduction in the experimental absorption due to optical saturation effects. The maximum intracavity power under the experimental conditions was 20.8 mW and the influence of saturation is negligible for the transitions that have been selected for the vibrational partition function calculation.  $A_C$  for the two overlapping transitions can be evaluated by using the expression:

$$A_C = \frac{n_{pyrene} \times f \times S' \times L_{slit}}{\Delta\nu} \quad (9)$$

where  $n_{pyrene}$  is the pyrene number density probed, and the value provided is from that estimated earlier using equation (7). The length of the slit ( $L_{slit}$ ) is considered the length of the interaction region probed by the cavity mode, and  $f$  is the sum of the two overlapping normalized line intensities from the simulated spectrum divided by the total normalized line intensities for the entire simulated vibrational band. The product of  $f$  with the band strength ( $S'$ ) then provides an estimate of the experimental value for the line intensity of the perfectly overlapped transitions.  $S'$  for this particular vibrational band has been measured experimentally [4] to be  $\sim 10$  km/mol ( $1.66 \times 10^{-18}$  cm/molecule), and is in good agreement with a theoretical estimate [5]. The total product is then divided by  $\Delta\nu$ , the linewidth, which is constrained to 12 MHz ( $0.0004$   $\text{cm}^{-1}$ ) for all five of the spectral features. Division of the  $A_C$  by the expression for  $A_E$  shown in equation (8) leads to:

$$\frac{A_C}{A_E} = \frac{A_C}{A_C \times Q_{vib} \times C_{cluster}} = Q_{vib} \times C_{cluster} \quad (10)$$

Table 1: Summarized data comparing the  $A_E$  to the  $A_C$  for all five spectral features shown in Figure 9. The first column provides the number label attached to the pair of transitions. The second column provides the final and initial quantum numbers describing the rotational quantum numbers for the rovibrational transition, and the third and fourth columns provide the  $A_E$  and  $A_C$  values respectively. The last column provides the ratio of  $A_C$  divided by  $A_E$ . The final two rows of the table present the average and standard deviation of the  $A_C/A_E$  ratios.

Spectral Feature	$J'_{K'_a, K'_c} - J''_{K''_a, K''_c}$	$A_E$ ( $\times 10^{-5}$ )	$A_C$ ( $\times 10^{-5}$ )	$A_C/A_E$
1	21 <sub>13,8</sub> -22 <sub>14,9</sub> : 21 <sub>13,9</sub> -22 <sub>14,8</sub>	1.95	2.38	1.22
2	16 <sub>16,0</sub> -17 <sub>17,1</sub> : 16 <sub>16,1</sub> -17 <sub>17,0</sub>	2.01	3.35	1.66
3	17 <sub>15,2</sub> -18 <sub>16,3</sub> : 17 <sub>15,3</sub> -18 <sub>16,2</sub>	2.27	3.28	1.44
4	19 <sub>13,6</sub> -20 <sub>14,7</sub> : 19 <sub>13,7</sub> -20 <sub>14,6</sub>	1.52	1.94	1.27
5	17 <sub>14,4</sub> -18 <sub>15,3</sub> : 17 <sub>14,3</sub> -18 <sub>15,4</sub>	2.07	2.96	1.42
			Average	1.41
			Standard Deviation	0.17

revealing that the ratio of the two quantities provides an estimate of the vibrational partition function and the degree of clustering in the expansion. The calculated ratios resulting from analysis of the experimental data and calculations are shown in Table 1. The average value obtained for  $Q_{vib} \times C_{cluster}$  was  $1.41 \pm 0.17$ . To calculate an upper limit on the  $T_{vib}$ , we assumed that  $C_{cluster}$  was equal to 1, its smallest possible value.

Translating the value of the partition function into an effective value for  $T_{vib}$  requires knowledge of the temperature dependence of the vibrational partition function. The vibrational partition expression for a polyatomic molecule is:

$$Q_{vib}(T_{vib}) = \prod_i^n (1 - e^{-\frac{\tilde{\nu}_i}{kT}})^{-1} \quad (11)$$

where  $n$  represents the total number of normal modes for the polyatomic molecule in question, and  $\tilde{\nu}_i$  is the vibrational frequency for the  $i^{th}$  normal mode in  $\text{cm}^{-1}$ .  $T_{vib}$  is given in units of Kelvin, and  $k$  represents Boltzmann's constant in units of  $\text{cm}^{-1}/\text{K}$ . Scaled harmonic frequencies from theoretical calculations [5, 6, 7] found in the NASA AMES PAH IR Spectral Database ([astrochem.org/pahdb](http://astrochem.org/pahdb)) are used for the values of  $\tilde{\nu}_i$ , and the resulting temperature dependence of  $Q_{vib}$  is shown in Figure 10.

The results of this analysis yield useful information about the value of  $T_{vib}$ . A  $Q_{vib}$  of 1.41 corresponds to a  $T_{vib}$  of 84 K. The  $3\sigma$  upper estimate for  $T_{vib}$  is 111 K, and the value of  $T_{rot}$  derived from the spectral fitting (23 K) can be adopted as the lower bound for  $T_{vib}$  because the rotational cooling in a supersonic expansion is more efficient than the vibrational cooling [8].

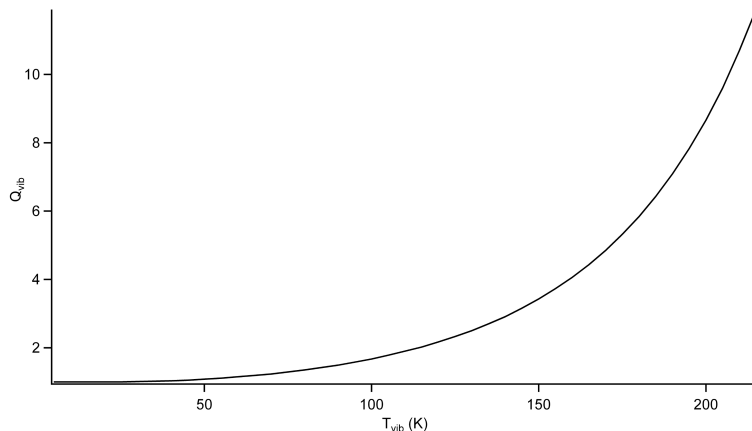


Figure 10: Plot of the pyrene vibrational partition function from a temperature of 0 to 220 K.

#### 4 Heated Oven Supersonic Expansion Source

To facilitate gas phase spectroscopy of large molecules we have built a high temperature oven capable of operating up to 700°C for at least 8 hours (see Figure 11). Our oven is made of stainless steel with six 300 W strip heaters (Chromalox NSA-1013) bolted onto the oven with high-temperature thermally conductive epoxy (Aremco 597-A) applied to the interface between the heaters and the oven. Power is supplied to the heaters using a pair of variable transformers (Staco Energy Products). To run at high temperatures (>350°C) we surround the oven with an aluminum heat shield to reflect blackbody radiation back onto the oven. The sample reservoir is capable of holding >50 g of sample and is built to hold liquid samples. This was important for pyrene because we needed to melt the pyrene to produce enough vapor pressure to detect absorption. The temperature of the oven was monitored by a thermocouple attached to the exterior of the oven.

#### 5 Frequency Calibration of Spectra

To calibrate the frequency of our high-resolution spectra, we used a mid-IR wavemeter (Bristol) for relative calibration and a reference cell filled with SO<sub>2</sub> for absolute calibration. We first fit the wavemeter data for each scan to a fourth order polynomial and used this fit to generate a relative frequency scale for each scan. Next, we adjusted the offsets of individual scans to ensure that features in the pyrene and SO<sub>2</sub> spectra which appeared in both scans overlapped, creating a relative frequency scale for the entire set of scans. As we stated in our previous work, there is a small frequency offset between our wavemeter reading and the true frequency. To determine this offset, we compared line center frequencies of our SO<sub>2</sub> reference scans on the relative frequency scale to reported values in HITRAN. Figure 1 shows a

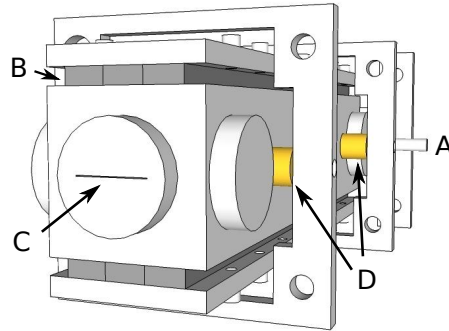


Figure 11: 3D schematic of our high temperature oven. A: Gas inlet line for argon carrier gas used in the supersonic expansion. B: Strip heaters for heating the oven. C: Slit where the supersonic expansion is created. D: Ceramic spacers which act as a thermal break between the oven and the plates and rods that suspend the oven in the vacuum chamber.

plot of the difference between the HITRAN frequencies and the relative frequencies obtained using the wavemeter data. The data clearly show a linear dependence of this difference as a function of frequency, meaning there is a systematic variation in the offset of the wavemeter reading from the true frequency as a function of frequency. To derive the proper offset to apply to the relative frequency scale to bring it to the true frequency, we fit the differences to a line (shown in the figure) which has a standard deviation in  $y$  of 15 MHz. We used the fit to add an offset to the relative frequency scale to create an absolute frequency scale. We used this scale for all of the data analysis presented in this communication after subtracting 40 MHz to account for the frequency shift caused by our acousto-optic modulator (AOM).

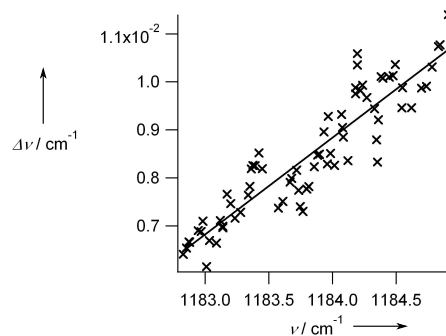


Figure 12: Plot of the difference between  $\text{SO}_2$  frequencies reported in HITRAN and the values we obtain using our wavemeter data versus the reported HITRAN frequencies. These data were fit to a line, which was used to calculate the proper offset to apply to our wavemeter data to bring it to the true frequency.

## References

- [1] K. Busch, M. Busch (Eds.), *Cavity-Ringdown Spectroscopy: An Ultratrace Absorption Measurement Technique*, American Chemical Society, Washington, DC, **1999**.
- [2] O. F. Hagena, *Surf. Sci.* **1981**, *106*, 101–116.
- [3] M. Sulkes, C. Jouviet, S. A. Rice, *Chem. Phys. Lett.* **1982**, *87*, 515–519.
- [4] C. Joblin, P. Boissel, A. Leger, L. D’Hendecourt, D. Defourneau, *Astron. Astrophys.* **1995**, *299*, 835.
- [5] S. R. Langhoff, *J. Phys. Chem.* **1996**, *100*, 2819–2841.
- [6] C. Bauschlicher, C. Boersma, A. Ricca, A. Mattioda, J. Cami, E. Peeters, F. Sánchez de Armas, G. Puerta Saborido, D. Hudgins, L. Allamandola, *Astrophys. J. Suppl.* **2010**, *189*, 341–351.
- [7] A. Mattioda, D. Hudgins, C. Boersma, A. Ricca, E. Peeters, J. Cami, F. Sanches de Armas, Puerta, C. Bauschlicher, A. L.J., The NASA Ames PAH IR Spectroscopic Database: The Laboratory Spectra, *in preparation*.
- [8] A. Amirav, U. Even, J. Jortner, *Chemical Physics* **1980**, *51*, 31–42.

# References

- [1] B. E. Brumfield, *Development of a quantum cascade laser based spectrometer for high-resolution spectroscopy of gas phase C<sub>60</sub>*, PhD thesis, University of Illinois at Urbana-Champaign, 2011.
- [2] F. N. Keutsch and R. J. Saykally, Proc. Natl. Acad. Sci. U. S. A. **98**, 10533 (2001).
- [3] S. Li, R. Zheng, Y. Zhu, and C. Duan, J. Mol. Spectrosc. **272**, 27 (2012).
- [4] J. B. Paul et al., J. Phys. Chem. A **103**, 2972 (1999).
- [5] H. W. Kroto, J. R. Heath, S. C. O'Brien, R. F. Curl, and R. E. Smalley, Nature **318**, 162 (1985).
- [6] J. Cami, J. Bernard-Salas, E. Peeters, and S. E. Malek, Science **329**, 1180 (2010).
- [7] K. Sellgren et al., Astrophys. J. Lett. **722**, L54 (2010).
- [8] D. A. García-Hernández et al., Astrophys. J. Lett. **724**, L39 (2010).
- [9] D. A. García-Hernández, N. K. Rao, and D. L. Lambert, Astrophys. J. **729**, 126 (2011).
- [10] D. A. García-Hernández et al., Astrophys. J. Lett. **737**, L30 (2011).
- [11] O. Berne and A. G. G. M. Tielens, Proc. Natl. Acad. Sci. U. S. A. **109**, 401 (2012).
- [12] J. Bernard-Salas et al., Astrophys. J. **757**, 41 (2012).
- [13] R. Saito, G. Dresselhaus, and M. S. Dresselhaus, Phys. Rev. B **50**, 5680 (1994).
- [14] N. Sogoshi et al., J. Phys. Chem. A **104**, 3733 (2000).
- [15] V. Piacente, G. Gigli, P. Scardala, A. Giustini, and D. Ferro, J. Phys. Chem. **99**, 14052 (1995).
- [16] B. E. Brumfield et al., Rev. Sci. Instrum. **81**, 063102 (2010).
- [17] B. E. Brumfield, J. T. Stewart, and B. J. McCall, J. Mol. Spectrosc. **266**, 57 (2011).
- [18] B. E. Brumfield, J. T. Stewart, and B. J. McCall, J. Phys. Chem. Lett. **3**, 1985 (2012).
- [19] A. Amirav, U. Even, and J. Jortner, Chem. Phys. **51**, 31 (1980).
- [20] A. Amirav, U. Even, and J. Jortner, Chem. Phys. Lett. **83**, 1 (1981).
- [21] J. Menendez and J. B. Page, *Light Scattering in Solids VIII: Fullerenes, Semiconductor Surfaces, Coherent Phonons*, Springer, Berlin / Heidelberg, 2000.
- [22] C. Frum et al., Chem. Phys. Lett. **176**, 504 (1991).
- [23] L. Nemes et al., Chem. Phys. Lett. **218**, 295 (1994).
- [24] B. Chase, N. Herron, and E. Holler, J. Phys. Chem. **96**, 4262 (1992).
- [25] R. E. Haufler et al., J. Phys. Chem. **94**, 8634 (1990).

- [26] D. A. Dixon, B. E. Chase, G. Fitzgerald, and N. Matsuzawa, *J. Phys. Chem.* **99**, 4486 (1995).
- [27] K. Busch and M. Busch, editors, *Cavity-Ringdown Spectroscopy: An Ultratrace Absorption Measurement Technique*, American Chemical Society, Washington, D.C., 1999.
- [28] O. F. Hagen, *Surf. Sci.* **106**, 101 (1981).
- [29] D. E. Weeks and W. G. Harter, *Chem. Phys. Lett.* **176**, 209 (1991).
- [30] C. Sundar et al., *Solid State Commun.* **84**, 823 (1992).
- [31] A. Popović, G. Dražič, and J. Marsel, *Rapid Commun. Mass Spectrom.* **8**, 985 (1994).
- [32] E. Schönherr, K. Matsumoto, and M. Freiberg, *Fullerene Sci. Techn.* **7**, 455 (1999).
- [33] M. E. Sanz, M. C. McCarthy, and P. Thaddeus, *J. Chem. Phys.* **122**, 194319 (2005).
- [34] C. Camy-Peyret, J. M. Flaud, A. Mahmoudi, G. Guelachvili, and J. W. C. Johns, *Int. J. Infrared Milli.* **6**, 199 (1985).
- [35] R. Toth, *J. Mol. Spectrosc.* **195**, 98 (1999).
- [36] D. R. Miller, *Atomic and Molecular Beam Methods*, volume 1, Oxford University Press, New York, 1988.
- [37] chemicalize.org was used for geometry prediction of pyrene, anthracene, tetracene, pentacene, ovalene, and D<sub>2</sub>O, April, 2013, chemicalize.org and ChemAxon (<http://www.chemaxon.com>).
- [38] C. W. Bauschlicher et al., *Astrophys. J. Suppl. S.* **189**, 341 (2010).
- [39] S. R. Langhoff, *J. Phys. Chem.* **100**, 2819 (1996).
- [40] T. Shimanouchi, *Tables of Molecular Vibrational Frequencies Consolidated Volume I*, National Bureau of Standards, Washington, D.C., 1972.
- [41] M. Sulkes, *Chem. Phys. Lett.* **119**, 426 (1985).
- [42] K. Jinno and C. Kohrikawa, *Chim. Oggi* **16**, 9 (1998).
- [43] S. Saim, K. C. Kuo, and D. L. Stalling, *Sep. Sci. Technol.* **28**, 1509 (1993).
- [44] C. H. Sin, M. R. Linford, and S. R. Goates, *Anal. Chem.* **64**, 233 (1992).
- [45] R. Hauffer et al., *Chem. Phys. Lett.* **179**, 449 (1991).
- [46] P. Voumard and R. Zenobi, *J. Chem. Phys.* **103**, 6795 (1995).
- [47] J. Y. Zhang, D. S. Nagra, and L. Li, *Anal. Chem.* **65**, 2812 (1993).
- [48] R. Z. Martínez, M. Metsälä, O. Vaittinen, T. Lantta, and L. Halonen, *J. Opt. Soc. Am. B* **23**, 727 (2006).
- [49] M. S. Taubman, T. L. Myers, B. D. Cannon, and R. M. Williams, *Spectrochim. Acta. A. Mol. Biomol. Spectrosc.* **60**, 3457 (2004).
- [50] G. Fraser, F. Lovas, R. Suenram, and K. Matsumura, *J. Mol. Spectrosc.* **144**, 97 (1990).
- [51] T. C. Germann and H. S. Gutowsky, *J. Chem. Phys.* **98**, 5235 (1993).
- [52] R. C. Cohen et al., *J. Chem. Phys.* **89**, 4494 (1988).
- [53] R. C. Cohen, K. L. Busarow, Y. T. Lee, and R. J. Saykally, *J. Chem. Phys.* **92**, 169 (1990).

- [54] R. C. Cohen and R. J. Saykally, *J. Chem. Phys.* **95**, 7891 (1991).
- [55] S. Suzuki, R. E. Bumgarner, P. A. Stockman, P. G. Green, and G. A. Blake, *J. Chem. Phys.* **94**, 824 (1991).
- [56] E. Zwart and W. L. Meerts, *Chem. Phys.* **151**, 407 (1991).
- [57] R. Lascola and D. J. Nesbitt, *The Journal of Chemical Physics* **95**, 7917 (1991).
- [58] D. J. Nesbitt and R. Lascola, *J. Chem. Phys.* **97**, 8096 (1992).
- [59] M. J. Weida and D. J. Nesbitt, *J. Chem. Phys.* **106**, 3078 (1997).
- [60] D. Verdes and H. Linnartz, *Chem. Phys. Lett.* **355**, 538 (2002).
- [61] R. C. Cohen and R. J. Saykally, *J. Chem. Phys.* **98**, 6007 (1993).
- [62] J. Makarewicz, *J. Chem. Phys.* **129**, 184310 (2008).
- [63] L. Rothman et al., *J. Quant. Spectrosc. Ra.* **110**, 533 (2009).
- [64] C. Western, PGOPHER, a program for simulating rotational structure, 2010.
- [65] J. M. Hollas, *Modern Spectroscopy*, John Wiley & Sons Ltd, Chichester, England, fourth edition, 2004.
- [66] N. Goldman, C. Leforestier, and R. J. Saykally, *Philos. T. Roy. Soc. A* **363**, 493 (2005).
- [67] R. Bukowski, K. Szalewicz, G. C. Groenenboom, and A. van der Avoird, *Science* **315**, 1249 (2007).
- [68] G. T. Fraser, *Int. Rev. Phys. Chem.* **10**, 189 (1991).
- [69] R. S. Fellers, C. Leforestier, L. B. Braly, M. G. Brown, and R. J. Saykally, *Science* **284**, 945 (1999).
- [70] T. R. Dyke, *J. Chem. Phys.* **60**, 2929 (1974).
- [71] T. R. Dyke, K. M. Mack, and J. S. Muentzer, *J. Chem. Phys.* **66**, 498 (1977).
- [72] J. A. Odutola and T. R. Dyke, *J. Chem. Phys.* **72**, 5062 (1980).
- [73] L. H. Coudert, F. J. Lovas, R. D. Suenram, and J. T. Hougen, *J. Chem. Phys.* **87**, 6290 (1987).
- [74] G. T. Fraser, R. D. Suenram, and L. H. Coudert, *J. Chem. Phys.* **90**, 6077 (1989).
- [75] R. Suenram, G. Fraser, and F. Lovas, *J. Mol. Spectrosc.* **138**, 440 (1989).
- [76] E. Karyakin, G. Fraser, and R. Suenram, *Mol. Phys.* **78**, 1179 (1993).
- [77] G. T. Fraser et al., *J. Mol. Spectrosc.* **181**, 229 (1997).
- [78] E. Zwart, J. J. ter Meulen, and W. L. Meerts, *Chem. Phys. Lett.* **173**, 115 (1990).
- [79] E. Zwart, J. ter Meulen, W. Leo Meerts, and L. Coudert, *J. Mol. Spectrosc.* **147**, 27 (1991).
- [80] K. L. Busarow et al., *J. Chem. Phys.* **90**, 3937 (1989).
- [81] N. Pugliano and R. J. Saykally, *J. Chem. Phys.* **96**, 1832 (1992).
- [82] L. B. Braly, J. D. Cruzan, K. Liu, R. S. Fellers, and R. J. Saykally, *J. Chem. Phys.* **112**, 10293 (2000).
- [83] L. B. Braly et al., *J. Chem. Phys.* **112**, 10314 (2000).
- [84] F. N. Keutsch et al., *J. Chem. Phys.* **119**, 8927 (2003).
- [85] Z. S. Huang and R. E. Miller, *J. Chem. Phys.* **91**, 6613 (1989).

- [86] J. B. Paul, R. A. Provencal, and R. J. Saykally, *J. Phys. Chem. A* **102**, 3279 (1998).
- [87] G. C. Groenenboom et al., *J. Chem. Phys.* **113**, 6702 (2000).
- [88] F. Keutsch, N. Goldman, H. Harker, C. Leforestier, and R. Saykally, *Mol. Phys.* **101**, 3477 (2003).
- [89] X. Huang et al., *J. Chem. Phys.* **128**, 034312 (2008).
- [90] Y. Wang, S. Carter, B. J. Braams, and J. M. Bowman, *J. Chem. Phys.* **128**, 071101 (2008).
- [91] A. Shank, Y. Wang, A. Kaledin, B. J. Braams, and J. M. Bowman, *J. Chem. Phys.* **130**, 144314 (2009).
- [92] C. Leforestier, R. van Harreveld, and A. van der Avoird, *J. Phys. Chem. A* **113**, 12285 (2009).
- [93] C. Leforestier, K. Szalewicz, and A. van der Avoird, *J. Chem. Phys.* **137**, 014305 (2012).
- [94] G. Ayers and A. Pullin, *Spectrochim. Acta A* **32**, 1629 (1976).
- [95] J. Perchard, *Chem. Phys.* **273**, 217 (2001).
- [96] A. Engdahl and B. Nelander, *J. Mol. Struct.* **193**, 101 (1989).
- [97] S. Coussan, P. Roubin, and J. Perchard, *Chem. Phys.* **324**, 527 (2006).
- [98] J. Ceponkus and B. Nelander, *J. Phys. Chem. A* **108**, 6499 (2004).
- [99] J. Ceponkus, P. Uvdal, and B. Nelander, *J. Phys. Chem. A* **112**, 3921 (2008).
- [100] J. T. Stewart and B. J. McCall, *J. Mol. Spectrosc.* **282**, 34 (2012).
- [101] T. R. Dyke, *J. Chem. Phys.* **66**, 492 (1977).
- [102] J. D. Cruzan et al., *Science* **271**, 59 (1996).
- [103] G. Herzberg, *Infrared and Raman Spectra of Polyatomic Molecules*, D. Van Nostrand, New York, 1945.
- [104] H. A. Harker et al., *Mol. Phys.* **105**, 497 (2007).
- [105] I. M. Mills, *J. Phys. Chem.* **88**, 532 (1984).
- [106] R. F. Curl et al., *Chem. Phys. Lett.* **487**, 1 (2010).
- [107] C. Gmachl et al., *Appl. Phys. Lett.* **79**, 572 (2001).
- [108] C. Gmachl, D. L. Sivco, R. Colombelli, F. Capasso, and A. Y. Cho, *Nature* **415**, 883 (2002).
- [109] J. Faist, M. Beck, T. Aellen, and E. Gini, *Appl. Phys. Lett.* **78**, 147 (2001).
- [110] K. Faist et al., *IEEE J. Quantum. Electron.* **38**, 533 (2002).
- [111] R. Maulini, M. Beck, J. Faist, and E. Gini, *Appl. Phys. Lett.* **84**, 1659 (2004).
- [112] G. P. Luo et al., *Appl. Phys. Lett.* **78**, 2834 (2001).
- [113] G. Luo et al., *IEEE J. Quantum. Electron.* **38**, 486 (2002).
- [114] G. Wysocki et al., *Appl. Phys. B: Lasers Opt.* **81**, 769 (2005).
- [115] R. Maulini, A. Mohan, M. Giovannini, J. Faist, and E. Gini, *Appl. Phys. Lett.* **88**, 201113 (2006).
- [116] G. Wysocki et al., *Appl. Phys. B: Lasers Opt.* **92**, 305 (2008).
- [117] T. C. Cheng et al., *J. Phys. Chem. Lett.* **3**, 3160 (2012).
- [118] O. Asvany et al., *Science* **309**, 1219 (2005).